4D Imaging of Paper: A Novel Method to Characterize Deformation Mechanisms

by

Farzin Golkhosh

A THESIS SUBMITTED IN PARTIAL FULFILLMENT OF
THE REQUIREMENTS FOR THE DEGREE OF

MASTER OF APPLIED SCIENCE

in

THE COLLEGE OF GRADUATE STUDIES

(Mechanical Engineering)

THE UNIVERSITY OF BRITISH COLUMBIA
(Okanagan)

December 2018

The following individuals certify that they have read, and recommend to the College of Graduate Studies for acceptance, a thesis/dissertation entitled:

4D Imaging of Paper: A Novel Method to Characterize Deformation Mechanisms

submitted by Farzin Golkhosh in partial fulfillment of the requirements of the degree of Master of Applied Science

Prof. Lukas Bichler, School of Engineering, UBC Okanagan
Supervisor

Prof. André Phillion, Materials Science and Engineering, McMaster University
Co-supervisor

Prof. Mark Martinez, Chemical and Biological Engineering, UBC Vancouver
Supervisory Committee Member

Prof. Douglas W. Coffin, Chemical, Paper, and Biomedical Engineering, Miami University
University Examiner

Abstract

Recent advancements in fast synchrotron x-ray tomography has made it possible to acquire time-resolved 3D image volumes (4D Imaging) of different materials including paper that can be utilized for direct observation of their microstructure under deformation. Considering the importance of inter-fibre bonding in prediction of paper behaviour, especially when paper is formed from a pulp mixture, this thesis devises a method to evaluate the level of inter-fibre bonding using 4D imaging experiments. To do so, four samples with different levels of bonding, and six samples with different fractions of NBSK and Eucalyptus fibres were scanned by synchrotron x-ray tomography while being deformed in a tensile tester in an interrupted fashion. Qualitative observations of the sample with the weakest level of bonding revealed some significant thickness expansions in and around the regions of failure. Measurements of fibre-fibre contacts and curl index showed that inter-fibre bond breakage, in addition to fibre straightening, are the underlying mechanisms for such thickness expansions. This lead to a conclusion that out-of-plane deformations of paper samples during tensile testing can be used as a criterion to measure the level of bonding inside their networks. Qualitative observations of the samples with different levels of bonding showed that there is a strong correlation between such thickness expansions and the levels of bonding further confirming that out-of-plane deformations can be used as a measure to evaluate network efficiency. To do so, norms of the out-of-plane strain fields obtained from DVC analysis were used to quantify such thickness expansions that also showed strong correlation with the levels of bonding. Application of such analysis on mixture samples revealed some unexpected results where 100% NBSK samples showed higher thickness expansions when compared to 100% Eucalyptus samples when 100% NBSK sample is expected to have higher levels of bonding. This trend was explained by an increase of the free fibre lengths due to addition of longer fibres to the pulp mixture.

This underlined the need for consideration of the contribution of free fibre lengths to such thickness expansions to evaluate the level of bonding inside samples made from mixture of fibres that have different lengths.

Lay Summary

Advancements in x-ray imaging has made it possible to observe the evolution of internal structure of different materials during deformation. In this thesis such imaging methods are used for direct observation of internal structure of paper during tensile deformation. This is then used to develop a method to evaluate the level of fibre-fibre bonding of different paper networks which is one of the most important factors that determine their mechanical behaviour. This becomes particularly important when paper is made from a mixture of fibres where the difference between the fibres can influence the level of fibre-fibre interaction making it challenging to predict their behaviour. The findings of this thesis shows that thickness expansions of paper during tensile deformation can be used as a measure to evaluate the level of fibre-fibre interaction in their networks. They also underline that for a conclusive evaluation of mixture samples other measurements of their fibre network are also necessary.

Preface

This work has been done under supervision of Prof. André Phillion and Prof. Mark Martinez. With the exception of my supervisory committee members, who provided detailed suggestions on the experiments and analysis of the obtained data, I am the primary contributor of this work.

All paper samples were provided by Canfor Pulp Innovation. 4D Imaging experiments were conducted at Diamond Light Source, UK with the help of the research group of Prof. Peter Lee, University of Manchester, who also provided the tensile testing equipment.

In Chapter 2, I designed the multi-sample test with the guidance of my supervisors that were additively manufactured at UBC Okanagan. I prepared the samples for the multi-sample test setup at UBC Okanagan. The freeze-dried samples were cut at University College London. I developed all the improvements on the existing fibre segmentation algorithms and also developed all the pre- and post-processing routines in this chapter.

In Chapter 4, I conducted all the analyses, performed the DVC calculations and developed the routines for quantification of the analyses. Parts of Chapter 4 and 3 were presented at "The Fundamental Pulp and Paper Research Symposium" in Oxford, UK in September 2017

In Chapter 5, I developed all the quantification routines and performed all of the calculations and analyses.

Table of Contents

List of Tables

List of Figures

Acknowledgements

I would like to express my sincere gratitude to Prof. André Phillion for his continuous support and mentorship during this project. Under his supervision I grew as a researcher and gained invaluable knowledge and experience.

I also would like to thank Prof. Mark Martinez for his insights and guidance. I also would like to thank Prof. Peter Lee for providing insights and support during 4D imaging experiments. I am also thankful to Prof. Lukas Bichler for his support.

I would also like to thank Loic Courtois, David Eastwood, Yash Sharma, and Wendy Tsai who helped me with the 4D imaging experiments at Diamond Light Source.

I wish to thank all my friends at both UBC Okanagan and Vancouver campuses. I wish to thank Sadegh Hasanpour, Majid Targhagh, Mohammad Mohseni, Moein Ahamadipour, Reza Larimi, Armin Rashidi, Ali Moallemi, and Hamed Helisaz who made this journey more enjoyable.

Finally, I would like to acknowledge the financial supports of Canfor Ltd., and NSERC for funding this research.

To my beloved wife, Mahsa
for her unconditional love
To my dear parents, Najibeh and Masoud
and my dear brother, Farzad
for their endless support

Chapter 1

Introduction

The advent of digital media has led to a decline in the application of paper as a medium, which has motivated the industry to embark on a journey to find novel applications for such a ubiquitous yet interesting material. This trend has resulted in the development of some novel paper-based technologies ranging from low-cost and flexible electronics [1] and energy devices [2] to biomedical sensors [3]. As a consequence, some previously overlooked properties of paper, including the mechanical properties, have been regaining attention in the research community. This underlines the need for further investigation of the process-structure-property relationship of paper materials.

The mechanical properties of paper depend not only on the properties of its constituent fibres, but also on the cumulative and relative arrangement of those fibres that form the fibre network. Consequently, the mechanical properties of paper can be divided into two length-scales: fibre-level and network-level. Modification of either or both of these properties can help in tailoring the mechanical properties of paper materials for specific applications. In general, two main processing steps are utilized for this purpose: refining and pulp mixture. Refining induces some changes to morphology of fibres that can also affect the network-level properties. Application of different fibres inside the pulp mixture also influences the properties by changing the intrinsic properties of the constituent fibres. In general, the main motive behind the application of pulp mixtures is to reduce the fraction of more expensive softwood fibres inside the pulp mixture by substitution of less expensive fibres while achieving the desired properties. However, the change of pulp mixture can also effect the network

properties by altering the fibre-fibre interactions (i.e. the level of inter-fibre bonding) inside the network making the process-structure-property relation more complex. Therefore, understanding the changes in fibre-fibre interactions made by changing the pulp blend is of paramount importance for prediction of their properties.

Since the failure of paper can be associated with disruption of either the fibres themselves or their bonding inside the network, characterization of failure mechanisms, or in other words the measurement of the evolution of relevant fibre-level and network-level properties during deformation, can significantly contribute to our understanding of the underlying physics of paper-based products. However, considering the complex morphology of paper fibres and its network, characterization of deformation mechanisms is not a trivial task, especially by direct measurement. Recent advancements in different imaging modalities including X-ray Computed Tomography (CT) has made it possible to obtain detailed high quality three-dimensional data of paper's microstructure. Such data can be used along with sophisticated image analysis algorithms to measure different properties of paper. Furthermore, fast imaging capabilities of the third generation synchrotron X-ray imaging facilities has also made it possible to perform some 4D (3D + time) imaging of different in-situ mechanical tests. The 4D data can be used in measurement of evolution of properties. In particular, it can be used to characterize the deformation mechanisms in paper.

Considering the importance of fibre-fibre interactions in predicting the behaviour of paper materials, especially when they are formed from a mixture of different fibres, the main focus of this thesis is to gain insight about the correlation of deformation and failure of paper and the level of fibre-fibre bonding of their network, and to apply those insights to evaluate the level of bonding in different mixture samples. This can be done by performing a 4D imaging of tensile testing of paper samples, and then analyzing the obtained data by different image analysis techniques to measure the evolution of some relevant microstructural descriptors during deformation. The experiments can then be repeated for a set of samples with different levels of bonding to quantify the effect of fibre-fibre bonding on deformation mechanisms. The insights gained from these experiments can then be used to evaluate the level of inter-fibre bonding inside different mixture samples.

1.1 Literature Review

This section provides a review of the relevant literature, specifically, around fundamentals of paper physics, factors affecting fibres and bonding, and image analysis methods that are relevant to paper. In section 1.1.1, the literature surrounding the structure-property relation of paper with a focus on its tensile strength is explored. This section tries to establish the importance of inter-fibre bonding as a determining factor of paper's mechanical behaviour and its relation to paper's deformation and failure. The process part of the process-structure-property relation of paper is explained in section 1.1.2 where factors that can affect fibres and their bonding are considered. This section provides a review of some of the relevant literature about refining, pulp mixture, and drying of paper. In section 1.1.3, a brief explanation of X-ray CT and its application in characterizing paper materials is also provided.

1.1.1 Paper Physics

There are two major factors that influence the strength properties of paper materials: the strength of constituent fibres and the strength of inter-fibre bonding [4]. Before moving to deformation and failure of paper, it is important to understand the relation between these factors and the overall tensile strength.

1.1.1.1 Tensile Strength of Paper

There have been many studies examining the link between the properties of individual fibres and properties of the final paper sheets, especially their tensile strength [5]. One of the first studies in this area was the work of Cox et al. [6] in which they calculated the strength of paper and other fibrous materials using the modulus of the paper fibres, along with a function of fibre orientation. Cox applied the above model to investigate the mechanical properties of a resin-filled planar fibre mat, and showed that for a homogeneous sheet, the elastic modulus was equal to one-third as compared to Young's modulus of an individual fibre. Although this model provided new insight into stress distribution in paper handsheets, the calculated results poorly matched the experimental findings. This was attributed to the curved morphology of actual papermaking fibres, and the transmission of the load through the inter-fibre bonds.

The research by Cox inspired the development of new models that better accounted for paper physics. Perhaps, the most well-known example of these models is the work of Page and Seth [7, 8], where the structure of paper sheet was included in the mathematical analysis of Cox to directly predict Young's modulus and tensile strength. The Page equation is given below,

$$E_p = \frac{1}{3}E_f\Big[1 - (\frac{w}{L\,RBA})\sqrt{\frac{E_f}{2\,G_f}}\tanh\Big(\frac{L\,RBA}{w}\sqrt{\frac{2\,G_f}{E_f}}\Big)\Big] \tag{1.1}$$

$$\frac{1}{T} = \frac{9}{8Z} + \frac{12A\rho g}{bPL(RBA)} \tag{1.2}$$

where in equation 1.1, E_p is the elastic modulus of paper, E_f is the axial elastic modulus of the component fibres, w is the mean fibre width, L is the arithmetic mean fibre length, G_f is the shear modulus of the component fibres for shear in (L, w) plane, and in equation 1.2, Z is the zero span tensile strength, T is the tensile strength, A is the average fibre cross section, b is the measured shear bond strength per unit bonded area, and P is the perimeter of the fibre cross section. The term RBA is used to represent the Relative Bonded Area. These equations have been extensively applied to different paper types where they have shown good agreement with experimental data. The presence of the terms RBA and b in these equations clearly shows the major role that inter-fibre bonding can play on the strength properties of paper, which will be explained in more details in the following sections.

1.1.1.2 Inter-fibre Bonding

As mentioned earlier, inter-fibre bonding is one of the major factors influencing the strength properties of paper. An inter-fibre bond can be described as the zone where two fibres are so close that different bonding mechanisms become activated [9]. In general, six different mechanisms are thought to contribute to the development of bonds between cellulose fibres [10, 11, 12]: mechanical interlocking, capillary forces, inter-diffusion, Coulomb forces, hydrogen bonding and Van der Waals' forces. In a recent study, Hirn and Scennach [10] have quantified the contribution of each mechanism to the inter-fibre bonding of cellulose fibres and reported that despite the general belief which flavours hydrogen bonding as the main contributor, Van der Waals' bonds play the most important role. Regardless, these inter-molecular bonding mechanisms only

become relevant when a molecular contact, i.e. contact less than 300 Å, is obtained. Molecular contacts between fibres are achieved by capillary forces pulling fibres together when water is removed. This mechanism of fibre bonding was first explained in detail by Campbell [13], and is known as the *Campbell Effect.* In the wet state during paper formation, capillary bridges are formed between fibres. As pulp fibres are hygroscopic and contain about 10% water at ambient conditions [10], capillary bridges do not disappear during drying but instead result in capillary forces that pull fibre surfaces together, leading to the creation of molecular contacts.

Although the knowledge of mechanisms involved in the formation of inter-fibre bonding are useful for understanding of the physical behaviour of paper, the details of their inheritance makeup is not necessary for studying the effect of bonding in deformation and failure mechanisms. In general, in the context of deformation and failure of paper, the effect of inter-fibre bonding is mainly considered through characterization of their strength and extent by measurement of the specific bond strength and RBA, respectively.

Bond Strength The strength of bonds in a paper is usually quantified by the specific bond strength, which is defined as the ratio of the shear strength of the bond to the area of that bond [9]. The most common way of studying bonding and bond strength in paper is by performing mechanical tests in the out-of-plane direction (z-directional tensile test, delamination test, and Scott bond test) [14]. According to Koubaa and Koran [15], the results obtained from these tests, strength, energy, and modulus, are highly correlated with each other but do not provide the real value of the fibre-to-fibre bond strength.

In the delamination test, the paper sample is sandwiched between two adhesive tapes and the ends of which are pulled apart until the paper begins to split. At this instant, the force required to complete the fracture is recorded. This technique measures the inter-fibre bond breakage energy and the energy dissipated within the fibre network [15]. In the z-directional tensile, double sided adhesive tape is applied on both sides of a paper sample, and the assembly is then inserted into a tensile test apparatus. The failure strength as well as the energy of intra-fibre bond failure are measured [15]. In the Scott bond test, an impact testing method, a paper sample is

placed within a frame, and a pendulum is released to strike the upper edge of the frame. This apparatus is used to measure the loss of potential energy due to the resistance of paper to splitting. Of the three tests, the Scott test seems most affected by basis weight, and by the dynamic nature of the test thus overestimating the bond strengths [15]. According to Koubaa and Koran [15], the z-directional tensile strength seems to be the most suitable measurement technique for measuring the internal bond strength of high-basis-weight papers.

Relative Bonded Area The extent of bonding in paper is usually described by the term Relative Bonded Area, RBA, which is the ratio of the bonded surface area to the total surface area of the fibres [16]. As discussed above, the RBA is a strong predictor of the strength of paper. However, measurement of the RBA is not a straightforward task, and can be measured either by direct or indirect methods.

Indirect methods for RBA measurement use either gas adsorption or optical light scattering techniques. The gas adsorption method utilizes a measure of the adsorption of nitrogen gas in a paper sheet as a proxy for the non-bonded surface area of the sheet [17, 18]. In this method, the total surface area can also be measured using non-bonded handsheets formed in acetone and butanol [18]. However, the total surface area is the surface area accessible to the gas which can also include the internal lumen area and the pores in the cell wall [19]. The light scattering method of Ingmanson and Thode [20] is based on the assumption that only the free surface area of the fibres can scatter light. In this case a lower light scattering coefficient translates to a higher degree of bonding. Then, the total surface area calculation is based on the assumption that there is a linear correlation between the light scattering coefficient and tensile strength, and the total surface area can be determined by extrapolating the light scattering coefficient to zero tensile strength. Although both methods have found widespread usage in research and in industry, the way of determining the total surface area has become a subject of debate [19, 21]. It is argued that refining and pressing can introduce additional differences in paper samples such as fibrillation and lumen collapse that can also affect the light scattering. Batchelor and He [21] recently developed a new method to calculate the RBA of non-bonded sheets without the need for extrapolation of light scattering coefficient by using available experimental data:

fibre cross-sectional area, cell wall density, area of a rectangle circumscribing the fibre, fibre wall area, and the density of the sheet. This method seems to produce adequate results.

Direct methods for RBA measurement are based on image analysis and microscopic studies of paper cross-sections. However, most of the macroscopic studies face difficulty in producing sufficiently high resolution images of the paper cross-sections [19]. Only recently, the development in X-ray micro-tomography has made it possible to produce high resolution 3D images of the paper sheets that can be used to measure the extent of fibre-fibre contacts in them [22]. However, to study the fibre-fibre contacts from 3D images, one needs to segment all individual fibres, which means assigning to each image element a label that indicates to which object it belongs. It is also quite unclear exactly what constitutes a fibre-fibre bond, since it will depend on the image resolution. Several automatic methods to segment paper fibres have been developed that are mostly based on lumen tracking [23, 24]. In the method developed by Sharma et al. [24] RBA is calculated via counting the contacts between the segmented fibres. Malmberg et al. [22] has developed a method to measure RBA without fibre segmentation only by detecting fibre lumens in cross-sectional images of the 3D volume which in principal is similar to the light scattering method. More information about X-ray tomography of paper and related image analysis methods are provided in the Image Analysis section of this chapter.

1.1.1.3 Tensile Deformation and Failure of Paper

Load-elongation curves obtained from standard tensile tests are one of the main tools to study the deformation of materials. Despite the fact that paper is heterogeneous at all levels of its structure, it still exhibits a well-defined load-elongation curve that can be used to describe its mechanical behaviour. The load-elongation curve of paper has two distinct features when testing is carried out in a dry atmosphere (relative humidity below 80%) [25]. As seen in Figure 1.1, the initial response of paper to a tensile load is an elastic behaviour. This initial linear response is followed by the plastic region which is associated with a gradual decrease in the slope of the curve that usually approaches a reasonably constant secondary slope [25]. Further, paper also show behaviour that is typical of visco-elastic materials, such as a dependence of

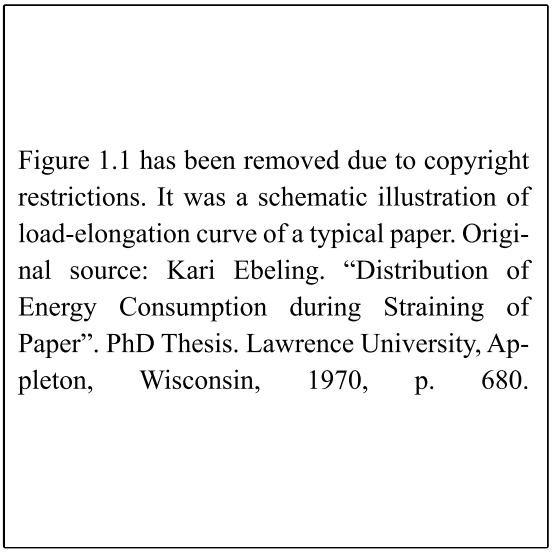

Figure 1.1: Schematic load-elongation curve for a typical paper [25]

the load-elongation curve on strain rate, creep, and stress relaxation [26].

Elasticity As explained in Section 1.1.1.1, through extensive experimental studies, Page and Seth [7, 8] were able to elucidate the factors that affect the elastic response of paper leading to the equation 1.1. They showed that the elastic response of paper depends on two factors: the elastic properties of the constituent fibres, and the sheet structure. The structural factors includes the orientation distribution, fibre length, and the relative bonded area of the paper network. They also showed that when the fibres are long enough, and the network is highly bonded the elastic modulus of a paper should approach one-third that of the component fibres. Consequently, the elastic modulus of random sheets can be simply described by,

$$E_p = \frac{1}{3}\,\varphi\,E_f \tag{1.3}$$

where, φ is the efficiency of the network and has maximum value of 1.0 for sheets of well-bonded long fibres.

Viscoelasticity-Plasticity The literature regarding the visco-elastic and plastic behaviour of paper contains two drastically different viewpoints. The first viewpoint, hypothesized by Rance [27], believes in disruption of inter-fibre bonding throughout the whole deformation process of paper. In this viewpoint, fibres are considered to be

perfectly elastic and inter-fibre bond breakage is believed to control the rate of the response, or in other words, the visco-elasticity of paper. This viewpoint is supported by the work of Nordman et al. [28] that used optical scattering to show that paper suffers from inter-fibre bond breakage during deformation. However, as they only reported indirect evidence, there were some questions regarding the inter-fibre bond breakage being the true source of the change in light scattering coefficient. Further, Page et al. [29] performed some direct microscopic observations of the inter-fibre bonded areas during straining of a paper. They reported that a vast majority of the analyzed bonds showed little to no loss in the bonded area and only a few of them showed full failure during deformation. The second viewpoint, first hypothesized by Berzinski [30], believes that the plastic deformation of paper is not influenced by inter-fibre bond breakage but is only governed by the irreversible intra-fibre deformation of the cell wall structure. This viewpoint has been supported by the work of Kubát [31], and Page et al. [32]. Finally, Ebeling [25] has also studied the thermodynamic behaviour of paper during the load-elongation and hypothesized that the load-elongation response of paper was governed by both intra-fibre irreversible structural changes and subsequent partial breakage of inter-fibre bonds.

One of the most complete research on the stress-strain behaviour of paper was conducted by Seth and Page [8]. In this study, different paper sheets with different levels of inter-fibre bonding were generated by varying the wet pressing and refining conditions, and through the use of additives. It was reported that the level of the inter-fibre bonding had no influence on the shape of the stress-strain curve as long as there was adequate level of bonding to create a fully efficient structure. The level of bonding only seemed to affect the strain to failure and the strength of the paper sheets. The change in the light scattering coefficient was also measured for different sheets, and it showed a decrease in RBA during straining at a rate which depended on the treatment that was applied to the sample. The sheet with the lowest bonding level showed the highest rate of RBA loss. Figure 1.2 shows the stress-strain curve for three samples of their study [8]: a control sheet indicated by the letter C, a sheet treated with a bonding agent indicated with the letter B, and a sheet treated with a debonding agent indicated by the letter D. The right-hand vertical axis indicates the corresponding light scattering coefficients recorded during straining. As can be

Figure 1.2 has been removed due to copyright restrictions. It was a digram of stress and light scattering coefficients plotted against strain of the samples that were controlled, treated with debonding and bonding agents showing how the light scattering coefficiencts increase more rapidly for the sample treated with a debonding agent. Original source: R S Seth, D H Page, and J Brander. "The Stress Strain Curve of Paper". In: The Role of Fundamental Research in Paper Making. Vol. 1. 1981, pp. 421–452.

Figure 1.2: Stress-strain curves and scattering coefficient for C-control, B-treated with a bonding agent D-treated with a debonding agent [8]

seen, while the shape of all three stress-strain curves is the same (only the failure point is affected), the increase in scattering coefficient is much larger for the sample treated with a debonding agent as compared to the sample treated with a bonding agent. Therefore, it was concluded that the pre-failure behaviour, and subsequently, the stress-strain behaviour of paper sheets are not affected by bond strength.

Further, since in the plastic regime the flow stress also is dependant on the visco-elastic properties of fibres, in addition to the sheet structure and the efficiency factor, Seth and Page [8] proposed that an equation similar to equation 1.4 could be used to describe the plasticity of paper:

$$E_p{}^\star = \frac{1}{3}\,\varphi^\star\,E_f{}^\star \tag{1.4}$$

where $E_p{}^\star$ and $E_f{}^\star$ now represent the value of stress divided by strain at any point on the stress-strain curve, and $\varphi^\star$ now represents the strain-dependent efficiency factor. The change in the orientation of the fibres is thought to be negligible and the efficiency factor is thought to decrease because of inter-fibre bond breakage. Following the same rationale, they showed that by using an efficiency factor calculated by dividing the elastic modulus of an inefficient structure by the elastic modulus of an efficient structure, the stress-strain curves of paper networks with different network efficiency superimpose on each other as long as the fibre properties stay the

Figure 1.3 has been removed due to copyright restrictions. It included two diagrams: (a) showed the plots of the stress-strain curves for different samples with different wet pressing pressures and how the curves are different, and (b) showed that the stress-strain curves of all the samples superimpose with only difference between them being the strain to failure values. Original source: R S Seth, D H Page, and J Brander. "The Stress Strain Curve of Paper". In: The Role of Fundamental Research in Paper Making. Vol. 1. 1981, pp. 421–452.

Figure 1.3: (a) Stress-strain curves for handsheets made with different wet-pressing pressures from laboratory-made, never-dried, unbleached, 46%-yield kraft pulp of black spruce (b) The same stress-strain curves superimpose when the efficiency factor is considered [8]

same. Therefore, they concluded that the non-linearity of the stress-strain curve of paper and its visco-elastic properties originate from the intra-fibre processes and that the inter-fibre bond breakage only plays a minor role in the stress-strain evolution through a slight reduction in the network efficiency during deformation. Figure 1.3 (a), redrawn from the work of Seth and Page [8], shows the stress-strain curves of different samples made with different levels of wet-pressing. Figure 1.3 (b) shows the same stress-strain curves that superimpose when the efficiency factor is applied, thus demonstrating the superimposition theory proposed by Seth and Page.

Failure Analysis There are two main mechanisms that govern the fracture of paper: fibre pull-out, where breakage of a series of inter-fibre bonds result in fibres being pulled out of the paper network during deformation and failure, and fibre breakage, where the fibres inside the fracture zone break due to high tension inside their fibre walls. Different experimental methods have also been developed to study the fracture process in paper. Kettunen and Niskanen [33] have developed a geometric method to characterize the microscopic damage that results from inter-fibre bond failure and fibre pull-out caused by propagation of a crack through paper. In this method, the

area that the fracture takes place and proceeds is called the Fracture Process Zone, FPZ. The method involves measurement of two parameters: damage width w_d, that characterizes the extent of inter-fibre bond breakage near the crack line, and pull-out width W_p that characterizes the fibre pull-out by measuring the distance that the fibre ends extend from the crack line on both sides. The measurement is performed on silicon-impregnated samples, as silicon enhances the contrast of newly created surfaces that allows for identification of inter-fibre bond or fibre failures. Further, Zhang et al [34] applied this damage analysis method to compare the effect of wet straining and refining on the fracture properties of paper and showed that the ratio of damage width to pull-out width may be reflective of the degree of fibre segment activation.

Acoustic Emission (AE) monitoring has also been applied in investigation of damage processes in paper [35, 36, 37]. Isaksson et al. [36] used AE monitoring to study the onset and evolution of damage in isotropic paper sheets with inter-fibre bond breakage as their dominant damage mechanism. Detected emitted waves in AE monitoring are considered to be the consequence of rapid release of elastic energy originating from micro failures. Figure 1.4, redrawn from their study, shows the typical experimental (σ) and theoretical ($\hat{\sigma}$) stress-strain curves obtained from the uniaxial strain tests in [36]. As can be seen, the normalized cumulative number of AE events and the calculated homogeneous damage variable D is also plotted as a function of uniaxial strain ε. The theoretical stress-strain curve is calculated by extrapolation obtained from a curve fitting relation and damage variable D is calculated as $D = 1 - \sigma/\hat{\sigma}$. Close agreement of the curves for the damage parameter and the normalized cumulative number of AE events demonstrated the use of detected AE to indicate damage growth in paper specimens where inter-fibre bond breakage is the active damage mechanism.

Fracture Mechanics of Paper In recent years, in addition to the idea of network efficiency, the idea of fracture sensitivity has gained increasing attention which is based on the notion that tensile strength of paper is a measure of paper's ability to concentrate strain energy resulting in development of fracture-based models of tensile strength [38]. It has been reported that linear elastic fracture mechanics (LEFM) modified for paper [39], and an extended fracture process zone length (FPZ) [40], is

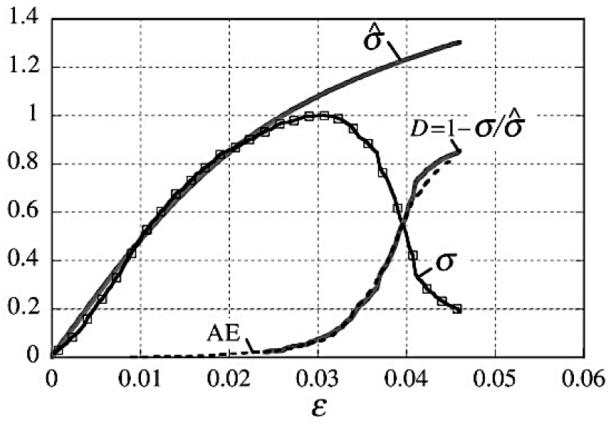

Figure 1.4: Typical experimental and theoretical stress-strain curves obtained from uniaxial strain test on isotropic paper sheets along with the normalized cumulative number of AE events and the calculated homogeneous damage variable D as a function of the uniaxial strain [36]

sufficient to describe the fracture resistance for a wide range of paper grades [41]. Coffin et. al. [41] showed that for a wide range of commercial papers a sample width of 50 mm is enough to determine the effective process zone length, and the obtained results can be scaled to allow for prediction of fracture sensitivity of wider webs. The measured FPZ, or in other word, the effective process length parameter was taken as a measure of papers ability to concentrate load near the crack tip that has a great influence on the fracture resistance of a paper sheet relative to its tensile strength. They also argue that the tensile strength of paper is a result of a fracture process mainly induced by the defects along the edges of paper sheets which are introduced via cutting of the network. Therefore, tensile strength is simply the result of the same type of fracture process that happens in a notched test. This idea resulted in application of a flawed lattice model to study the effect of a discrete structure on the fracture sensitivity, which showed that the smaller lattice spacing resulted in concentration of load closer to the crack tip. This way they concluded that the FPZ used in modified-LEFM is not necessarily a physical length of the extended fracture zone length, but a characteristic length of the network that can be used to describe the ability of the structure to concentrate energy. Therefore, a fracture-based model can be used to model the tensile strength loss of a network based on this characteristic length rather than bond strength as in Page's equation for tear strength. Coffin [38]

also measured characteristic length of 37 market pulp for a set of beating curves and reported the existence of a unique shape to the curve of the normalized tear strength when plotted against their characteristic length. This plot showed that the tear strength decreases significantly when the characteristic length is smaller than the fibre length. He interpreted the observed trend as that the tear strength peaks when the unit cell is of the order of the fibre length and further densification of the paper network results in smaller effective unit cells that similar to the result of the lattice model will lead to more strain concentration quickly diminishing the tear strength. In other words, he explained that tensile strength and tear strength appear to be influenced by the ability of the network to concentrate and transfer strain energy from one unit to another, and therefore, once the characteristic length is less than the fibre length, the ability of the network to concentrate energy is sufficient to propagate fracture without engaging the surrounding material resulting in higher fracture sensitivity to smaller tears and less energy required for tearing. Therefore, he concluded that for networks of large inherent lengths, such as low grammage and low bonding sheets, sample size needs to be considered even when a standard sample width of 15 mm is used as they would not yield an accurate measurement of tensile strength.

1.1.1.4 Auxetic Behaviour of Paper

Similar to other materials, deformation of a paper sample under uniaxial loading is three dimensional, which means that paper not only deforms in the direction of the load, but also exhibits signs of deformation in the transverse directions. This effect is known as the Poisson effect, and quantified as,

$$\nu = -\frac{\Delta d/d}{\Delta l/l} \tag{1.5}$$

where ν is the Poisson's ration, d is in this case the initial thickness, l is the initial length of the sample, and Δd and Δl are changes in the thickness and length of the sample.

Auxetic materials are a specific class of materials that exhibit expansion in the transverse direction during a uniaxial tensile loading. This thickness expansion during uniaxial tensile loading have also been observed for different kinds of paper and

reported in the literature [42, 43, 44]. Öhrn [42] measured thickness change by three different types of instruments: a continuous thickness gauge made of a metallic circular platen with a diameter of 2.7 cm, a mercury dilatometer [45] measuring thickness as a function of volume change of liquid mercury, and a Microcator [42] that measures thickness during a biaxial bulging of paper. Öhrn tested four types of papers and found all of them to show an increase in the thickness with increasing strain. He measured the thickness of samples until failure and even after failure and found that the thickness curve was concave upward for all samples. Stenberg and Feller [43] used a bespoke thickness measuring device with a spherical platen head to continuously measure the thickness of the samples over an area of about 20 cm^2 of paper while being strained in a tensile tester. The overall thickness of the samples was reported to increase with increasing strain. No correlation were found between the Poisson's ratio with either grammage or the initial thickness of the samples and no discussion was provided on the effect of processing parameters.

In addition to all the above mentioned experiments, where mechanical contacts were used to measure the change in the thickness of samples, image analysis can also be used to measure such changes. Post et. al. [44], used optical imaging along with some image analysis to measure the thickness change of different paper samples during tensile testing. They reported an increase in the thickness for few samples made from Kraft pulp and also some multi-ply boards. However, as the thickness measurements were calculated from images of the cut edge of the samples, any misalignment, rupture, or buckling of the sample could significantly influence the thickness values.

As can be seen from equation 1.5, expansion in the thickness direction occurring concurrently with tensile deformation results in a negative Poisson's ratio, which is a typical characteristic of auxetic materials [46]. In contrast, most monolithic materials (e.g. metals, ceramics, and polymers) show a positive Poisson's ratio, which means that a stretch in one direction induces a contraction in the lateral directions. Although auxetic materials also elongate in the direction that they are being stretched, unlike regular materials they show expansion in either or both lateral directions. Auxetic behaviour can be both naturally occurring, as in certain types of skin and load-bearing bones, and synthetically induced, as in honeycomb structures and fibre-reinforced composites. Depending on the type of the material, different mechanisms are believed

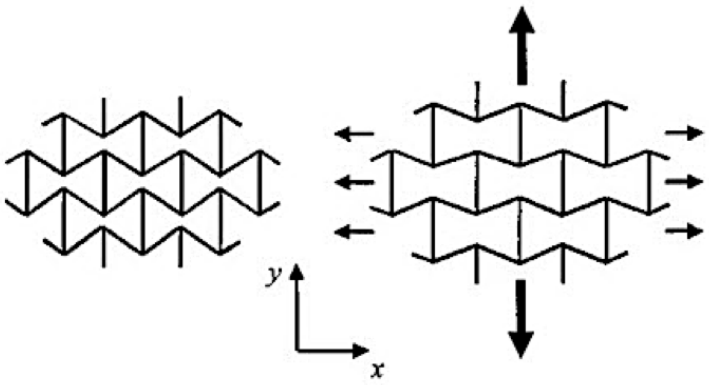

Figure 1.5: Re-entrant honeycomb network structure with negative Poisson's ratio (auxetic) [46]

to be responsible for their auxetic behaviour [46]. A simple mechanism for auxetic behaviour can be observed in the re-entrant honeycomb structure. As can be seen in Figure 1.5, the special form of the structure will result in an expansion in the y direction when the structure is stretched in the x direction.

As mentioned earlier, the out-of-plane Poison's ratio of paper have been measured to be negative, and therefore, paper can be considered as an Auxetic material. Straightening of the curved fibres have been widely accepted as the mechanism responsible for the auxetic response of paper [42, 43, 44]. In a recent work, Verma et. al. [47] have tried to build up on the existing knowledge and further explain this phenomena by developing a simple geometrical model using cylindrical fibres. Figure 1.6 shows a schematic view of their network model along with its cross-sectional view at stretched and non-stretched states. They hypothesized that when the network is stretched, the relaxed and flexible fibres are pulled at the network points pushing the fibres that are bonded or in contact with them in the z-direction resulting in an increase in the thickness of the network. It is therefore suggested that the bonded contacts make this phenomena more pronounced, since otherwise fibres would slide past each other. Consequently, by filling the voids of the network they would not be able to contribute to the thickness expansion. Using such geometrical model, Verma et. al. showed that, similar to paper, the magnitude of the negative out-of-plane Poisson's ratio of their model increases with increasing strains, consistent with experimentally obtained values [42].

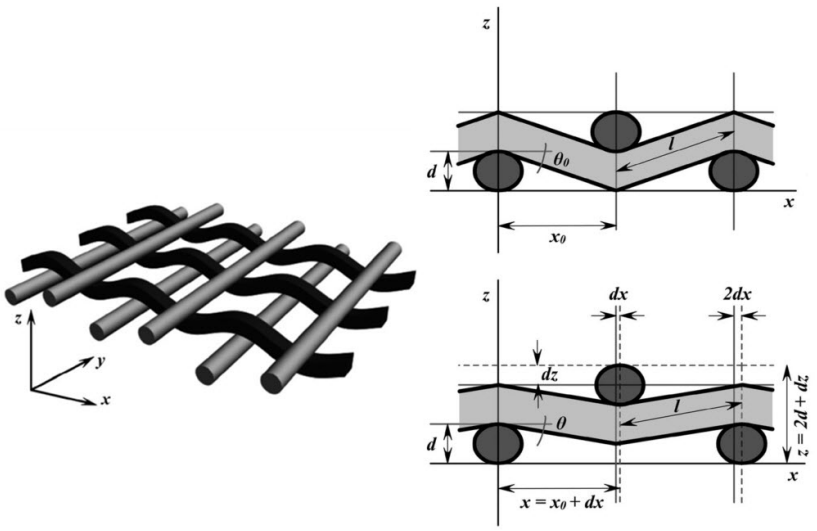

8

Figure 1.6: Network structure (left) and its cross-sectional view at non-stretched (right-upper) and stretched states (right-bottom) [47]

1.1.2 Factors Affecting Fibres and Bonding

As explained in section 1.1.1, the properties of the constituent fibres and their interactions, namely inter-fibre bonding, are the two major factors that affect the strength properties of the final paper products. These factors can be influenced by different processing steps that help tailor the final products for specific applications. In the present research, three processing methods have been used to alter the mechanical properties of paper handsheets: refining, where mechanical treatment of fibres is used to alter their properties; drying, where fibre properties and bond formation can be influenced by changing drying conditions; and pulp mixture, where paper properties are altered by using blends of different fibre types that inherently have different properties. All these factors are explained below.

1.1.2.1 Refining

The refining process or "beating" of chemical pulps is a mechanical treatment to design the fibres to better satisfy the requirements of the paper-making process such as drainage characteristics, or the desired properties of the final paper product including certain strength properties [48, 49]. In the refining process, the fibres are subject to compressive and shear forces that can result in several changes in fibre characteristics

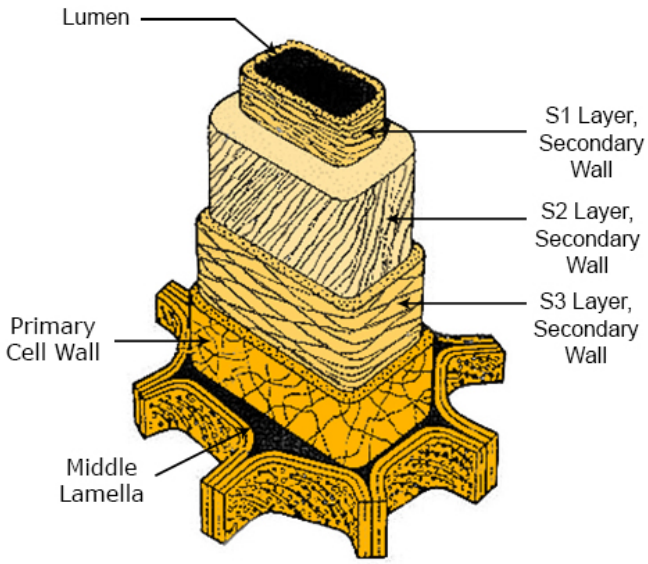

Figure 1.7: Schematic drawing of a wood fibre structure [53]

which depend on the type of initial fibres, refiner specification, and pulp consistency. Pulp consistency is defined as the weight in grams of oven-dried fibre in 100g of pulp-water mixture, based on which refining processes are usually divided into low or high consistency methods.

In order to understand the effect of refining on paper properties, its effect on fibre properties have to be clarified, which necessitates a basic familiarity with the wood cell wall structure. The cell wall structure of wood fibres consists of several layers [50]: middle lamella, primary cell wall, secondary wall, and lumen. Figure 1.7 shows a schematic drawing of the structure of a wood fibre. As can be seen, the primary and secondary cell walls contain a scaffold of cellulose microfibrils with middle lamella surrounding the primary cell wall. Middle lamella mainly consists of lignin that is holding the fibres together in wood, along with some primary cell walls of adjacent fibres. The secondary cell wall is the main contributor to the mechanical properties of the fibre, and contains three different layers [51]: the outermost layer called $S1$, the middle layer called $S2$, and the innermost layer called $S3$. The Microfibril Angle of the secondary wall layers is known to be the main reason behind the difference in elasticity, shrinkage, and collapse resistance behaviour of different types of wood fibres [52]. The last layer of the cell wall is called the lumen, which is the hollow core and can hold water or water vapour.

Fibrillation The first effect of refining on paper fibre is internal fibrillation caused by cyclic action of forces that rise during the refining process. This results in delamination of the P and $S1$ layers of fibres, causing the breakage of inner bonds that exist among different fibre wall layers. Further, this results in the expansion of the pore structure inside the cell wall that leads to swelling of the fibre [54], which is indicative of damage in the fibre wall. Finally, degradation of the fibre wall during internal fibrillation causes the fibres to be more flexible or conformable [55]. The loosening of the fibre wall results in a reduction of the effective elastic modulus that further reduces the bending stiffness of the fibres. Flexibility is one of the key factors in determining the final strength of a paper product since more flexible and collapsed fibres result in higher contact areas between fibres and lead to stronger bonding that in turn results in higher tensile strength [56, 57].

Another effect of refining, especially when the shear rate in refining is low, is external fibrillation, which is associated with the shearing of the fibre surface that results in exposure of the microfibrils still attached to the surface of the fibres [58]. This results in an increase in the specific surface area of pulp fibres that are believed to improve the fibre–fibre bonding [59, 60]. Further, some hydrophilic compounds from the cell wall are released during the external fibrillation process that leads to the formation of some gel-like layers that appear as a thin layer after drying that can influence the fibre-fibre bonding [60]. As internal and external fibrillation happen simultaneously during the refining process, it is difficult to determine the effect of each one individually. However, the application of ultra-fine friction grinding has made it possible to keep internal fibrillation constant while observing the effect of external fibrillation on strength properties [61]. This resulted in the observation that external fibrillation, in addition to internal fibrillation, will significantly increase the tensile and bonding strength.

Fine Formation and Fibre Shortening In general two types of fines can be present in pulp: primary fines and secondary fines. Primary fines are present even in unbeaten pulp and stem from the ray and parenchyma cells [62] while secondary fines are produced during the refining process as a result of fibre shortening or external fibrillation [63]. Fines consist of fragments of primary and secondary fibre walls with

a high surface area that can improve the fibre-fibre bonding, but at the same time they can increase the draining time.

A reduction in the fibre length during the refining process is called fibre shortening [64]. While fibrillation is caused by a large number of impacts of small intensity, a small number of high intensity impacts can lead to fibre cutting [65]. Fibre cutting is usually an undesirable effect of refining as longer fibres result in higher tensile strength in paper sheets [66]. However, the shortening of fibres can improve sheet formation considerably due to decrease of flocculation tendency by reducing the crowding number [67]. The fibre length reduction as a result of refining is calculated by measuring the length weighted average fibre length before and after the refining process. It has been reported that the reduction of fibre length did not actually correlate with the changes in the number of long fibres in the unit mass, suggesting that there might be a relation between fines formation and fibre shortening [68].

Fibre Straightening Another major effect of the refining process on the fibre morphology is fibre straightening [69]. Although the exact mechanism of fibre straightening during refining is not clear, breakage of the intra-fibre bonds, swelling of the fibre walls along with the tension in the refiner gap are thought to be the main mechanisms associated with fibre straightening [70].

As pulp travels through different high consistency mechanical treatments it may be subject to bending or axial compressive stresses. Lamellar structures of wood fibres that consist of helically wound fibrils results in them being fairly strong in tension, while they easily fail under longitudinal or axial compression. Axial compressive failure in fibre results in regions where the original orientation of the fibrils are locally disturbed, and give rise to *microcompressions* [71] which is defined as axial shortening of fibres due to introduction of slip planes and dislocations. Further, the bending failure of fibre can result in large-scale deformations in the fibre wall that are accompanied by delamination. This leads to development of regions that have low bending stiffness. Fibres have a tendency to develop kinks at those sites, where the direction of the fibre axis changes abruptly. It is because of these deformations along the length that a fibre becomes curly [72].

Straightness of fibres can have a major impact on tensile strength and modulus

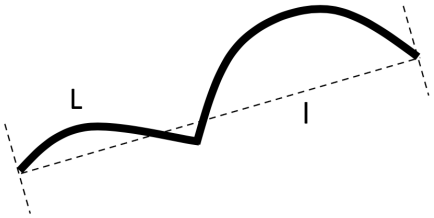

Figure 1.8: Illustration of fibre curl

of the final paper sheet [71]. Considering that paper consists of a network of fibres that bond together at fibre-fibre crossings, the fibre segments that are curved do not contribute to the load transfer in the network until deformation straightens them. Consequently, stress distribution within the network becomes uneven, leading to stress concentration and therefore a reduction in in-plane strength. The straightness of fibres is measured using a parameter called *curl index*, which is defined as the relationship between the "contour length", and the "projected length", as shown in Figure 1.8 and calculated as [71],

$$Curl\,index = \frac{L}{l} - 1 \tag{1.6}$$

where L is the contour length and l is the projected length.

1.1.2.2 Pulp Mixture

Most of the research on the effect of pulp blends on paper properties are focused on investigating the usefulness of the general mixture rule in predicting the properties of mixture sheets. The most basic form of the mixture rule is the linear regression model, which approximates the mixture properties by summing the products of the properties and weight fractions of each constitutive phase [73]. For example, Gates and Westcott [74] performed a theoretical study on the application of a linear mixture rule (i.e. mass fraction additivity) for calculation of RBA for a paper that consists of two components. Using statistical mechanics of fibres in the network, they were able to develop the following relation

$$RBA = \frac{w_1 RBA_1}{w_1 + w_2\alpha_1} + \frac{w_2 RBA_2}{w_1\alpha_2 + w_2} \tag{1.7}$$

where w_1 and w_2 are the mass fractions, and RBA_1 and RBA_2 are the relative bonded areas of the two components. α_1 and α_2 are factors that consider the RBA, and width and thickness of the collapsed fibres of the pulp components. However, they found that this relation is not always true and some mixtures do not follow the linear mixture rule. They also concluded that when the RBA deviates from this linear mass fraction additivity rule, tensile strength of mixtures also deviate from the linear mixture rule. Similarly, Mohlin and Wennberg [75] observed synergistic effect for tearing resistance in a mixture of chemical and mechanical pulps. However, the tensile properties and internal bond strength was reported to show negative deviation from the linear additivity. Weak interactions between the chemical and mechanical fibres was suggested to result in formation of two separate networks in the mixture leading to such non-linear patterns. Retulainen [76] also observed a negative non-linear deviation from linear mass fraction additivity for the apparent density of blends of earlywood and latewood kraft fibres in mechanical pulps. Tearing resistance was reported to increase linearly with the addition of latewood fibres but showed a positive deviation when more flexible earlywood fibres were added to the mixture. It was suggested that the stiffer fibres had undermined the ability of bonding of more conformable fibres, and therefor, the Kraft fibres were under utilized. In contrast, both linear and non-linear behaviour of the strength properties in sheets consisting of Kraft and TMP was observed by Zhang et al. [77]. It was suggested that the behaviour was dependent on the degree of bonding in the sheet. When the bonding potential of both pulps was fully utilized, a linear relationship in the strength properties was observed, while a deviation, generally negative, was seen when the bonding potential was not fully utilized.

Some properties of the mixtures of separately refined chemical softwood and hardwood pulps also have been reported to deviate from the linear mixture rule. The tensile, tear and folding strengths, light scattering and opacity of the mixture can show synergistic effects while air permeability have been shown to deviate negatively from the calculated values [78, 79, 80]. In contrast, the breaking length, and the stretch of the mixture have been reported to follow the linear additivity rule [80]. Bovin and Teder [78] have found that if their tensile strengths are on different sides of the tear strength maximum on their tensile-tear strength curves the tear strength of

the mixtures of any different chemical pulps show positive deviation from the linear mixture rule.

1.1.2.3 Drying

As explained in section 1.1.1.1, inter-fibre bonding is a major factor contributing to strength properties of paper networks. Inter-fibre bonds form due to a phenomena known as the Campbell Effect [13] that arises from the capillary forces during the drying process that pulls the fibres together. As the drying process continues, this effect leads to different kinds of bonding between fibres including Molecular bonding and Van der Waals' bonding. The extent of inter-fibre bonding formed during this process can also be influenced by the method of drying. In general, drying can be categorized into two types of *free drying*, where paper sheets are allowed to shrink freely during drying, and *restrained drying*, where shrinkage of paper sheets during drying is inhibited. During drying, pulp fibres have different tendencies to shrink laterally or longitudinally [81]. The amount of shrinkage depends on the amount of wet swelling of the fibre walls that is in turn dependant on the internal fibrillation, and chemical composition of the fibre walls. As a result of this discrepancy, pulp fibres shrink more laterally leading to shear stress at the bonding area. Therefore, when a paper is loaded, the edges of the bonds will be the first area to start carrying the load [81]. Lateral shrinkage of one fibre also leads to axial shrinkage of the bonded fibre, causing microcompressions in the bonding region. Consequently, the properties of the bonded fibres differ from those that are freely dried. In contrast, when the drying is restrained, the axial compression in the bonded area inflicted by neighbouring fibres leads to activation of some fibres in the network as shown in Figure 1.9. Activation refers to the event when originally kinked, curly, and deformed fibres that are unable to carry any load, are transformed into active components of the network. In addition, Jentzen [82] found that drying under axial tension can substantially increase the tensile strength but decrease the breaking length of single fibres. This change in mechanical properties is associated both with an increase in the crystalline orientation (that enables higher tensile strength and Young's modulus) as well as a more even redistribution of stress in the fibres brought upon by a removal of internal deformations [83, 82].

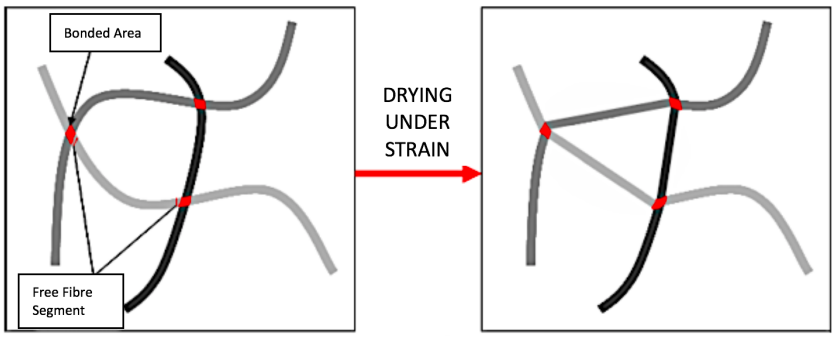

Figure 1.9: Schematic illustration of network activation [81]

Finally, paper can also be *freeze-dried*, where the wet handsheet is initially frozen and then sublimed under vacuum condition. This method is known to eliminate the surface tension effect during the drying process, inhibiting the Campbell effect [84, 85]. This results in the freeze-dried samples to have lower degrees of bonding, and consequently, lower tensile strength properties when compared to air-dried samples.

1.1.3 Image Analysis

Considering the great importance of the fibre network on properties, direct observation of this network, and changes that occur with deformation, will help to improve our understanding of the process-structure-properties relationship in paper. Different image acquisition methods have been employed to study paper, and are summarized in [86]. While most of these imaging methods are suitable to study the surface of a paper, a few of them can also be used for 3D analysis. Among these methods, the non-destructive and high-resolution nature of X-ray Computed Tomography (CT) has made it the method of choice for 3D analysis of paper microstructure [87]. In doing so, the next section will provide a brief explanation of the X-ray tomography methodology. The following sections will then explain how image analysis techniques can be applied to the acquired 3D images to analyze the structure of paper. The last section will focus on the use of X-ray computed tomography to acquire time-dependent data sets that can further facilitate the study of paper's mechanical behaviour.

1.1.3.1 X-ray Tomographic Imaging of Paper

X-ray Computed Tomography (CT) imaging has been used for more than 40 years in medicine, and has developed to be a powerful technique to study materials over

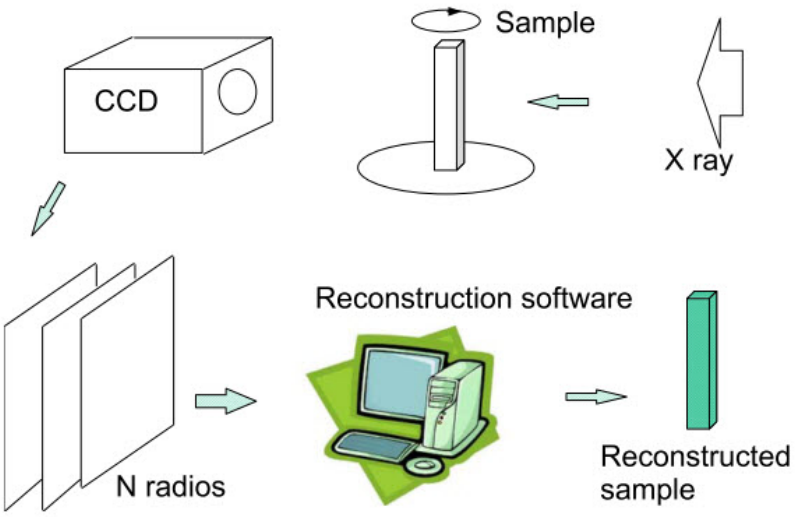

Figure 1.10: Schematic illustration of the principles of X-ray tomography [90]

the past 15 years. Figure 1.10 shows a schematic illustration of the process of X-ray tomography in a non-medical setting. As can be seen, the sample is placed between the source and the detector. Then, the sample is rotated and a series of radiographs is acquired. Then, these images are used to reconstruct or compute the 3D dataset of the internal structure of materials [88]. The image contrast is obtained based on variations in X-ray attenuation within the studied sample. Attenuation of X-ray by each element within a sample is governed by its characteristic X-ray attenuation coefficient μ[89]:

$$I = I_0 e^{-\mu t} \tag{1.8}$$

where I_0 is the intensity of the incident beam, and I is the intensity of the X-ray beam after passing through a material with thickness t. This equation can be extended to a three dimensional space:

$$I(x, y, z) = I_0 e^{-\int_0^z \mu(x,y,z)dz} \tag{1.9}$$

where (x, y, z) determine the position inside the specimen. Therefore, the resultant x-ray intensity $I(x, y, z)$ is a measure of the attenuation coefficient as a function of the position inside the specimen. Solving this equation for μ results in a three dimensional volume consisting of attenuation coefficients of materials inside the scanned specimen which are proportionally represented by different greyscale values.

In addition to the absorption mode, the contrast of the images can also be obtained by phase contrast. Phase contrast exploits the Fresnel diffraction of the X-rays and

maps the difference in the refractive indices of materials inside the sample [91]. In this way it can enhance the visibility of the edges and boundaries of the objects that have similar X-ray attenuation coefficients. It can also be useful in imaging of materials that have very low X-ray attenuation. For example, in paper materials the low attenuation of cellulose fibres makes it difficult to differentiate the fibres from voids (i.e. air) via absorption mode CT, and therefore, phase contrast can be a useful method for imaging of such materials.

The X-ray source can also significantly affect the quality of the obtained images and synchrotron radiation can offer significant improvements when compared to laboratory X-ray sources. While X-ray tubes are normally used in lab-based equipment, synchrotron uses synchronized magnetic and electric fields to accelerate charged particles in a ring-shape path that results in a nearly parallel beam propagation with a flux many orders of magnitude higher than that of lab-based X-ray sources. The parallel nature and the high flux of such beams translates to faster scan times [92]. The high intensity of the synchrotron beams also facilitates the application of filters providing the possibility to work with a monochromatic beam resulting in scans that suffer less from X-ray artifacts such as beam hardening [92].

Synchrotron X-ray Computed Tomography of Paper Synchrotron X-ray Computed Tomography (sCT) has been widely used to study the structure of paper [87, 93, 94, 95, 96]. The usefulness of sCT to study paper structure at the micrometer level was first examined by Samuelsen et. al. [96]. Antoine et. al. [97] also used sCT with phase-contrast mode to obtain images of paper's 3D structure with a resolution of 1 μm. They found a series of artifacts and 'disturbances' in their data and proposed a set of image analysis routines to semi-automatically segment fibres and fillers from pores. Roscoat et al. [94] used a parallel, monochromatic synchrotron X-ray beam to obtain images of paper structure achieving a resolution of 0.7 μm. They realized that the sensitivity of paper samples to humidity and temperature can result in sample shrinkage during the scan that can lead to blurry images. They were able to overcome this problem by estimating the strain of the sample during the scan using a linear interpolation based on the cross-correlations between radiographs obtained at both 0 and 90 degrees. They also suggested conditioning samples by leaving them

in the experimental hutch for two days prior to the experiment in order to resolve the shrinkage problem. Further, using the acquired images they were able to segment and characterize the structure of paper samples in terms of their fibres, fillers and pores. In a later work, Roscoat et al. [87] used sCT to study porosity and specific surface area of four industrial paper materials. They analyzed the porosity profile in the thickness of each sample using the acquired 3D datasets and reported the thickness of paper sheets to consist of three layers: a bulk layer with almost constant porosity being sandwiched between two boundary layers that have strong porosity gradients.

In addition to bulk-level studies, sCT has also been used to study paper structure at the level of fibres and bonds [22, 98, 99]. Malmberg et al. [22] used phase-contrast sCT to study a series of wood-fibre mats. They developed a data reduction method to quantify the degree of inter-fibre bonding in their samples that only requires the identification of fibre lumens. Marulier [98] also used sCT to study paper's fibrous microstructure to shed light on the links between manufacturing conditions, and the resultant microstructural and mechanical properties. They adapted a manual segmentation approach to find centre lines of fibres that were further used to characterize the morphology of fibre cross sections and inter-fibre bonds. Wernersson et al. [99] also developed an algorithm with a graphical user interface that can facilitate a semi-automatic segmentation of fibres inside a X-ray tomography data. Segmentation is done by choosing a few control points along the fibre that represents the centre line of the fibre at each slice. Then, the rest of the fibre centre line is calculated by the algorithm using interpolation and splines. By using the segmented fibres the developed algorithm is able to identify where the fibres are free or bonded.

While manual or semi-automatic fibre segmentation methods have been shown to be effective in studying the microstructure of paper using sCT, segmentation of large number of fibres using such methods can not only be very time consuming, but also may result in user bias. This underlines the importance of development of robust automatic algorithms that can effectively segment individual fibres form tomographic data. Such data can be used to obtain statistically significant measurements of different fibre-level and network-level properties of paper.

1.1.3.2 Segmentation

As mentioned earlier, the data acquired from sCT is a three dimensional volume of greyscale values that proportionally represent the X-ray attenuation of the materials inside the scanned sample. The first step in analyzing such data is to distinguish the greyscale values that represent the paper material from background noise (i.e. air), which is known as Binarization. Doing so usually involves selection of a threshold value that separates ranges of the greyscale spectrum that are attributed to the regions of interest from the rest of the values. However, the low contrast of X-ray tomographic images of paper, especially at the fibre-air interface makes such selection of a global threshold value a challenging task [97]. Therefore, advanced filtering and denoising methods are usually first applied to sharpen the histogram of greyscale values, facilitating the binarization of tomographic datasets of paper.

Binarization Different denoising and binarization methods for tomographic images of paper samples have been suggested in literature [97, 94, 100]. Antoine et al. [97] proposed a multi-step method for binarization that included a low and high pass filtering, subjective selection of seed points, and thresholding by region growing. First, low frequency noise in the quasi-ring artifacts was removed by a smoothing procedure based on averaging five consecutive slices in one direction, while high frequency noise was removed by conventional Butterworth filter [101]. Then, a region growing method [101] restricted in only two directions and requiring the selection of several seed points was used to binarize the data. Roascoat et al. [94] used a non-linear anisotropic diffusion filter [102] and showed that application of such diffusion filters can result in smooth regions while preserving the edges. In that work, a semi-automatic seeded region growing method was used for binarization, which regroups the voxels based on their homogeneity and adjacency criteria. Recently, Sharma et al. [100] developed a multi-step method for binarization. First, a simple non-linear diffusion filter [103] was used to remove the noise while preserving the edges. Then, a threshold value was calculated in a way that the basis weight of the digitized volume would be equal to the physical basis weight of the sample. The digitized basis weight was calculated by:

$$w = \frac{N(T) \times (r)^3 \times \rho}{A} \tag{1.10}$$

where $N(T)$ is the total number of voxels with a greyscale value greater than T, r is the voxel size (i.e. the resolution of images), ρ is the density of cellulose (assume in Sharma's study to be $1.5\,\mathrm{g/cm^3}$), and A is the area of the sample. Using this equation, the value of T was calculated by equating the basis weight of the digitized paper with experimental measurements. It should be noted, however, that considering the locality nature of basis weight in paper, and the fact that the size of samples in X-ray tomography imaging are very small (i.e. in the order of few millimetres), the actual basis weight of the scanned sample might not be exactly equal to the measured basis weight of a standard sample.

Segmentation of Individual fibres After binarization, different image processing techniques can be used to segment individual fibres inside the volume. The term segmentation refers to the identification of regions of interest in digital images. Segmentation is quite important and has applications in many different fields, ranging from medical sciences, to robotics, and materials sciences, and thus a variety of segmentation algorithms exist in the literature. However, because of the complex morphology of paper fibres, adaptation of such algorithms to segmentation of paper fibres has been proven to be challenging.

An initial attempt at segmentation of individual fibres inside volume images of paper was made by Aronsson [23]. In this work, segmentation was initiated by manual definition of two seed points inside the lumens of paper fibres: the preferred start- and end- locations. Seeds were then grown in the direction of local fibre orientation using Ordered Region Growing (ORG) [104] along with a steering function defined by a Distance Transform (DT) [105] of the binary image. In this way, ORG tracks centreline of lumens throughout the 3D dataset that results in a 'wiggly' skeleton for each lumen. Then, using these lumen skeletons as seed voxels, a 3D segmentation method known as SeparaSeed [106] was applied to identify the entire lumen. Finally, a DT histogram based approach was used to segment fibre walls. This method successfully segmented 10-20% of the lumens in a dataset obtained by SEM and microtomy [23]. Lundén [107] and colleagues have also developed a similar method to identify lumen candidates, but unlike Aronsson's approach, this method does not assume a constant fibre wall thickness when segmenting fibres. In fact, lumen candidates are

grown outwards until an edge is detected using the Canny edge detector algorithm [108]. This method was able to capture any regions where the lumens had collapsed by first removing the previously identified regions and then using the remaining data as seed for edge detection in the original data. Another method that has been used to segment lumens in a volume image of paper was to track Maximally Stable Extremal Regions (MSER) [109]. MSERs are either bright regions surrounded by dark boundaries or dark regions surrounded by bright boundaries, and can be identified using extremal properties of the intensity function. A lumen being a dark region surrounded by a bright boundary, can in fact be identified by detection of MSERs. Therefore, simultaneous detection and tracking of MSERs between adjacent slices of a volume image can result in segmentation of 3D lumens [110, 110]. Such segmented lumens can further be used to segment fibres in a similar way as the previously mentioned approaches. Axelsson [111] has also developed a 'pre-segmentation' method that uses the local orientation of fibres. In this method, the first estimation of the fibre cross section is provided manually by identification of seed points that mark the approximate centre for each fibre. Then a local coordinate system is defined with the origin at the seed point and one coordinate axis along the approximate fibre direction. Next, a series of images are created using sum projections perpendicular to the fibre cross section by rotating the local coordinate system around the fibre axis. The sum projections are then radon-transformed [112] to identify the lines corresponding to the fibre walls. This can be done by locating the local maxima in radon transforms. These lines are then used to update the fibre axis and the centre points. Finally, a step is taken in the direction of the fibre axis and the new fibre axis and centre point is calculated in a similar fashion. The described method was shown to effectively find the centre lines of fibres; these can be used as seed data for segmenting fibre walls in a similar way as in [23]. However, this method only works for fibres with lumens since completely collapsed region of a fibre become a band in their radon transform, lacking the required local maxima. Among the mentioned methods for segmentation of individual fibres only the methods based on tracking of MSERs can be considered as automatic and the rest of them require manual indication of seed points for initiation. Attempts have also been made to automate other methods through automatic identification of lumen cross sections in two dimensional slices using different shape

descriptors and constraints [113, 114]. Simultaneous tracking and identification of lumens in adjacent slices can result in 3D segmentation of lumens that can further be used as seed for segmentation of fibres. A recent advancement in this area has been made by Sharma et al. [100] and can extract 40-50% of the fibres in a image volume. Sharma's method is utilized in the present study, and will be explained in more detail in the methods section of this thesis.

1.1.3.3 4D Imaging of Paper

4D imaging refers to performing some *in-situ* (or in other words time-dependant) analyses of materials inside X-ray chambers that has been made possible by recent advancements in fast synchrotron X-ray Computed Tomography (sCT). Nowadays 4D tomographic imaging can also be done inside lab-based tomography machines. However, since lab-scale CT equipment have limited X-ray flux their application in 4D imaging is only limited to high contrast materials and processes happening over long time scales.

4D tomographic imaging along with some image analysis methods has been used to study combined microstructure and mechanical evolution of different materials [90, 115, 116, 117]. For example, Latil et al. [117] have used 4D imaging to study the micromechanical behaviour of a saturated fibre bundle during an in-situ compression test. This was done by quantifying some microstructural descriptors such as fibre orientation from 3D images at different stages of deformation to characterize evolution of the fibrous medium during its deformation.

4D imaging has also been applied to perform in-situ analysis on paper products. Viguié et al. [118] have used 4D imaging to study hygroexpansion of lignocellulosic fibrous material. They used a paper-board made up of several layers and subjected it to a variation of humidity while performing X-ray microtomography scanning. Then, image correlation techniques were used to measure in-plane and out-of-plane displacement fields which revealed that hygroexpansion is highly anisotropic. They also used the obtained data to characterize the hygroexpansion micromechanisms for the fibre and pore phases. This showed that hygroexpnsion is highly dependant on the fibre content of the fibrous layer.

Digital Volume Correlation DVC is a three-dimensional expansion of the standard two-dimensional Digital Image Correlation (DIC) [119]. DIC is now widely accepted and commonly used in experimental mechanics and is used to obtain direct in-plane displacement measurements and full-flied strains [120]. This is achieved by tracking of points (features) in the digital images of the surface of a test object to match them in the reference state and after deformation. This will result in their displacement vector that can be used later to obtain their corresponding strain fields. While DIC is only limited to 2D images and deformation of the surface of the test objects, DVC is a true 3D measurement technique that uses the same principles as in DIC to calculate internal displacements. DVC is dependant on tracking of naturally occurring textures inside the materials, and therefore, is typically used along with high-resolution tomographic 4D imaging. This dependence limits the application of DVC to materials that possess suitable microstructures. DVC have been applied to study the behaviour of many materials ranging from indentation response in metallic foams [121] to microstructural behaviour of trabecular bone compression [122]. The fibrous structure of paper materials make DVC a suitable tool to study their deformation mechanisms. More technical details about the DVC method are provided in Section 2.4.2.

1.2 Summary

The search for novel paper-based products derived by the competition in pulp and paper industry has become the motivation behind further investigation of different properties of paper materials. Development of novel products necessitates a deeper understanding of process-microstructure-properties relationships in order to better tailor the properties for such products. Consequently, in recent years the mechanical properties of paper, including their tensile strength, has regained attention within the research community. As explained in section 1.1.1, the strength of paper mainly depend on the properties of its constituent fibres and their relative and cumulative arrangement, or in other words, paper's network structure that can be modified through different processing methods. As explained in section 1.1.2, refining, pulp mixture, and drying can significantly alter the mechanical properties of the final paper product.

Refining processes aim to minimize the inter-fibre bond breakage during deformation and failure of paper samples by inducing morphological changes in the constituent fibres. This results in a more efficient paper network during deformation that improves the tensile strength. Moreover, as explained in section 1.1.2.3, since bond formation happens during the drying process, changing the drying conditions can also substantially alter the extent of inter-fibre bonding inside the paper sheets. As shown in sections 1.1.1.3 and 1.1.1.3 , although the effect of inter-fibre bonding on deformation and failure mechanisms, and its resulting translation to macro-scale strength properties is well understood, there is no clear agreement in the paper community on the relative importance of different mechanism (i.e. fibre/bond breakage) during deformation and failure of paper products. This underlines the need for direct observation of deformation and failure of paper materials to gain insight about mechanisms that are active during deformation and failure, and also to quantify their relative importance. This can be achieved by measurement of evolution of microstructural descriptors such as inter-fibre bonding.

In addition to the refining process, the strength properties can also be changed by altering the pulp mixture. This can be used to tailor paper properties by changing the intrinsic properties of the constituent fibres. Another industrial motivation for pulp mixture is to reduce the cost by substitution of some fibres with cheaper ones. In this case, interactions between fibres become even more important. As shown in section 1.1.2.2, there has been many studies focused on understanding the effect of pulp mixture on the properties of the final paper products. Although there are a few mixture models that have been developed for paper products using statistical methods, there is no clear understanding of how the physics of fibre-fibre interactions changes with changing pulp blends. This underlines the need for further investigation. The first step in doing so would be to see if different pulp mixtures with the same amount of refining result in different extents of inter-fibre bonding. Since deformation of paper is mainly governed by the extent of inter-fibre bonding, characterization of deformation and failure of paper by direct observation can shed light on the the level of inter-fibre bonding inside the paper network.

Recent developments in synchrotron X-ray tomography allow for the 4D imaging of a wide range of engineering materials during processing and in-service use. As ex-

plained in Section 1.1.3.3, this method, combined with software tools including fibre segmentation and Digital Volume Correlation, make it possible to quantify deformation at the scale of microstructure. It is now possible to acquire the 3D structure of paper during different stages of deformation, and further to analyze the volume images to directly characterize their deformation.

1.3 Scope and Objectives

Considering the industrial importance of the level of inter-fibre bonding in predicting the behaviour of paper materials, especially for samples made from pulp mixtures, and the scientific importance of understanding the evolution of fibre morphology during paper deformation, and new 4D imaging methods that have become available for materials engineering research, the main objectives of this thesis are:

- To demonstrate the viability of using 4D imaging to observe the evolution of fibre-level and network-level properties of paper during deformation
- To characterize the deformation mechanisms of paper based on microstructural descriptors such as inter-fibre bonding and curl index
- To apply the developed methods to study deformation of a series of handsheets with different levels of bonding to see if deformation of samples can be used to evaluate the level of bonding of their network
- To use the obtained insights to evaluate the level of bonding inside the network of a series of samples made from pulp mixture of varying levels of NBSK and Eucalyptus fibres

This thesis includes six chapters. In Chapter 1, an introduction along with a review of the relevant literature was provided, and the scope and objectives were listed. Chapter 2 provides the details about the 4D imaging experiments, along with the explanation of the image analysis methods that are later used in Chapter 3 and 4. In Chapter 3, these methods are applied on the dataset obtained from 4D imaging experiments to gain general insights on deformation of paper. In Chapter 4, the insights of Chapter 3 are utilized to study the effect of bonding and pulp mixture on

deformation of paper. In Chapter 5, the obtained image volumes are used to measure the Poisson's ratios of all samples. Chapter 6 summarizes the findings of this research and provides recommendations for future work.

Chapter 2

Methods

In this chapter a detailed explanation of the methods used for this study will be provided. In doing so, this chapter is divided into four sections. In the first section, the method used to acquire the 4D data is provided. Second, a detailed explanation about the sample preparation and the design of the sample holder is given. Third, a description of the details of the fibre segmentation methodology are provided. Finally, a detailed explanation of the DVC method is given.

2.1 4D Imaging of Paper

The 4D imaging synchrotron Computed Tomography (sCT) experiments were performed on the I13 beamline at the Diamond Light Source (Didcot, UK) under pink beam conditions. As mentioned in the Section 1.1.3.1, typically monochromatic beams are used in synchrotron facilities in order to avoid beam-hardening artifacts that are present in polychromatic laboratory sources. However, the use of monochromator results in significant loss in X-ray flux [123]. This leads to increased data acquisition times that would be too long to capture in 3D the dynamics of fibre deformation. An alternative to monochromatic X-rays is the so-called pink-beam in which only the high-energy X-rays are filtered greatly increasing the X-ray flux.

Imaging Setup The detectors on I13 beamline were placed on a motorized stage that enabled adjustment of the sample to detector distance up to 2000 mm. The sample to detector distance in this case was set to be around 1 m allowing for some

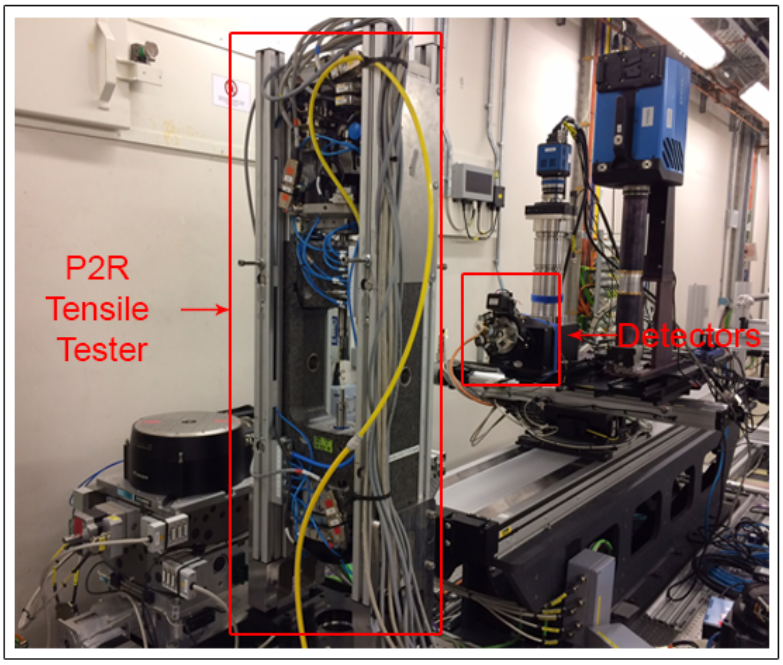

Figure 2.1: P2R tensile tester

phase-contrast to be captured in the images. After interacting with the paper, X-rays are transformed to visible light by a scintillator screen, and then captured by digital detector placed behind an optical microscope. The 4X objective lens was chosen for these experiments, along with a PCO Edge camera, resulting in a voxel size of 1.6 μm and a field of view of 64 mm^3. The pink beam mode was used enabling a fast exposure time of 0.101111 s per projection. In total, 1800 projections were taken for each tomograph resulting in a scan time of around 3 minutes, and in total $\approx$ 18-20 3D image volumes were acquired during the deformation process.

In-situ Tensile Testing A bespoke tensile tester known as the P2R [124] was provided by Manchester University to perform the *in-situ* tensile tests. Figure 2.1 shows the P2R tensile tester placed in the beamline. Tensile tests were performed under a constant rate of deformation of 100 μm/min. Deformations were applied at increments of 100 μm followed by a 2-minutes relaxation time. In total, each sample was deformed in about 18 - 20 steps prior to failure, with 3D images captured at each step. One should note that some samples contained areas of yellow/brown discoloration after the 4D imaging, providing some indication that the intensity of the X-ray beam may have damaged some of the handsheets.

2.2 Sample Preparation and Holder Design

Ten standard handsheets were used in this study: four softwood handsheets to study the effect of bonding on deformation and failure mechanisms, and five handsheets to study the effect of pulp mixture on deformation and failure mechanisms. All handsheets were created using the facilities at the University of British Columbia (UBC)'s Pulp and Paper Centre. The four samples used to study the effect of bonding were made from NBSK pulp and are referred to as freeze-dried, non-refined, moderately-refined, and highly-refined. The six samples used to study the effect of pulp mixture were made using different levels of separately refined NBSK pulp in combination with Eucalyptus pulp, and are referred to based on their NBSK content. All the pulp used for sample preparation was provided by Canfor. While the freeze-dried and non-refined samples had no refining, the moderately-refined and mixture samples were Low-Consistency (LC) refined at 60 kWh/t, and the highly-refined sample were refined at 100 kWh/t. Except the freeze-dried sample, which as implied by its name was freeze-dried into a handsheet, all the samples were air-dried. Air drying was performed in restraint at 23 °C and relative humidity of 50% for 24 hours after formation of the sheets. The handsheets, having an areal density of 60 g/m^2, were formed using a British handsheet maker and following standard TAPPI procedures. Table 2.1 lists all the handsheets and their respective processing parameters.

The handsheets were cut into samples having a dog-bone shape as shown in Figure 2.2 (a). Samples were 18 mm long with a gauge length (width) of 2.8 (3.0) mm. The doge-bone shape of the samples was employed to ensure that the fracture would occur in the field of view during sCT imaging. The handsheets, except the freeze-dried samples, were all cut by Silver Bullet^{TM} single-blade paper cutter at UBC. The freeze-dried samples, due to their delicacy, were cut using a laser cutter at University College London.

To increase the load to a measurable level of ≈20 N for the bespoke tensile tester of the synchrotron facility a multi-sample test setup was developed, and shown in Figure 2.2 (c). Consequently, four samples (three for the freeze-dried sample) were deformed concurrently. As can be seen in Figure 2.2 (c), 3D printed rectangular spacers were fixed on each side of each sample in the multi-sample test setup, using

Sample Name	Material	Refining Energy (kWh/t)	Drying
Freeze-dried	100% NBSK	0	freeze-dried
Non-refined	100% NBSK	0	air-dried
Moderately-refined	100% NBSK	60	air-dried
Highly-refined	100% NBSK	100	air-dried
100% NBSK	100% NBSK 0% Euc.	60	air-dried
80% NBSK	80% NBSK 20% Euc.	60	air-dried
40% NBSK	40% NBSK 60% Euc.	60	air-dried
20% NBSK	20% NBSK 80% Euc.	60	air-dried
10% NBSK	10% NBSK 90% Euc.	60	air-dried
100% Euc.	0% NBSK 100% Euc.	60	air-dried

Table 2.1: List of samples with their processing conditions

double-sided adhesive. The spacers were needed to separate the samples so that they would be easily distinguishable in the acquired 3D images. The adhesive layers were used as reinforcement to ensure that the fracture would not occur in the grip area, and also to facilitate load transfer between spacers and samples. A pin-grip design was employed to link the samples together, as well as to the tensile tester. Further, an assembly mould as shown in Figure 2.2 (b) was used to ensure that all the samples are aligned together. To do so, samples and spacers were laid on top of each other inside the mould and then a pressure was applied to make them stick together.

The multi-sample geometry was mounted inside the tensile tester using purpose-built grips, additively manufactured, and depicted in Figure 2.3 (a). A screw-nut setup was used to apply adjustable compressive load to further ensures that the fracture would not occur in the grip region. The U-shape bracket was used to facilitate sample handling without damaging the samples; this was taken out after the grips were placed in the tensile tester. Figure 2.3 (b) shows the actual 3D printed grips along with their multi-sample setup. Figure 2.3 (c) shows how the grips were placed inside the tensile tester.

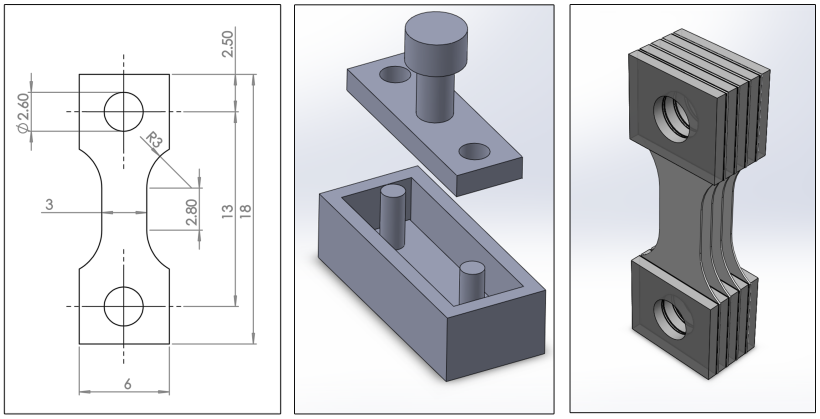

Figure 2.2: Schematic drawing of (a) sample geometry (b) assembly mould (c) multi-sample geometry

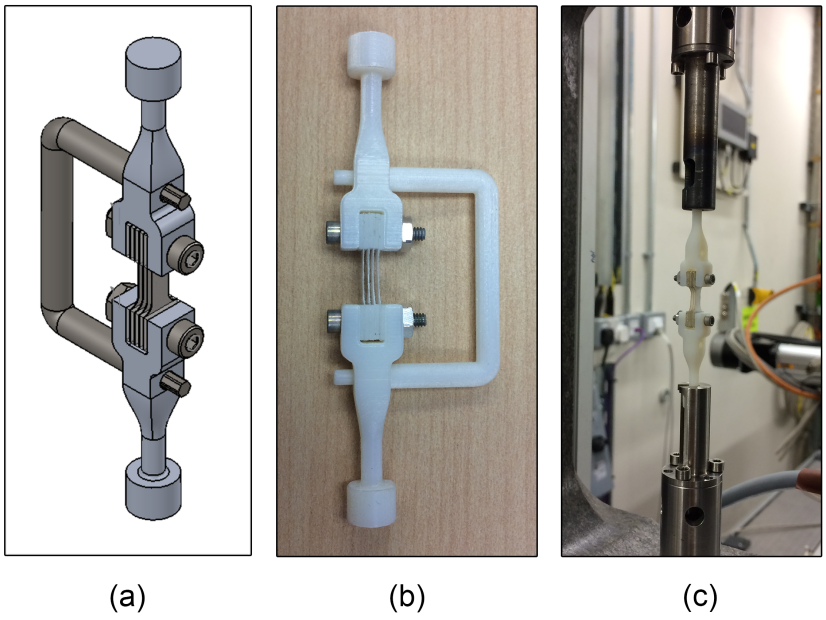

Figure 2.3: (a) Schematic drawing of the grip, (b) Actual 3D printed grip and its multi-sample setup, (c) samples placed inside the tensile tester

2.3 Segmentation

The segmentation method developed in this work is an improved version of the automated fibre segmentation method developed by Sharma et al. [100]. Since this method uses binarized 3D images as input, the acquired sCT images need to be bina-

rized before segmentation. Further, to improve the quality of the binarization step, a denoising step was also necessary to remove artifacts and noises from the obtained sCT images. Therefore, denoising and binarization steps, which are different to the methods used in [100], will be explained first before moving to a detailed explanation of the developed segmentation algorithm.

2.3.1 Denoising

In general, images that are acquired from X-ray tomography can include noises and artifacts that necessitates a filtering step to remove such noises. This becomes challenging when the contrast of images are low, which is the case with X-ray tomographic imaging of paper samples. Figure 2.4 (a) shows a cross-sectional slice of a volume image of a paper sample acquired by sCT. As can be seen, fibres appear as light ring shaped objects and the grey areas surrounding them are in fact the air inside and outside of the fibres. Ring artifacts and a noisy background can also be seen; these result in large errors during the binarization step. Since the segmentation method is based on identification of fibre lumens, general smoothing filters that perform indiscriminate blurring cannot be used to remove the noise as they can result in blurring of the fibre edges making such identifications even more difficult. Considering the importance of fibre edges, edge-preserving filters seem to be the best option for denoising.

The denoising filter used in this work was a bi-exponential edge-preserving smoother called BEEPS [125]. BEEPS is structurally similar to a bilateral filter and uses a simple local adaptation of the filter weights to preserve edges with low computational costs. Due to the size of sCT image data, low computational cost is a desirable attribute. Similar to bilateral filters, BEEPS also contains two essential ingredients of a range filter r and a spatial filter s. While r is used to measure the degree of photometric similarity of a neighbourhood (i.e. image intensity), s determines the spatial extent of the filter. There are two choices for the range filter: Gaussian-like or sech-like (i.e. hyperbolic secant). In both cases, the contribution of the range filter is controlled by its standard deviation. While a large standard deviation leads to a broad range filter that has a weak effect and allows for the smoothing of all but the strongest edges, a small standard deviation results in a narrow range filter with strong effect that forbids the smoothing of most edges. Decay of a bi-exponential filter con-

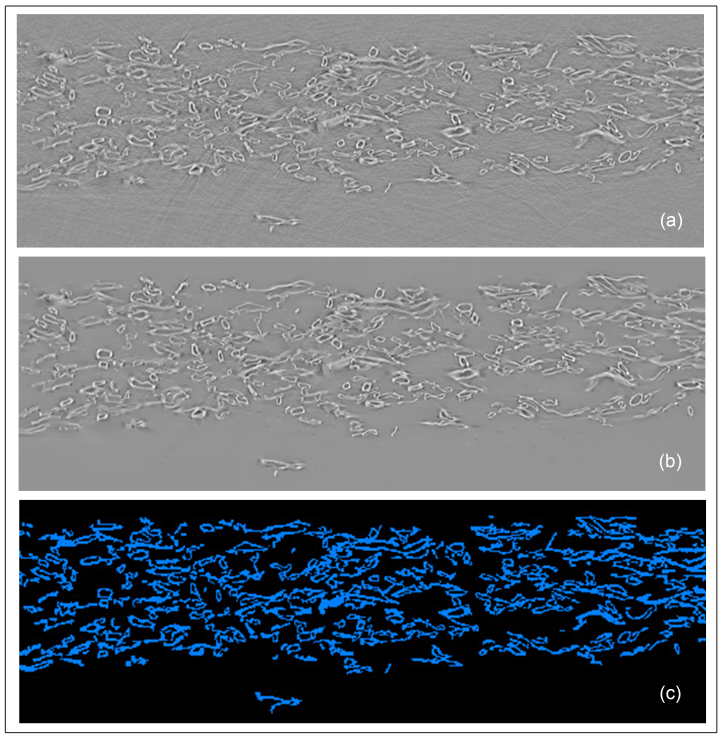

Figure 2.4: Cross-sectional slice of a sCT image of a paper sample (a) in as-scanned condition (b) in filtered mode (c) in binarized mode

trols the amount of spatial smoothing with useful decays being in the interval [0, 1). With slow decay (near 0), the filter has a long-range reach and the spatial smoothing is strong.

In this study, BEEPS is used as a plugin within the ImageJ [126] software. Figure 2.4 (b) shows the same slice as in Figure 2.4 (a) after application of a BEEPS filter using the following parameters: a sech range filter with standard deviation of 6.00, a spatial decay of 0.01, and 6 iterations. Figure 2.5 shows the histogram of the same slices before and after application of BEEPS. The effectiveness of filtering is evident from the slimmer tails and a higher peak in the histogram of the filtered image.

2.3.2 Binarization

Although Sharma et al. [100] have developed a binarization method based on the basis weight of paper samples, this study utilized a hysteresis thresholding method instead of a standard thresholding method [127]. Avizo® software is used in this research to perform the hysteresis thresholding. While in a standard thresholding

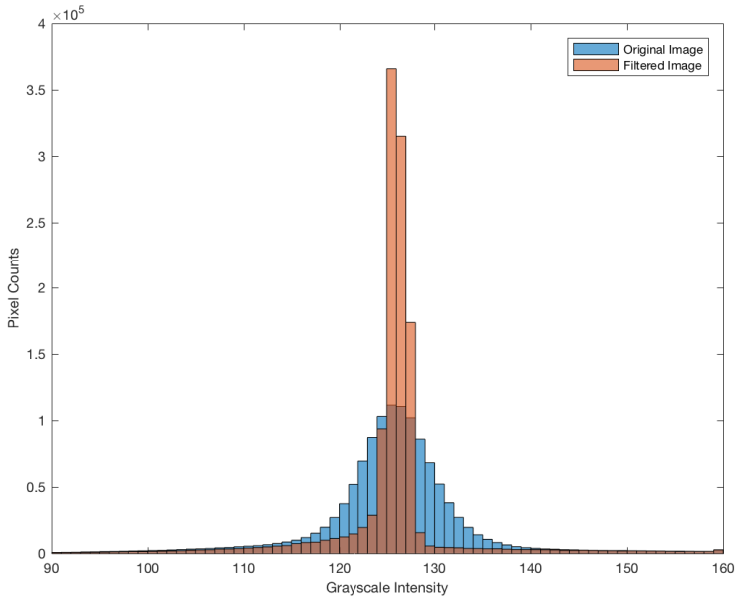

Figure 2.5: Histogram of cross-sectional slices of a sCT image of a paper sample before and after denoising using BEEPS

method any pixels lower than the threshold is turned into black and any values above it to white, the hysteresis mode uses a hysteresis loop to provide a more connected thresholding result. First, two threshold parameters λ_1 and λ_2 (i.e. grayscale values) are specified. Then, if intensity of the point $I(n, m) > \lambda_2$ then the point is in the retained area and it is turned to white. If $I(n, m) < \lambda_1$, the point is in the rejected area and it is turned to black. However, if $\lambda_1 < I(n, m) < \lambda_2$, the point is in the fuzzy area, where it will be retained if it has any connectivity to a retained area, or otherwise will be rejected and turned to black. This method has the potential to be run in 3D where the connectivity criteria is measured in 3D. The low and high range of grayscale values are obtained by addition and subtraction of a constant value (e.g. 5) to the threshold value obtained from the method in [100]. This approach will result in lower white speckles in the binarized images while using lower values for threshold that helps preserve closed lumens, which in turn can facilitate lumen tracking. Figure 2.4 (c) shows the result of hysteresis thresholding, using the Avizo® software, on the cross-section image shown in Figure 2.4 (b). As can be seen, a nicely-binarized image is obtained. Having denoised and binarized the data, volume images are now ready to be fed into the segmentation algorithm.

2.3.3 Existing Segmentation Method

The segmentation method developed by Sharma et al. [100] consists of the following three stages: lumen tracking, fibre walls extraction, and second-level segmentation.

In the lumen tracking stage, a modified connected component labelling algorithm is used to track the lumens throughout the 3D volume. Although the geometry of lumens are not closed in 3D due to the presence of pores in the fibre walls and the fact that fibres have open ends, the cross section of lumens in 2D cross-sectional slices of the volume image have a closed geometry. Therefore, with the exception of cracked lumens, a simple connected component labelling algorithm [128] is capable of identifying and separating most of the lumens in the cross-sectional images of the dataset. Considering the fact that lumens of the same fibers will have some overlapping points in the adjacent slices, identified lumens can be merged to create a 3D lumen. When a lumen is cracked or a fibre end is reached in a slice, connected component labelling will result in part of the background to be labelled as the lumen in that slice. Therefore, a sudden increase in the lumen cross-section area can be used as a method for identification of pores and fibre ends. If the cross-sectional area of a lumen, after sudden increase in slice k, returns to its original size within an acceptable threshold after n slices, then the lumen is identified to have a pore. The intersection of the lumen in slice $k+n$ with the background in the slices k to $k+n-1$ are taken as the lumen for those n slices. However, if the sudden increase in the lumen size does not recover after n slices the fibre is considered to be ended at the slice $k-1$. Thus, this method is capable of successfully identifying the lumens that have pores in their fibre walls.

In the fibre wall extraction stage, the 3D lumens identified by the lumen tracking stage are used as seed data to extract fibre walls by assigning each voxel in the fibre phase the label of the closest lumen. First, a distance transform is performed on the 2D slices of the segmented fibres. This results in the voxels belonging to the lumens to have a value of zero and the remaining voxels to have values based on their distance from nearest lumens. Multiplication of the obtained dataset by the binarized data will result in each voxel in the fibre phase to have a value based on their distance to the nearest lumen. Application of a threshold value on the distance transformed data

will result in removal of the voxels that are farther than the threshold value from each lumen preserving the topology and thickness of fibres. Finally, assigning the label of their nearest lumen to each voxel in the fibre wall phase will result in identification of the boundaries of fibres that are in contact leading to effective segmentation of the fibres.

In the second-level segmentation, the focus is on tracking the collapsed regions of fibres. Since there are no lumens in such regions, the lumen tracking is not capable of identifying such regions, and therefore, crushed fibres appear as several smaller fibres in the segmented data. To overcome this issue, in the second-level segmentation the non-segmented fibre voxels are attached to either ends of the segmented fibres based on their connectivity to the fibre voxels in adjacent 2D slices. In this way each segmented fibre may grow at its ends and overlap with other segmented fibres. Such overlap can be used as an indication that those segmented fibres belong to a single fibre. This can be used to merge such fibres segments into a single fibre leading to effective segmentation of fibres that have collapsed regions in their fibre walls.

2.3.4 3D Lumen Tracking

The method developed by Sharma et al. [100] is based on the assumption that fibres in a paper sample are all more or less aligned in a single direction and lumens can easily be detected from their cross sections in 2D slices perpendicular to the direction of fibres. However, in handsheet samples, where fibres are randomly oriented, such assumptions do not hold resulting in this method to be biased to a single direction. To overcome this issue, the developed code has been extended to a 3D lumen tracking algorithm by extending it to each of the three x, y, z axes. This will result in the need to merge three different set of labels each obtained from each of the three directions. The details of the developed algorithm, based on connectivity criteria of fibre lumens, is provided in the following section.

The lumen identification step in [100], where a series of constraints are used to remove the false positives may result in some directional bias. Such constraints include limiting the maximum and minimum values for areas of blobs that are identified as lumens and selection of a threshold value for the solidity of such blobs. The solidity of a blob of pixels in image processing is defined as the ratio of its area to its convex

area, which is in fact the area of its convex hull. Therefore, shapes similar to a circle have higher values of solidity compared to shapes similar to a star. Because of these constraints, blobs that are identified as lumens but are in fact areas between fibres, due to their shape, will have lower values of solidity. By choosing an appropriate threshold value for solidity, all the blobs that result from areas between fibres can be removed. However, when fibres are not all perpendicular to the 2D cross-sectional slice that is used for lumen identification their lumesn can appear in different sizes and shapes, and therefore, application of such global threshold values might limit the effectiveness of this method. Considering that same lumens can also appear in different shapes and sizes in 2D slices from different directions, and the fact that lumens with pores in a 2D slice in one direction can have a closed lumen in another direction, a multi-directional identification of the same lumen can facilitate a more effective lumen tracking approach and remove the directional bias of the existing method.

In the 3D lumen tracking method, the lumen identification method developed in [100] is used in three orthogonal directions. Figure 2.6 shows identified lumens in an X-ray tomographic image of a paper sample obtained from a lab equipment. Figure 2.6 (a) shows the identified lumens from only one direction, while Figure 2.6 (b) shows the identified lumens from three orthogonal directions using the same method. The same parameters of solidity and area of lumens were used in both cases. In Figure 2.6 (b) different colors indicate voxels that are identified from different directions. One should note that some lumens were identified from all three directions and some of them were only identified from one direction resulting of 48% increase in the number of voxels identified as lumens for this sample. This is more evident in Figure 2.7 that shows a 2D cross-sectional slice of the identified lumens. As can be seen from Figure 2.7 (b), different parts of the same lumen can be identified from different directions that results in them having different labels depending on the identification direction. This necessitates a method to merge different parts of the same lumen together.

A connectivity criteria is used in this method to merge different segments of the same lumen that are identified from different directions, and consequently, have different labels. This connectivity criteria is based on the fact that lumens of different fibres are separated by their fibre walls and do not touch each other. Consequently, a

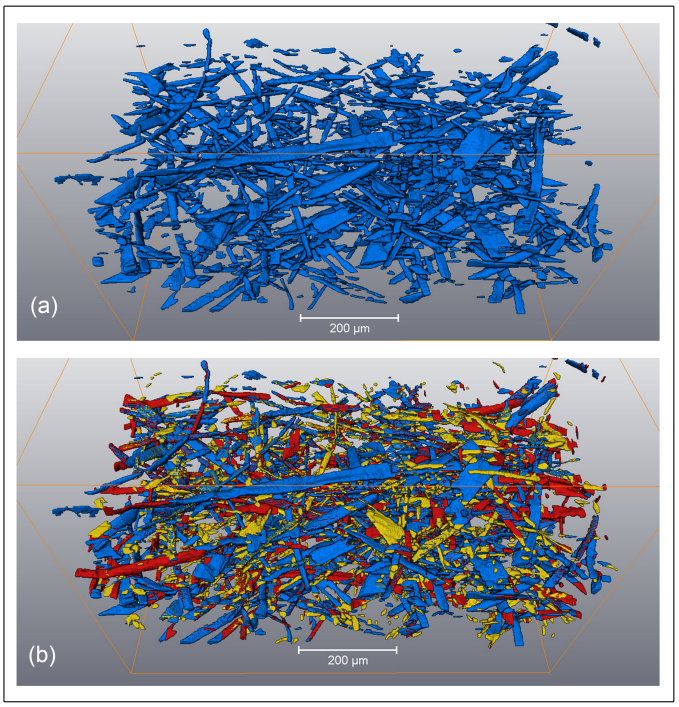

Figure 2.6: 3D visualization of (a) lumens identified from a single direction (b) lumens identified from three orthogonal directions. Voxels are colour coded based on the direction of identification

simple connected component labelling can result in proper labelling of lumens leading to merging of different segments of the same lumen. This is evident from Figure 2.7 (c) where the identified lumens from different directions are labelled based on their connectivity. Figure 2.8 shows the extracted fibre walls using the same labelled lumens as in Figure 2.7 (c). As can be seen, 3D connectivity of the segmented voxels can successfully be used to label the lumens of a fibre that are identified from different directions. As evident however, there still remains some lumens with different segments that are not merged together. This is due to the fact that those segments were separated by collapsed regions of that fibre, and therefore, there were no lumens in that regions to be identified and used for connectivity. This can be overcome using the second level segmentation method described in [100].

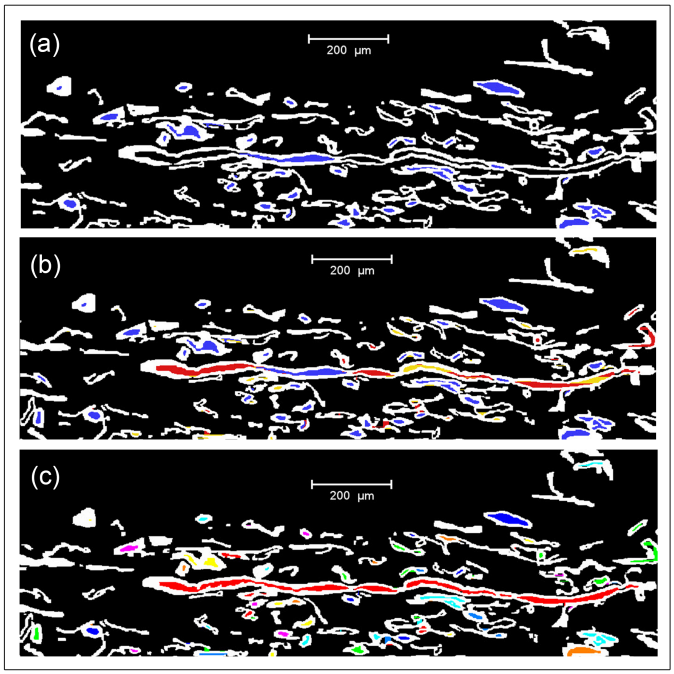

Figure 2.7: 2D cross-sectional slice of lumens (a) identified from a single direction (b) identified from from three orthogonal directions and colour-coded based on their direction of identification (c) labelled using their 3D connectivity.

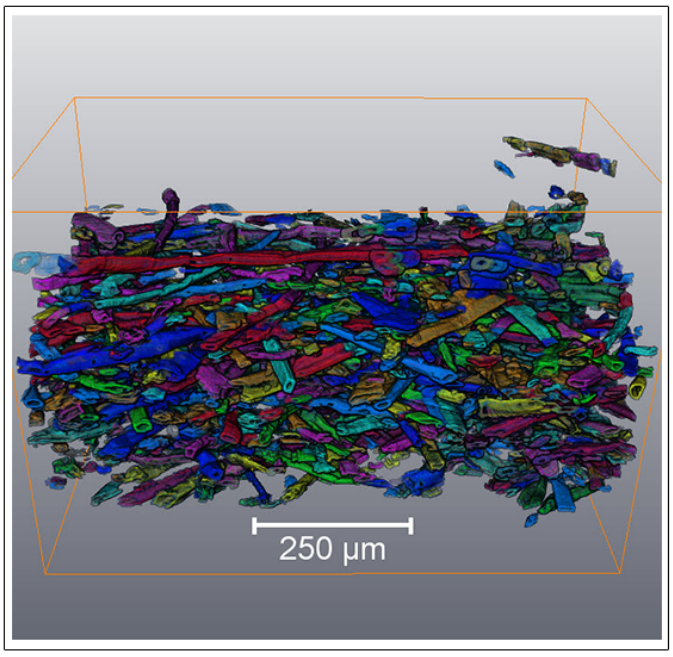

Figure 2.8: 3D visualization of extracted fibre walls using lumens labelled by their 3D connectivity.

2.3.5 Post-processing

Having segmented individual fibres inside the volume image of a paper sample, different network and fibre level properties can also be calculated using those segmented fibres. Considering the scope and objectives of this thesis, two properties of Relative Contact Area (RCA) and curl index are of interest. RCA is a property similar to the Relative Bonded Area but applicable to sCT datasets as described below. Calculation of RCA in different stages of deformation using the 4D imaging data at hand can help in quantitative studies of the evolution of inter-fibre bonding during deformation and failure of paper samples. Further, curl index, as explained in the literature review section, is the measure of straightness of fibres, and therefore, such measurements can make it possible to study straightening of fibres that is thought to be one of the major underlying mechanisms of paper's auxetic behaviour.

2.3.5.1 Relative Contact Area

As explained in Section 1.1.1.2, relative bonded area can be measured directly using image analysis methods by finding the contacts of segmented fibres. In this case, calculation of relative bonded area reduces to counting the number of voxel faces that are in contact with each other and belong to different fibres, divided by the number of voxel faces that are in contact with the air, multiplied by the surface area of each voxel (i.e. resolution squared). However, this method necessitates the need to segment all the individual fibres inside a paper handsheet, which with current state of the available tools is virtually impossible. Nevertheless, since the purpose of this measurement is to study the evolution of this descriptor during deformation of paper networks, a similar approach as proposed by Sharma et al. [100] can be adopted. In this case, instead of measurement of relative bonded area for the whole paper handsheet, this measurement is obtained for each segmented fibre that is written back to the non-segmented volume. Then, counting the number of voxel faces of the segmented fibre that are in contact with the rest of the fibres will result in the contact area for each fibre. Furthermore, the tracked lumens for each fibre can also be added to the original volume to exclude the voxels inside the fibre from this measurement. Figure 2.9 (a), shows a cross sectional view of the segmented fibres inside the freeze-

dried sample that are longer than 0.5 mm using the developed algorithm of this study. As can be seen, the identified contact areas of the fibres with the air and the rest of the fibres are indicated by the developed algorithm using red and green regions, respectively. Figure 2.9 (b) shows a 3D visualization of one of these segmented fibres chosen arbitrarily where the red areas indicate the fibre areas in contact with air and the green regions indicate the contact areas of the fibre and the rest of the volume. Division of the area of the green regions by the area of the red regions will result in a measurement of relative bonded area for each fibre. However, one should note that this method of relative bonded area measurement is based on the assumption that the fibres in contact form bonds in all the contacted areas, which may not be entirely correct. Therefore, it is more accurate to denote this measurement as Relative Contact Area (RCA) of fibres. In addition, one should note that since the contact area of fibres in digitized volumes also depend on the resolution of tomography data, this measurement might not represent the true contact areas of fibres. Regardless, this value can still be used for a comparative analysis by considering the same segmented fibres at different stages of deformation.

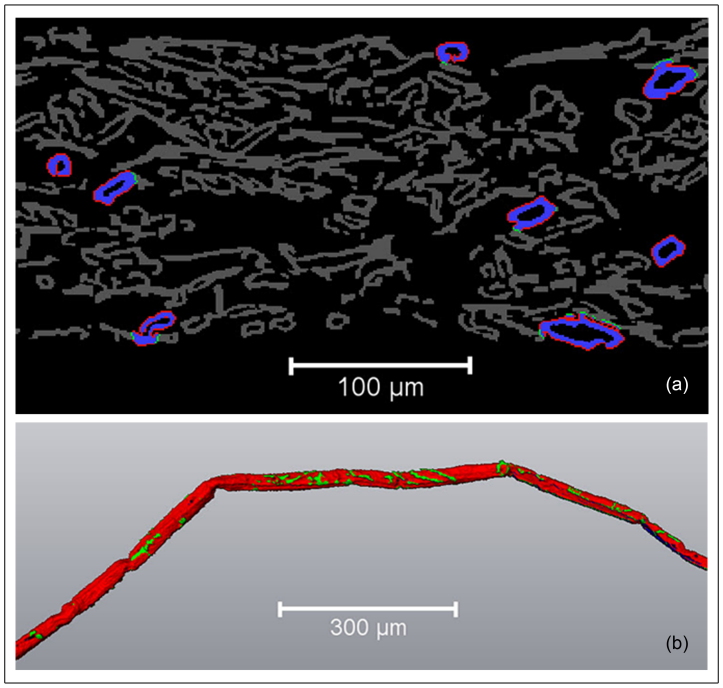

Figure 2.9: (a) Cross sectional view of the segmented fibres that are longer than 0.5 mm and (b) 3D visualization of a single segmented fibre. Red regions depict the free surface area of the fibres and the green regions indicate the fibre contact areas.

2.3.5.2 Curl Index

As explained in Section 1.1.2.1, curl index is defined as the relationship between the "contour length", and the "projected length" of the fibres expressed in the Equation 1.6. Contour length of fibres are calculated based on the method suggested by Sharma et al. [100]. In this method, the contour length of a fibre is calculated by adding the cord lengths of the digitized fibres. Cord lengths are defined as the Euclidean length between the centres of the fibre's cross section in every two consecutive adjacent slices inside the tomography data. The centre of each cross section of fibres are found by treating the voxels of lumens and fibre walls together as a single cluster of 2D points in each cross section, and using the *k-means clustering* algorithm to find the centroid of that cluster. k-means clustering [129] is a quantization algorithm that aims to partition the given data to different clusters such that the variances of each cluster (within-cluster sum of squares) becomes minimum. Application of k-means clustering to obtain a single cluster made of voxels of lumens and fibre walls will yield the coordinates of the centre of each cross section of fibres. These coordinates can later be used to find the contour length by adding the Euclidean distance between adjacent centres. Furthermore, projected length of a fibre in this case can be found by calculation of Euclidean distance between the centres of the start and end cross section of each fibre. Figure 2.10 (a) shows 81 fibres that are segmented from the freeze-dried sample using the segmentation method of this study and have a contour length of more than 0.5 mm. As can be seen, the obtained centre lines for each fibre are also depicted as red lines. Figure 2.10 (b) shows a 3D visualization of the same segmented fibre as in Figure Figure 2.9 (b). The projected length of this fibre is calculated by Avizo® as 1516.14 μm. The projected length of the same fibre is calculated as 1516.6 μm using the algorithm developed in this study. This value along with the contour length obtained from the method developed by Sharma et al. [100] can be used in Equation 1.6 to find the curl index of each segmented fibre.

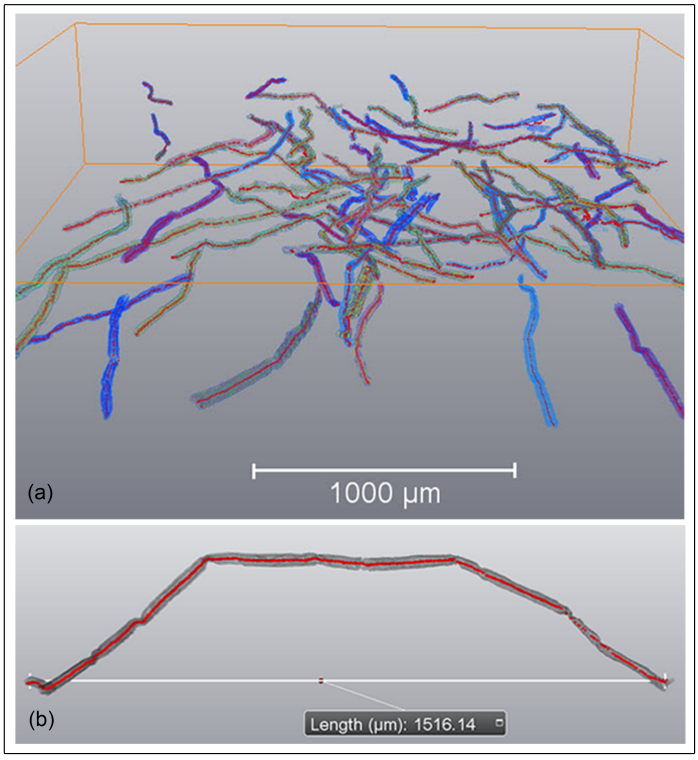

Figure 2.10: (a) Segmented fibres of the freeze-dried sample that are longer than 0.5 mm along with their centre lines plotted in red, and (b) single segmented fibre along with its centre line and projected length

2.4 Digital Volume Correlation

Since its introduction in 1999 [130], DVC has seen a rise in its variation of implementations that try to achieve higher efficiency and accuracy [119, 131]. A commercial software named VicVolume® is used in this research for DVC analysis, and consequently, details of the underlying calculations are not available. However, all the spatial-domain DVC are based on the same general procedure [121]. The procedure of DVC analysis of this research can be divided into two steps of 4D volumetric image acquisition and calculation of the strain fields that are explained in detail in the following sections.

2.4.1 4D Volumetric Image Acquisition

The first step for any DVC analysis is to acquire a set of volumetric images of a test subject at different levels of deformation. As explained in Section 2.1, 4D synchrotron

X-ray tomographic imaging is used in this research to obtain suitable data for DVC analysis. One should note that such volumetric data are in fact a discreet set of data points that represent the interaction of the test subject with the imaging ray over a small volume called voxel [121]. As a voxel value is associated with a discreet point in the centre of the voxel, the intensity values between centres of different voxels need to be interpolated. This interpolated data are normally used when a 3D visualization of the data is rendered. Having obtained the necessary data, the process of DVC starts by defining the region of interest. A set of discreet points are then defined inside this region based on the accuracy requirements.

It should be noted that the considered deformed volumes in this research are all *registered* with the reference volume. Registration is a process similar to DVC where only the translation of the deformed volume is considered. During registration the volume is translated to a point that maximizes the correlation between the deformed and the reference volumes. In this way the result of DVC analysis will only include the deformation of the sample and the translation will be excluded from the analysis. Avizo® is used in this research for all the registrations.

Figure 2.11 shows the freeze-dried sample as is displayed inside the editor of VicVolume®. As can be seen from Figure 2.11 (a), the region of interest is first drawn manually by the user by specifying a set of points as the boundaries. The yellow indicator inside the region of interest is an initial guess defined by the user. Initial guesses are used to reduce the computational cost and increase the accuracy of the results. Figure 2.12 shows the editor of VicVolume® that can be used to specify initial guess points. Those points are specified manually by the user mainly considering the translational degrees of freedom (i.e. translation in x, y, and z), and is then checked by the software to examine the degree of correlation between the chosen points considering the extra degrees of freedom: rotation, normal and shear strain. If the correlation coefficient is higher than the threshold value, then the specified point is taken as an initial guess for deformation. As can be seen from Figure 2.11 (b), VicVolume® divides the region of interest into cubic sub-volumes of equal sizes, the size of which is defined by the user based on the underlying microstructural texture of the material. In fact, to obtain reliable results each sub-volume needs to be large enough to include enough information (i.e. texture). The centre point of each

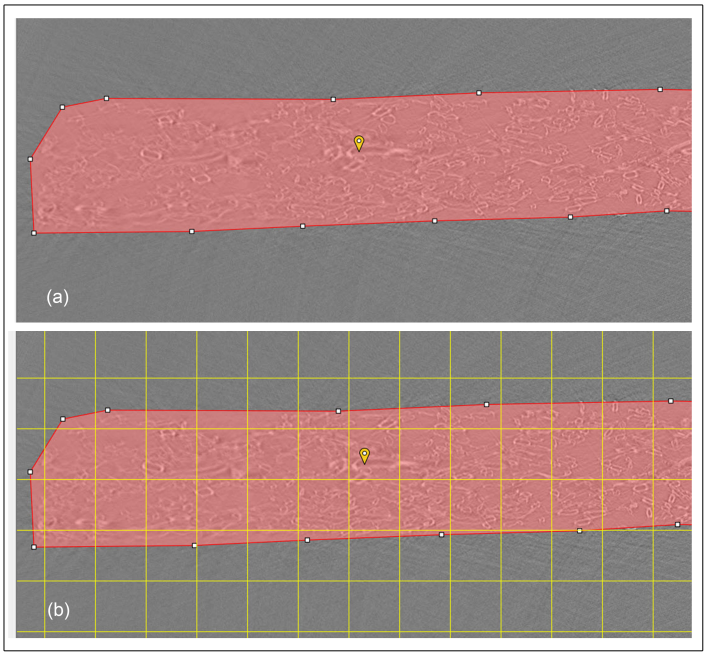

Figure 2.11: (a) Specification of the region of interest and an initial guess (yellow indicator) inside the editor window of VicVolume® (b) division of the region of interest into sub-volumes of equal sizes

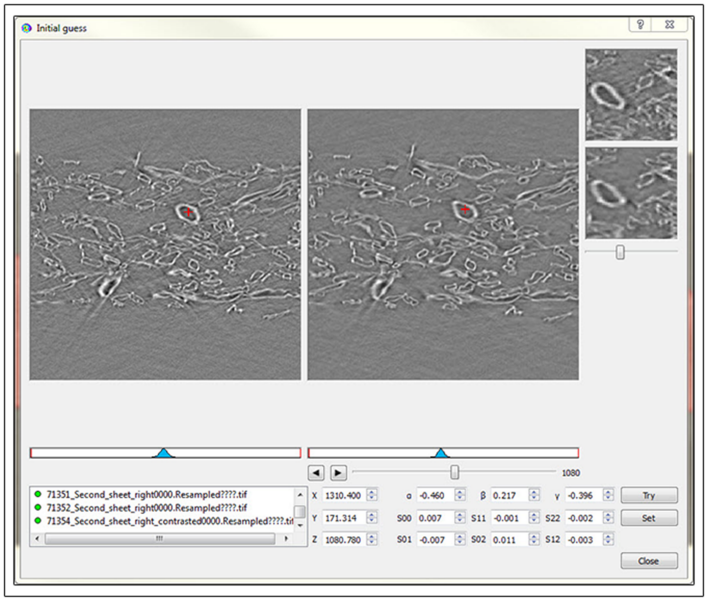

Figure 2.12: Editor window of VicVolume® to specify an initial guess

sub-volume is then taken as the measurement point for estimation of displacement vectors that is explained in more details in the following section.

2.4.2 Calculation of Strain Fields

To calculate the strain fields, first an estimation of displacement vectors are required. Displacement vectors at predefined measurement points are estimated via correlation of the target volume (i.e. deformed) and the reference volume. Figure 2.13 (bottom) shows a schematic summary of the process for a single measurement point p. As can be seen, a sub-volume denoted as k_0 centred at the measurement point p is extracted from the reference volume. The sub-volume is defined as a set of w vectors centred at p and pointing to the centre of each voxel inside the sub-volume, $\{m^\alpha : \alpha = 1, 2, 3, ..., w\}$, with values extracted from the reference volume. Then, the correlation process can be carried out in a general way by performing a series of affine transformations [132] on the original sub-volume k_0 resulting in a series of trial sub-volumes labelled as k. Trial sub-volumes are also defined as a set of w vectors, $\{n^\alpha : \alpha = 1, 2, 3, ..., w\}$ with voxel values extracted from the target volume. The main transformation of interest is translation defined by the vector t, as seen in Figure 2.13 (top). Other transformations, such as rotation, normal strain, and shear strain is also considered to improve the accuracy of the analysis. Next, an objective function is needed to quantify the degree of match between a reference and trial sub-volumes. In this research, Normalized Cross Correlation Coefficient (NCCC) is chosen in VicVolume® for that purpose which is defined as [121]

$$C(g) = 1 - \frac{\sum_{\alpha=1}^{w} B(p + x^\alpha)A(p + m^\alpha)}{\sqrt{\sum_{\alpha=1}^{w} B(p + x^\alpha)^2 \sum_{\alpha=1}^{w} A(p + m^\alpha)^2}} \tag{2.1}$$

where A and B are the reference and the target image volumes,respectively. p is the measurement point and m^α is defined as before. $x^\alpha = t + n^\alpha$ where t is the translation vector and n^α is the trial sub-volume defined as before. Parameter g includes all the active degrees of freedom that include the translation t and the rotation, normal strain, and shear strain parameters that define the transformations performed to obtain the trial sub-volumes. Numerical methods can then be used to obtain the global minimum of the objective function C with respect to the parameter vector g.

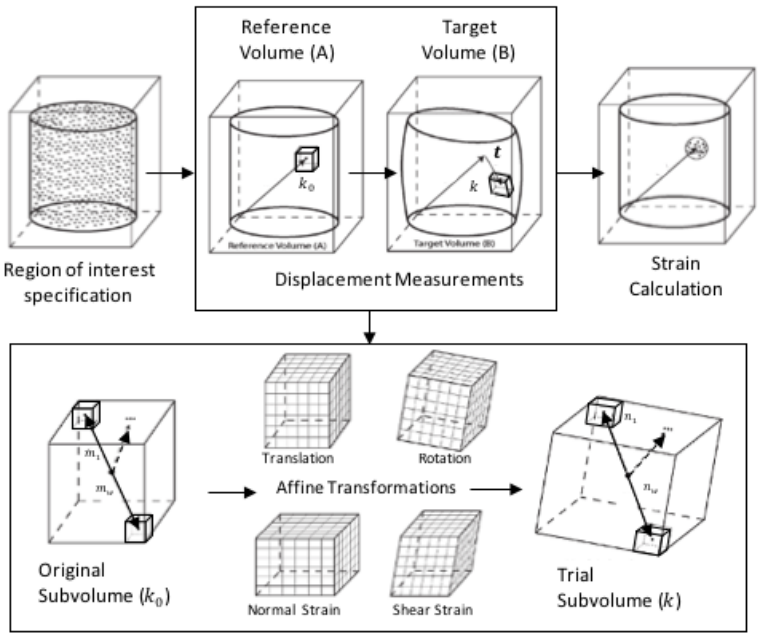

Figure 2.13: Schematic diagram of the general process for (top) DVC analysis, and (bottom) estimation of displacement vectors adapted from [121].

The results, displacement vectors, usually do not point towards the centre of voxels in the target volume, and therefore, interpolation is necessary to achieve sub-voxel accuracy. VicVolume® provides the user with the option to specify the order of the interpolation method (i.e. 4-tap and 8-tap) to modify the computational cost.

Finally, strain fields are estimated from the obtained displacement vector fields. First, the displacement field may be smoothed using a local polynomial fit, and then, is used to calculate deformation gradient tensor from a cloud of neighbouring points by least-square fit to a second-order Taylor series expansion of the displacement vector field [133]. Three threshold values can be specified in VicVolume® to discard the data points with unreliable (i.e. physically unrealistic) displacement values: Consistency Threshold, Confidence Margin, and Matchability Threshold. Consistency Threshold is used to control the maximum amount of change in displacement values of neighbouring points. A value of 0.1 pixel is used to remove the points that their displacement values are larger when compared to their neighbouring points. In addition, Confidence Margin is used to exclude any points that have low correlation values. A value of more than 95% match is used in all the analysis to remove the data points that their estimated locations are less certain. Matchability Threshold is

used to discard any data points that do not contain enough image contrast for proper correlation. A value of 0.1 pixel is used in all the analysis to exclude any sub-volumes that have less image contrast. VicVolume® also requires the user to specify the step size which determines the number of slices that are used in DVC calculations.

2.5 Overview of the Methods

The methods used in this research to characterize the deformation of paper samples can be summarized by the flow chart shown in Figure 2.14. First a 4D volumetric data is obtained by synchrotron X-ray tomographic imaging and in-situ tensile testing of the paper samples as explained in Section 2.1. Then, as explained in Section 2.4.1, Avizo® is used to register the obtained deformed volumes with respect to the reference volume. As explained in Sections 2.3.1 and 2.3.2, the registered data is then filtered and binarized using Avizo®. The filtered and binarized data is then used in the 3D lumen tracking algorithm to segment individual fibres inside both the deformed and reference volumes as explained in Section 2.3.4. Segmentation results, as explained in Section 2.3.4, can be refined by choosing proper constraints on the shape of the lumens until satisfactory results are obtained. Then, curl index and RCA of the segmented fibres are calculated using the methods explained in Sections 2.3.5.2 and 2.3.5.1, respectively. The registered data are also used in VicVolume® for DVC analysis. As explained in Section 2.4.1 the region of interest and some initial guess points are identified by the user. VicVolume®, as explained in Section 2.4.2, requires the user to specify the size of the sub-volumes, step size, interpolation method, and proper thresholding values. These values can be used to refine the results of the DVC analysis. The strain fields obtained from VicVolume® and measurements of curl index and RCA are then used to study the deformation of paper samples.

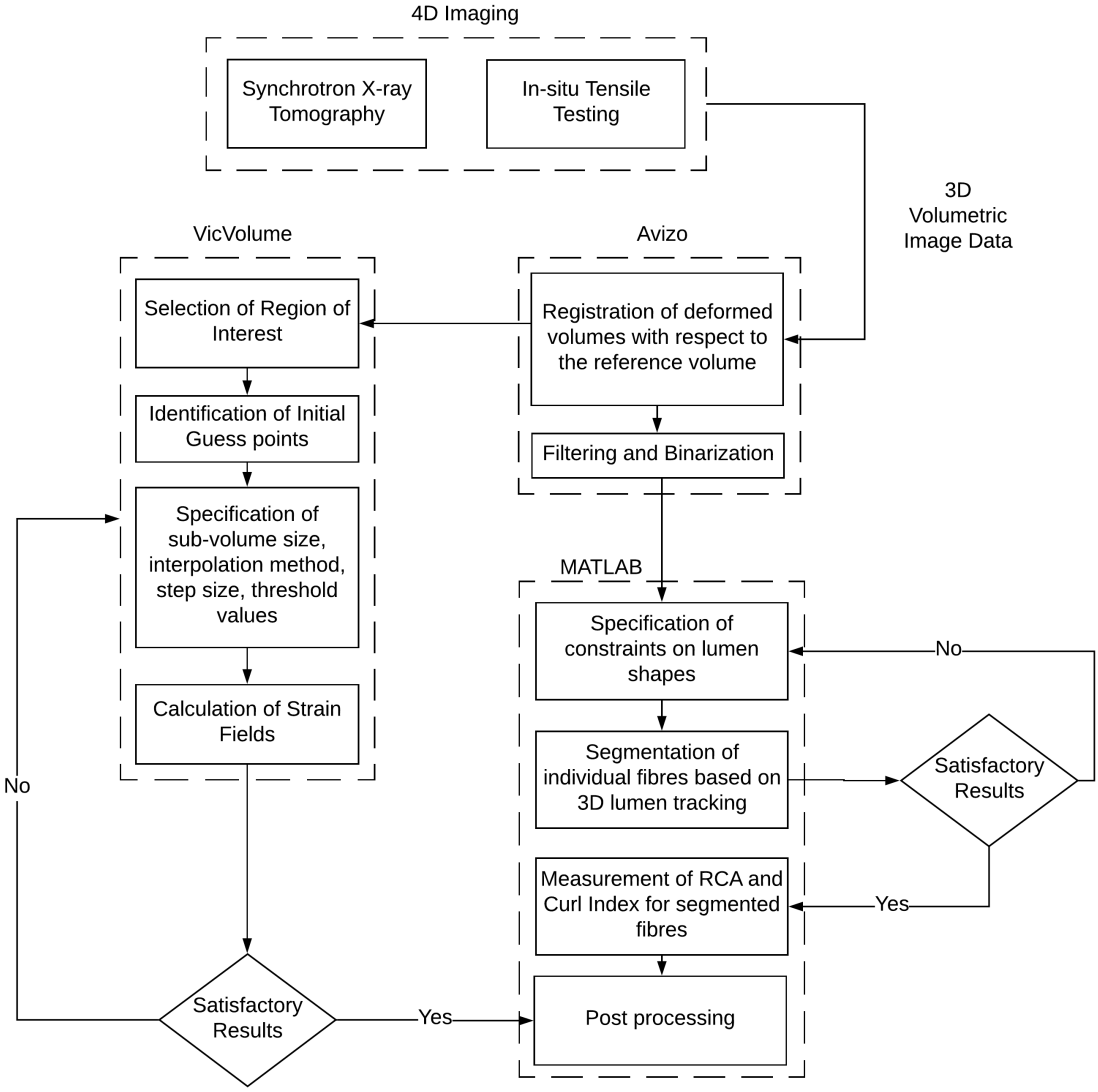

Figure 2.14: Overview of the methods used in this research

Chapter 3

Characterization of Deformation Mechanisms

This chapter is intended to present new insight on paper deformation mechanisms based on analysis of the 4D datasets of paper. In doing so, this chapter is divided into two main sections of network-level and fibre-level analysis. The freeze-dried sample was chosen since it contains a large number of un-collapsed fibres with open lumens, making it perfect for fibre segmentation using the improved segmentation algorithm developed in this thesis. The segmented fibres are later used for both qualitative and quantitative study of deformation at the fibre-level. A summary of the results and discussions is also provided in the final section of this chapter.

3.1 Network-level Analysis

The focus of this section is to study the deformation of the freeze-dried sample at the network level. First, the 3D volume images obtained from the 4D imaging experiment are presented and discussed in a qualitative manner. Next, the strain fields obtained from the DVC analysis along with the measured loads by the P2R tensile tester are used to provide quantitative insights about the deformation of the sample at the network-level.

3.1.1 Qualitative Observations

Figure 3.1 shows the front-view (1) and side-view (2) of the freeze-dried sample in the (a) reference state and (b)-(d) after tensile deformations of 1200 μm, 1600 μm, and 2580 μm, respectively. By comparing these images, the evolution of the fibre network resulting from tensile deformation can be observed. First, between Figures 3.1 (a)-1 and 3.1 (b)-1, it seems that the fibres have become more visible, especially in the bottom of the image, after 1200 μm of displacement. This change in contrast can be associated with detachment of a layer of fibres at the surface from the rest of the sample. A closer look at the side-views of these samples, Figures 3.1 (a)-2 and 3.1 (b)-2, reveals some out-of-plane expansion at the bottom of the sample. Second, the initial signs of failure are already evident in the lower region of Figure 3.1 (c)-1, after deformation of 1600 μm has been applied. Specifically, there is a large area that seem to be less dense when compared to the reference state, indicating fibre pull-out. This is made further clear in Figure 3.1(d)-1, with 2580 μm of deformation, as there are a large number of fibres at the bottom of the sample that seem to be aligned in the direction of the load, further indicating fibre pull-out. Although no rupture zone (in its conventional form) was observed during the deformation process, failure in this sample was identified to occur at 1200 μm based on a drop in the measured load. This will be further examined in Section 4.1.2. Fibre pull-out in this sample was expected to occur, since as explained in section 1.1.2.3, the freeze-drying process results in extremely weak inter-fibre bonds due to a reduction in the Campbell effect. The handsheet's weakness is further magnified by the low conformability of the constituent fibres that result from the fact that they have not been refined. A comparison between the side-view images of Figure 3.1 (a)-(c) shows an increase in the sample thickness with increasing deformation. This thickness expansion was most pronounced at the bottom of the sample, inside the failure region. Further increase of deformation resulted in reduction of sample thickness inside the failure region, as evident from comparison of Figure 3.1 (c) and (d). This thickness reduction is associated with the fact that fibres were pulled-out from the sample. This is also evident from Figure 3.1 (d-1), where, as can be seen, parts of the sample at the bottom left is missing. Furthermore, the observed thickness expansion is contrary

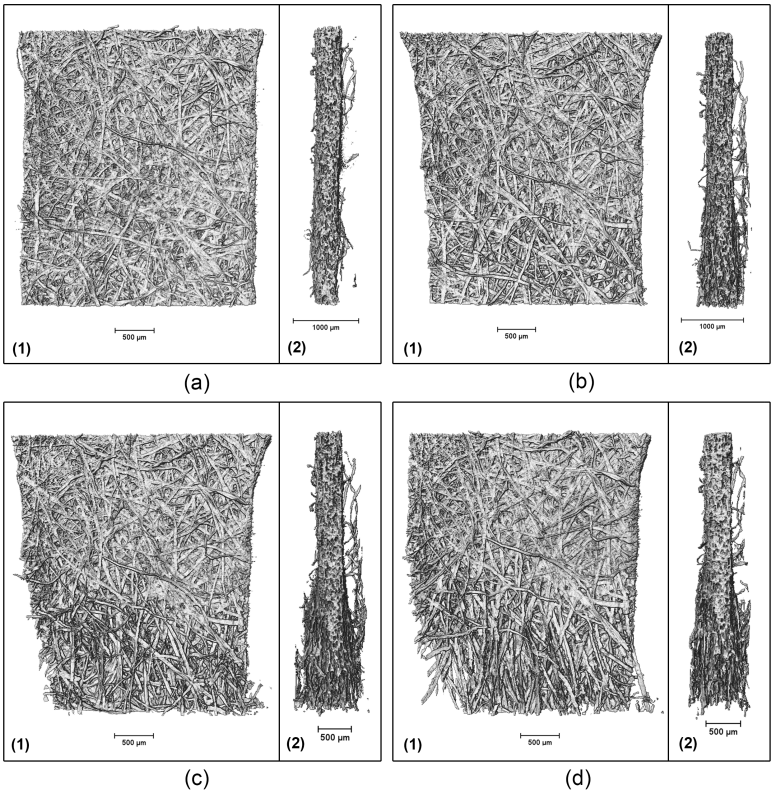

Figure 3.1: (1) Front-view (2) side-view visualization of the freeze-dried sample in (a) reference state, (b) deformation of 1200 μm, (c) deformation of 1600 μm, and (d) deformation of 2580 μm

to the hypothesis made in [47] that there will not be significant increase in sheet thickness (i.e. auxetic behaviour) during deformation of paper samples having weak hydrogen bonding, like freeze-dried handsheets, since the fibres would simply slide past each other and have significant opportunity to occupy the empty spaces.

3.1.2 Quantitative Insights

Figure 3.2 shows the in-plane strain (ϵ_{zz}) fields obtained from DVC analysis of the freeze-dried sample in the direction of the tensile load (z-direction) at deformations of (a) 200μm, (b) 400μm, (c) 600μm, and (d) 1000μm. The red regions show the areas of low in-plane strain while the yellow regions indicate the areas of high in-plane strain of greater than 0.08. As evident from Figure 3.2 (a), a narrow band of high in-plane strain is formed at the bottom of the sample at early stages of deformation. A comparison of the calculated strain fields, Figure 3.2 (a)-(d), reveals

that the magnitude of the in-plane strain in this region increases with increasing amount of deformation. This is consistent with the observations that were made from Figure 3.1, where fibre alignment and pull-out were observed at the bottom left of the sample. Consequently, it can be concluded that for the freeze-dried sample, the in-plane strain concentrates very early in the deformation process in a narrow region of the paper. This localization then grows in magnitude and size to become the failure region. This agrees with the findings of Ranger and Hopkins [134] and Borodulina et. al. [135] that plastic deformations in paper tend to concentrate along lines that move across the sample at an angle with respect to the applied external load similar to shear band formation that typically happens in ductile materials. Korteoja et. al. [136] also obtained similar deformation patterns using back-lit photographs of strained silicon impregnated paper samples, which also showed that plastic deformations in paper are highly nonuniform. They also observed that the site of eventual failure can visually (i.e. from plastic strain) be identified long before failure [136] which is also evident from the obtained strain fields.

Figure 3.3 shows the out-of-plane (ϵ_{yy}) strain fields obtained from DVC analysis of the freeze-dried sample at deformations of (a) 200μm, (b) 400μm, (c) 600μm, and (d) 1000μm. Similar to Figure 3.2, the red regions show the areas that exhibit small out-of-plane deformations, while the yellow regions indicate the areas that exhibit larger amounts of out-of-plane deformation. One should note that to facilitate the data visualization the maximum value of the strain is capped at 0.2. Therefore, the white regions indicate areas that have out-of-plane deformations of 0.2 or larger. As can be seen from Figure 3.3 (a), a region of high out-of-plane strain is formed at the bottom of the sample at early stages of deformation. A comparison between the out-of-plane strain fields in Figure 3.3 (a)-(d) reveals that such areas of high out-of-plane strain (yellow regions) grow in size and magnitude with increasing amount of tensile deformation. This is consistent with the observations that were made from Figure 3.1, where increasing amount of deformation was associated with thickness expansion of the sample, especially in or around the failure regions. This is also evident from a comparison of Figures 3.2 and 3.3 that shows that the large out-of-plane deformations are mainly concentrated in or around the regions that are associated with large in-plane deformations (i.e. failure regions). Such out-of-plane thickness expansions have

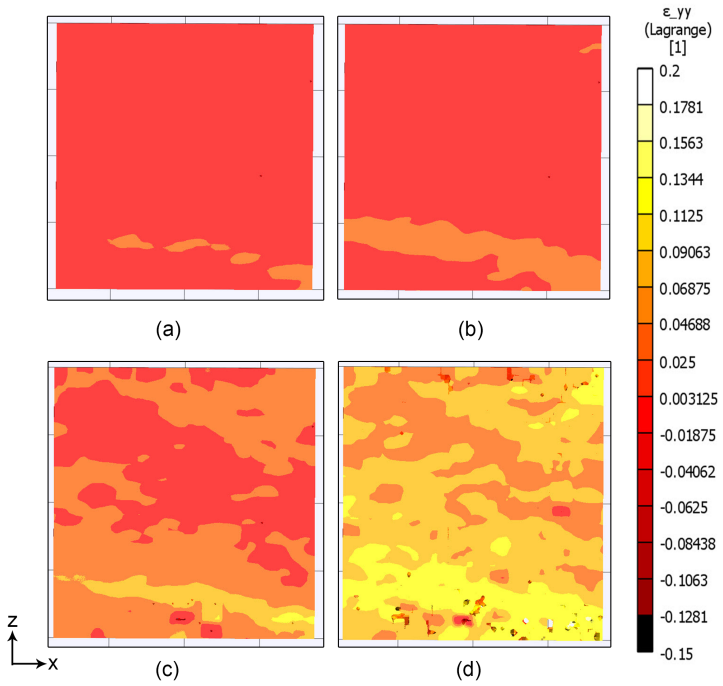

Figure 3.2: DVC calculated strain fields in the in-plane (z) direction of the freeze-dried sample at deformations of (a) 0.2mm (b) 0.4mm, (c) 0.6mm, and (d) 1mm

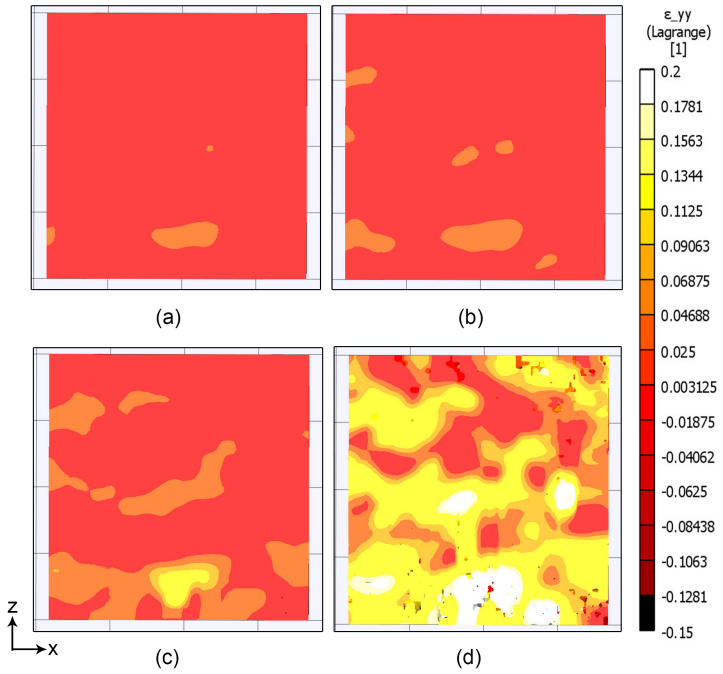

Figure 3.3: DVC calculated strain fields in the out-of-plane (y) direction of the freeze-dried sample at (a) reference state (b) deformation of 1200 μm, (c) deformation of 1600 μm, and (d) deformation of 2580 μm

been previously reported in the literature [44, 135].

3.1.3 Measured Loads and Strain Norms

Figure 3.4 plots the measured loads and the norm of the out-of-plane strain fields, N_{yy}, against the P2R cross-head displacement for the freeze-dried sample. The y-axis on the left indicates the loads in (N), while the y-axis on the right indicates the norms. The norm of the strain fields was determined by performing a 2-norm calculation on the 2D matrix that resulted from averaging strain values through the thickness of the samples. The 2-norm of the resultant matrix can be calculated from the following equation [137]:

$$\|A\| = \sqrt{\sum_{ij} |u_{ij}|^2} \tag{3.1}$$

where u_{ij} is the through-thickness average of the out-of-plane strain at the point ij. In other words, the norm is calculated by performing square root of sum of squares of the through thickness average strain values of the strain fields for each sample. Therefore, the norm of the strain values, in fact, quantifies the accumulated deformation by adding both the contraction and expansion that has occurred inside each sample. In this way, the norm will in fact provide a quantity to compare the amount of accumulated deformation inside different samples. The norms are calculated until the peak load is reached, after which failure is assumed to have occurred. Beyond this point, the sample is expected to have large deformations and missing fibre segments as a result of fibre pull-out. VicVolume® cannot handle the analysis of such samples where parts of the data from reference state is missing in the deformed volume, in which case the analysis will yield large erroneous values for strain fields. As can be seen from Figure 3.4, the norm of the out-of-plane strain fields increases with increasing tensile deformation. This is consistent with the expected auxetic behaviour of paper. However, while there is a relatively large increase in N_{yy} at later stages of deformation, the increase is small early-on. The plot of the N_{yy} versus P2R head displacement has a concave up trend, which is qualitatively similar to the plot of normalized cumulative acoustic events and homogeneous damage variable D as reported by Isaksson et al. [36], and explained in Section 1.1.1.3. This trend has also been observed for Poisson's ratios of some paper samples in the literature [42, 44, 47].

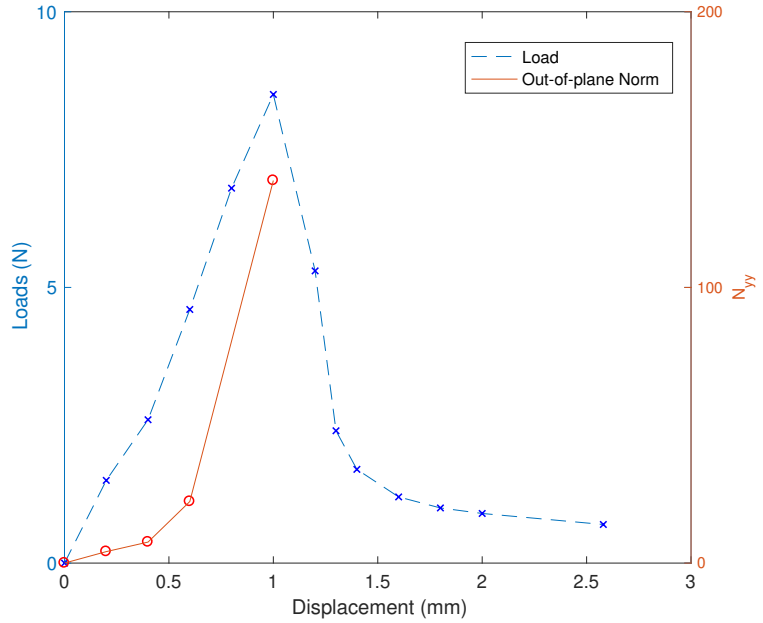

Figure 3.4: Peak load (blue dashed line) and out-of-plane strain norm (red solid line) of the freeze-dried sample from 4D imaging tests as a function of P2R tensile-tester cross-head displacement

Sample Scale Although the loads can be measured using the in-situ tensile testing equipment during 4D imaging experiments, it's worth noting that such measurements are not comparable to the standard tensile tests of paper. First, the high energy x-ray beams can damage the paper which was observed in this study as some of the samples exhibited colour change. This damage could lead to loss of strength. Second, the scale of the samples are not as advised by the standard TAPPI procedure (15mm). The gauge length and width of the samples in this study were 3mm and 2.8mm, respectively, which was dictated by the field-of-view of the synchrotron x-ray imaging equipment of 4×4×4 mm, as it was intended to capture the whole width of the samples during the in-situ tensile deformation. However, it was close to the fibre length as NBSK fibres are around 3mm long. Furthermore, as it was explained in Section 1.1.1.3, the gauge width of low grammage and low bonding samples are possibly smaller than their characteristic length resulting in inaccurate strength measurements. In addition, Hagman and Nygårds [138] also used tensile testing and speckle photography to study the effect of size in in-plane tensile testing of paperboard, and concluded that the strain behaviour of their samples is dependant on the

length to width ratio of the samples and cannot be predicted by standard tensile tests. Therefore, in general, considering the scale of the samples of this study, the strength measurements in here cannot be related to the values reported in the literature that have been obtained following standard tensile testing procedures. However, considering that the sample scale has been kept consistent throughout the experiments, the scale of the sample are not expected to significantly influence the comparative study of deformation mechanisms of this research.

3.2 Fibre-level Analysis

Although observations made at the network-level leads to some interesting insights about deformation of the freeze-dried sample, especially the presence of large out-of-plane strain regions inside and near the failure regions, it is still difficult to make comments about the underlying mechanisms for the observed deformations using network-level analysis. In this section the improved segmentation algorithm is used to segment a set of freeze-dried fibres at different levels of deformation for qualitative study of deformation at the fibre level. In addition, the developed post-processing codes for curl index and RCA are also used to obtain quantitative insight.

3.2.1 Qualitative Analysis of the Deformed Regions

Figure 3.5 (a) provides an overview of the fibre structure at a deformation of 1200μm with four manually segmented fibres highlighted in a region of interest. Figure 3.5 (b) shows three horizontal slices of the same cross-section in the (b)-1 reference state, (b)-2 1000μm, and (b)-3 1200μm displacement states. A comparison between Figures 5 (b)-1 and (b)-2 reveals that after 1000 μm of displacement, only the green fibre has sustained any deformation; the remaining fibres do not appear deformed nor displaced. By 1200μm of displacement, the blue fibre has clearly detached from the red fibre, and also appears to have deformed. In addition, the separation between the green and the blue fibre have also increased. Although Figure 3.5 (b) provides some ability to study fibre deformation, it is quite difficult to identify deformation mechanisms using only 2D cross-sectional slices as only one cross section of the fibre is visible at a time. Figure 3.5 (c) shows a 3D visualization of the four segmented fibres from

the region of interest: (c)-1 in the reference state, (c)-2 after deformation of 1000μm, and (c)-3 after deformation of 1200μm. Most parts of these fibres were segmented using the improved segmentation algorithm developed in this thesis; however some manual merging and refining was also required. By comparing Figures 3.5 (c)-1 and (c)-2, it is evident that the process of deformation resulted in a straightening of the green fibre, and that this straightening led to an increase in the separation between the green and the blue fibres near the middle kink of the blue fibre. Furthermore, as evident, the green and the blue fibres were also detached near the bottom of the fibres while remaining attached at the middle part. It is also evident from Figure 3.5 (c)-3 that after deformation of 1200μm the blue and the green fibres became completely detached from each other. However, the yellow and the blue fibres remained attached. It also appears that the blue and yellow fibres translated downwards, suggesting that they were being pulled out. Overall, these observations show that in a freeze-dried handsheet, an increase in fibre separation due to fibre straightening occurs during the early stages of deformation, while complete detachment, i.e. inter-fibre bond breakage, is also prevalent at later stages of deformation, resulting in failure.

Figure 3.6 shows a 3D visualization of a set of 18 segmented fibres. The blue fibres were segmented from a deformed configuration after a P2R cross-head displacement of 200μm, while the yellow fibres depict the same fibres segmented from a configuration after a displacement of 1000μm. One should note that some of the segmented fibres were manually refined since it is virtually impossible to segment the exact same segments of the fibres within two different volumes using only the developed automatic segmentation algorithm. The segmentation algorithm is capable of segmenting at least 80 fibres inside the deformed volumes of the freeze-dried sample that have fibre lengths of more than 0.5mm. Among those fibres, 18 fibres have been chosen based on the fact that their similar segments have been segmented inside the two volumes. As can be seen, the fibres at the bottom left of the sample exhibit noticeable movements, while the fibres at the top of the sample have negligible deformation. This is consistent with the observations that were made from Figures 3.1, 3.2 and 3.3, i.e. deformation at the network level was at the bottom and to the left. However, it is difficult to characterize fibre-level deformation by such qualitative observations. This necessitates quantitative calculations such as curl index and RCA measurements. In

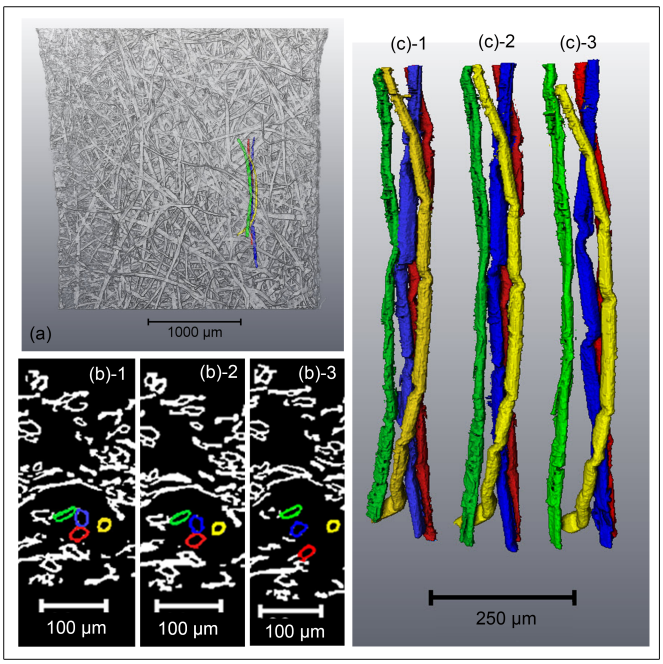

Figure 3.5: (a) 3D visualization of the freeze-dried sample after being deformed to 1200 μm; (b) Cross section of the same sample and (c) segmented fibres in the region of interest at "-1" reference state, "-2" deformation of 1000 μm, and "-3" deformation of 1200 μm.

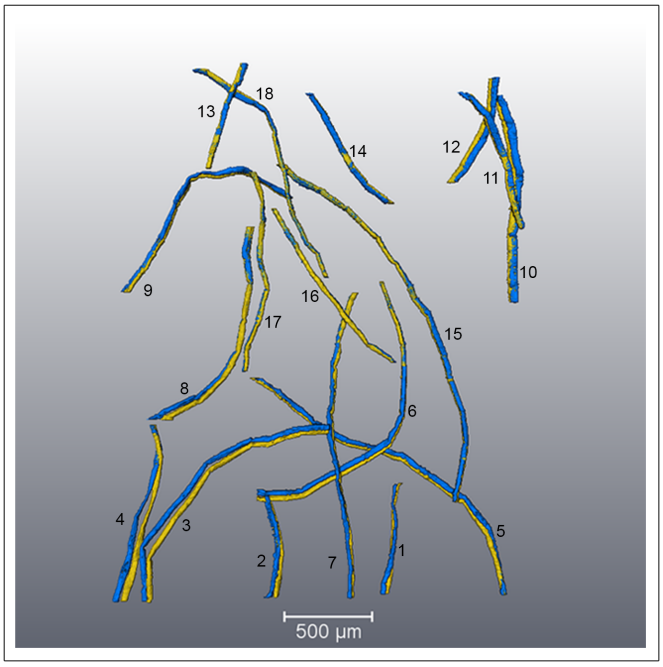

Figure 3.6: 3D visualization of the segmented fibres inside the reference configuration (blue) and deformed configuration at 1 mm (yellow) of the freeze-dried sample using the improved segmentation algorithm.

the following section, the number shown beside each fibre of Figure 3.6 will be used for quantitative comparison between the two deformed states.

3.2.2 Quantitative Insights

Segmentation of same fibre segments within different deformed volumes just using automatic segmentation algorithm is a challenging task since deformation of the sample can induce some morphological changes to the fibre lumens making it difficult to track the whole fibre inside different image volumes automatically. Therefore, some manual refining was performed to ensure that the same regions of each fibre segmented from two different image volumes were being compared in a quantitative manner. Fibre length can be used as an indicator to ensure similarity of the segmented fibres. Figure 3.7, shows a plot of fibre lengths of the segmented fibres inside the two deformed volumes of the freeze-dried sample; The blue bars indicate the fibre lengths inside the reference volume (deformation of 200μm), and yellow bars indicate the lengths of the same fibres inside the volume deformed at 1000μm. The x-axis indicates the fibre numbers that were assigned to each fibre as shown in Figure 3.6. The red bars also show the relative change in the fibre lengths from the first configuration to the second configuration. As evident, the fibre lengths mostly match each other and the relative change is small. This indicates that the same segments of each fibre are segmented from the two volumes. The small changes in the fibre lengths are mainly associated with fibre movements and deformations that have caused the fibres to move in or out of the field of view.

3.2.2.1 Relative Contact Area

Figure 3.8 shows the calculated RCA for the segmented fibres inside two different configurations of the freeze-dried sample using the method developed in this thesis; The blue bars show the RCA of the fibres after a cross-head displacement of 0.2μm, while the yellow bars show the RCA of the same fibres after displacements of 1000μm. The relative change of the RCA of the segmented fibres between the two configurations are also shown by the red bars. As evident, while the amount of RCA for almost half of the fibres remained the same with increasing amounts of deformation, for the rest of the fibres both reduction and increase in RCA were observed. To give an

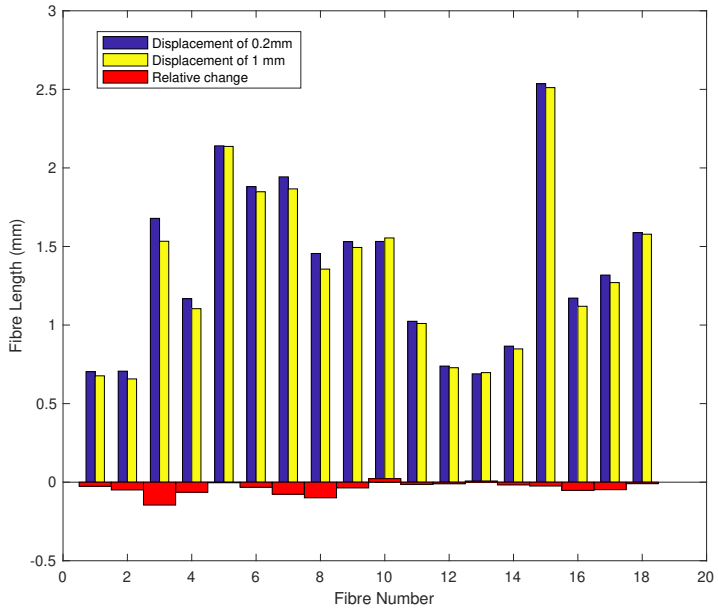

Figure 3.7: Fibre lengths of the segmented fibres of the freeze-dried sample (as shown in Figure 5) at displacements of (blue) 200μm, and (yellow) 1000μm, along with their relative change (red).

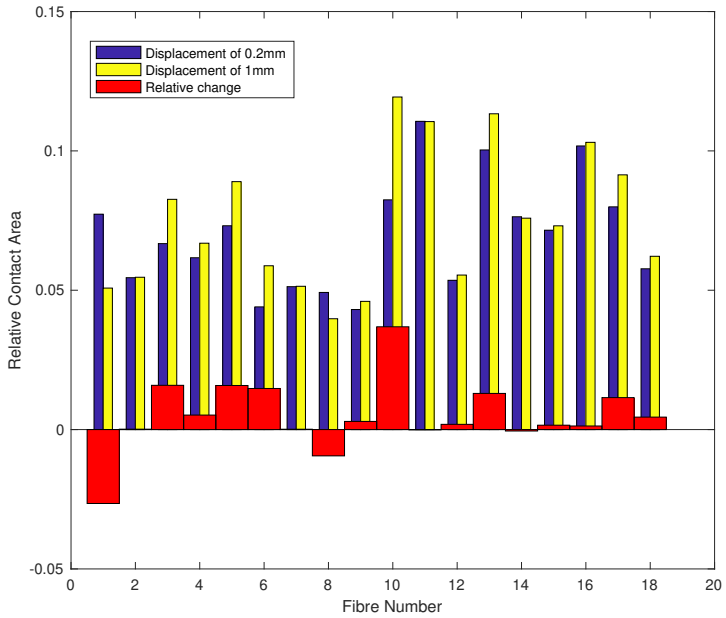

Figure 3.8: Relative Contact Area of the segmented fibres of the freeze-dried sample (as shown in Figure 5) at displacements of (blue) 200μm, and (yellow) 1000μm, along with their relative change (red).

example, fibre number one, located at the bottom of the sample (i.e. in or near the failure region) exhibited the biggest loss in RCA. This is consistent with qualitative observations that were made from Figure 3.5, where the blue fibre was observed to loose contacts with other fibres indicating inter-fibre bond breakage. One should note that RCA measurements are very sensitive to the quality of segmentation, and since some manual refining were required for merging of different segments of segmented fibres, despite best efforts, it was very challenging to remain consistent with manual refining of such segments. Overall, it seems that although it is difficult to generalize the change in RCA, and possibly inter-fibre bonding, during deformation of the freeze-dried sample, inter-fibre bond breakage happens in and around the failure regions of this sample. Since fibre detachments can result in a significant increase in fibre-fibre distance, it is also considered to be a contributing factor to the large out-of-plane strains measured inside the failure regions.

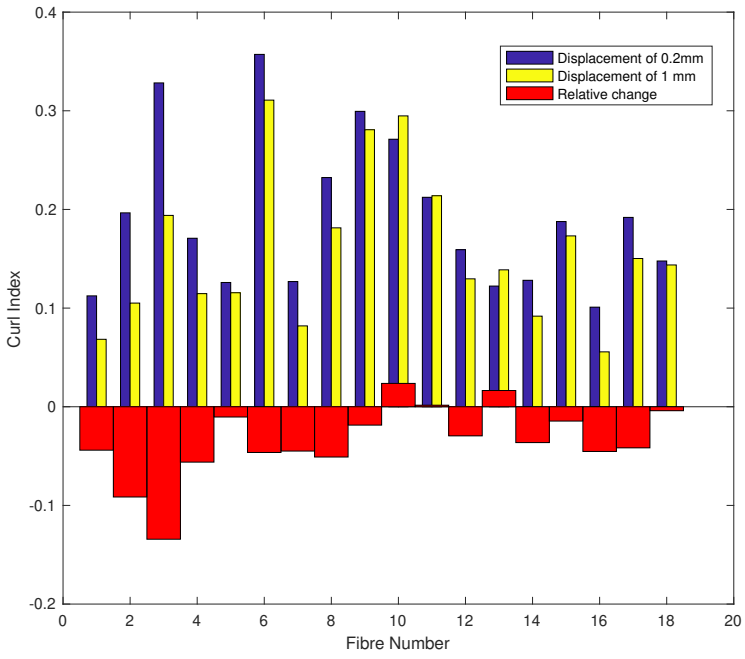

Figure 3.9: Curl Index of the segmented fibres of the freeze-dried sample (as shown in Figure 5) at displacements of (blue) 0.2mm and (yellow) 1000μm, along with their relative change (red).

3.2.2.2 Curl Index

Figure 3.9 shows the calculated curl index of the segmented fibres inside two different configurations of the freeze-dried sample using the method developed in this thesis; While the blue bars show the curl index of the fibres after a cross-head displacement of 200μm, the yellow bars show the curl index of the same fibres after displacements of 1000μm. The relative change of the curl index of the segmented fibres between the two configurations are also shown by the red bars. As evident, most fibres exhibit a reduction in the curl index value which is an indication of fibres being straightened. This is consistent with the expected auxetic behaviour of paper, and the general trend that were observed for the out-of-plane strain fields, since fibre straightening is considered to be the main mechanism responsible for auxetic behaviour of paper [42, 44, 47]. Only two fibres (No. 10 and 13) show an increase in the value of curl index with increasing deformation that translates to the fact that those fibres have become more curly (i.e. their "contour length" has increased.) This can be an indication of deflection of those fibre segments under compressive forces. As can be seen, the amount of relative change becomes mostly less negative as the assigned fibre number increases. As the lowest numbers are generally assigned to the fibres at the bottom of the sample, the biggest reduction in the curl index values are observed for fibres at the bottom of the sample. This shows that fibres inside or near the failure regions (bottom of the sample) show higher amounts of straightening, which is consistent with the previous observations of large thickness expansions in those regions. Since the main failure mechanism for the freeze-dried sample is known to be fibre pull-out, this is believed to stem from the fact that during fibre pull-out fibres have more opportunity to become straightened compared to the the fibres inside the rest of the network that are constrained by other fibres. Therefore, in general, such large amounts of fibre straightening, in addition to possible inter-fibre bond breakage, are considered to be the main contributing factors to the large out-of-plain strains observed in and near the failure regions. Overall, it can be concluded that both fibre straightening and fibre curling happens during deformation, although fibre straightening is more prevalent. In addition, straightening of the fibres in and around the failure regions where fibre pull-out happens are larger than the rest of the fibres.

3.3 Summary

In this chapter the results of the 4D imaging experiment were used for both qualitative and quantitative insights. At the network-level from the 3D visualization of the freeze-dried sample it was evident that the failure happened at the bottom of the sample. It was also evident from the side-views of the 3D visualizations that the thickness of the sample increased with increasing tensile deformations. Furthermore, it was evident that the thickness expansion was larger at the bottom of the sample where the failure was observed. In-plane and out-of-plane strain fields were calculated using the DVC analysis. From in-plane strain fields it was evident that the strain was concentrated in a narrow band at the bottom of the sample that grew in size and magnitude with increasing tensile deformations. The out-of-plane strain fields also showed signs of strain concentration at the bottom of the sample that grow in size and magnitude with increasing tensile deformation. The areas of large out-of-plane strain fields were also observed to be in and around the regions of high in-plane strain confirming the previous qualitative observations.

At the fibre-level, four fibres inside the freeze-dried sample were segmented and manually refined. Qualitative observations showed that fibres became straightened at earlier stages of deformation, while at later stages some of the fibres were completely detached from each other that can be taken as a sign for existence of inter-fibre bond breakage during tensile deformation of the freeze-dried sample. Furthermore, 18 fibres were chosen from the segmented fibres inside the sample that had lengths longer than 0.5mm at two stages of deformation. While, fibres at the bottom of the sample showed some noticeable movements, the rest of the fibres had negligible deformation. Fibre lengths of the segmented fibres were used as a measure to show that the same segments of each fibre were segmented inside the two different image volumes. RCA of the segmented fibres were also calculated using the algorithm developed in this thesis. While almost half of the fibres had negligible change in their RCA values, one fibre at the bottom of the sample showed some noticeable loss in its RCA. This also confirmed the qualitative observations that inter-fibre bond breakage may happen in and around the failure regions of the freeze-dried sample during tensile deformation. As inter-fibre bond breakage will result in an increase in the distance between the

detached fibres, such bond breakage were also considered to be a contributing factor to the observed large strain values in the out-of-plane strain fields. Furthermore, curl index of the segmented fibres were also measured using the method developed in this thesis. It was found that while most of the fibres straightened during tensile deformation, two fibres showed an increase in the curl index meaning that those fibres had become more curly. In addition, the relative change in the curl index (i.e. fibre straightening) were more pronounced for the fibres that were located at the bottom of the sample (i.e. in and near the failure regions). This was believed to happen as fibres during pull-out become more straightened compared to the fibres from the rest of the paper network that are constrained by other fibres. This showed that large amounts of fibre straightening, in addition to possible inter-fibre bond breakage, were also a contributing factor to the larger out-of-plane strain values that were observed in or around the failure regions. Therefore, it was suggested that when a paper network has more contribution from fibre pull-out it will exhibits larger values of out-of-plane strain before failure. Consequently, the out-of-plane strain norms of paper handsheets can be used as a measure to determine the relative contribution of fibre pull-out to the overall failure.

Chapter 4

Industrial Applications

The analysis of the freeze-dried sample in the previous chapter lead to the conclusion that there exists a correlation between the out-of-plane strain fields and the contribution of fibre pull-out to deformation and failure of the freeze-dried sample. Since paper networks with higher amounts of fibre pull-out are considered to have less efficient networks, this correlation, therefore, can also be used to compare the network efficiency of different paper samples. These findings are used in this chapter to study the effect of refining and pulp mixture on deformation of paper addressing the interest of the industry. For the effect of refining, qualitative and quantitative analyses of the 4D imaging experiments on three softwood samples with different levels of refining (i.e. 0, 60 , and 100 kWh/t) and the freeze-dried sample are used. Next, the same approach is used to evaluate the effect of fibre mixture on such mechanisms. To do so, the results of 4D imaging on 6 samples made from pulp blends with different levels of separately refined hardwood/softwood fibres (i.e. 100%Eucalyptus - 0%NBSK, 90%Eucalyptus - 10%NBSK, 80%Eucalyptus - 20%NBSK, 60%Eucalyptus - 40%NBSK, 20%Eucalyptus - 80%NBSK, 0%Eucalyptus - 100%NBSK) are studied. Finally, a summary of the findings is presented.

4.1 Effect of Refining

Refining is known to increase the network efficiency of paper samples by increasing the extent of inter-fibre bonding through mechanisms that were explained in Section 1.1.2.1. In this section this phenomenon is studied using 4D imaging experiments.

First, qualitative observations of the paper networks are used to study the effect of refining. Next, quantitative analysis including the out-of-plane strain norms are used for this evaluation.

4.1.1 Qualitative Observations

Figure 4.1 shows the front-views of the 3D visualization of the samples. Figure 4.1 (a) shows the freeze-dried sample and Figures 4.1 (b)-(d) show the samples that were refined at refining energies of 0, 60, and 100 kWh/t, respectively. As was observed in Section 3.1.1, the freeze-dried sample exhibits large amount of fibre pull-out. As can be seen from Figure 4.1 (b)-(d), definitive rupture zones were captured for the samples refined at 0, 60, and 100kWh/t. By a comparison between Figures 4.1 (b)-(d) it is evident that the number of unbroken fibres in the fracture zone decreases with increasing refining energy. This indicates the fact that the contribution of fibre pull-out to deformation and failure decreases with increasing refining energy, and consequently, as expected, higher refining energies leads to more efficient paper networks.

Figure 4.2 shows the side views of the 3D visualizations of the same samples as in Figure 4.1; Figure 4.2 (a) shows the side-view of the freeze-dried sample, and Figures 4.2 (b)-(d) show the side-views of the samples that were, respectively, refined at 0, 60, and 100 kWh/t. The images on the left show the samples at the reference state, while the images on the right show the samples after failure. The failure regions that were observed from Figure 4.1 are indicated by a dashed-line rectangle for each sample. A comparison between the left images of Figures 4.2 (b)-(d) shows that with increasing amounts of refining energy, in general, the samples become thinner. This happens as with higher refining energies the fibres become more conformable that lead to larger bonding area between flexible fibres than between stiff fibres leading to a stronger paper sheet with denser paper networks [139, 140] . Furthermore, as was observed in Section 3.1.1, a comparison of the side-views of the freeze-dried sample shows a thickness expansion in and around the failure region. A comparison between the left and right images in Figures 4.1 (b) and (c) shows that such thickness expansions in and around the failure regions decrease with increasing refining energies. This reduction is due to the fact that higher refining results in the paper networks to have lower values of free fibre length (i.e. length of a fibre between two inter-fibre bonds)

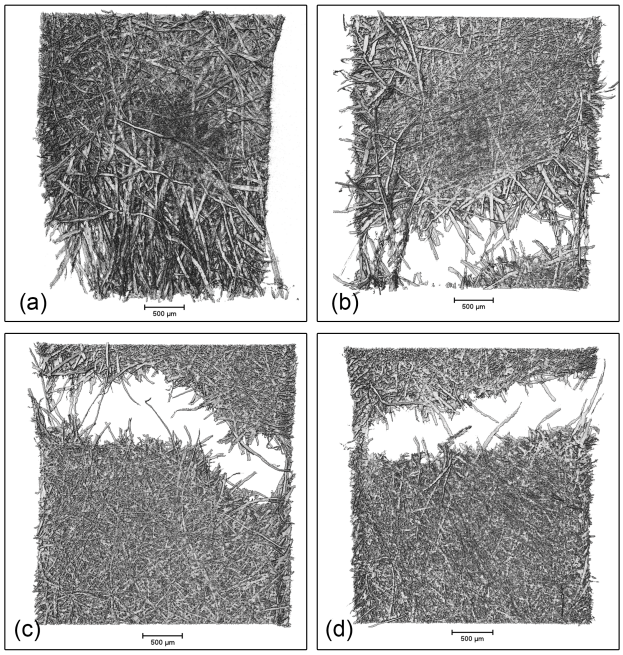

Figure 4.1: Front view of the (a) Freeze-dried sample, (b) 100% NBSK sample refined at 0kWh/t, (c) 100% NBSK sample refined at 60kWh/t, and (d) 100% NBSK sample refined at 100kWh/t after failure

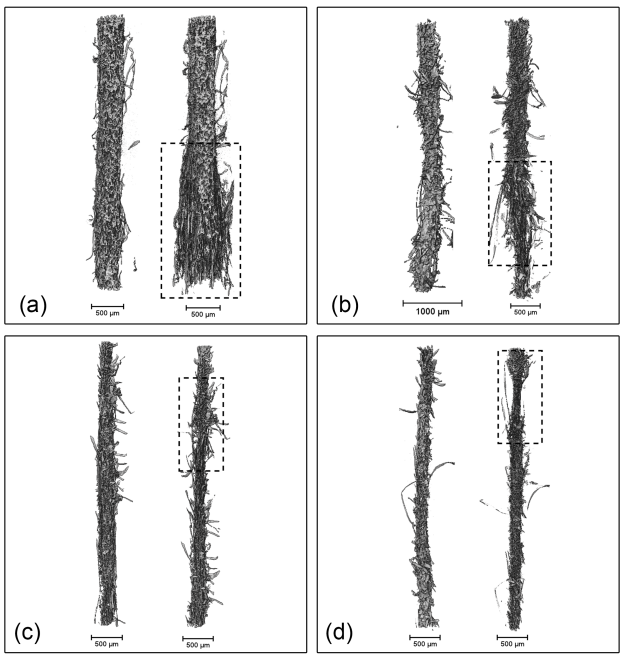

Figure 4.2: Side view of the (a) Freeze-dried sample, (b) 100% NBSK sample refined at 0kWh/t, (c) 100% NBSK sample refined at 60kWh/t, and (d) 100% NBSK sample refined at 100kWh/t at (left) reference configuration and (right) after failure with failed regions being indicated by dashed line rectangles

which leads to lower amounts of thickness expansion due to fibre straightening. In addition, paper samples that are refined at higher energies are expected to experience lower amounts of inter-fibre bond breakage contributing to such thickness expansions. A comparison between the left and right images in Figure 4.2 (d) shows that for the sample that were refined at 100kWh/t the thickness inside the failure region becomes even less than the thickness of the handsheet at the reference state, while the thickness around the failure regions shows some expansion. Overall, it can be concluded that the thickness expansion (i.e. auxetic behaviour) of paper samples show strong correlation with refining energies as samples with higher refining energies show lower amounts of thickness expansion.

4.1.2 Quantitative Insights

Figure 4.3 shows the evolution in load with displacement during 4D imaging for the 100% NBSK samples that were refined at 0, 60, and 100kWh/t and the freeze-dried sample. Recall that each test contained multiple samples, four for the softwood samples with different levels of refining and three for the freeze-dried sample. As can be seen, the load peaks at 32N for the sample refined at 100kWh/t at a displacement of 1400μm, then drops sharply afterwards, while for the samples refined at 60 and 0kWh/t, and the freeze-dried sample the values are 21N, 19N, and 8.5N at displacements of 1200μm, 1200μm, and 1000μm, respectively. The significant drop in the load after the peak value is associated with the failure of one or two of the handsheet samples within a test. Interestingly, for the samples that were refined at 0, 60 and 100kWh/t, there is a slight increase in the load a few steps after the peak, after which it drops again to zero. This behaviour is associated with the deformation and failure of the remaining samples that had not previously failed. This post peak increase is not seen for the freeze-dried test, as the failure of all the samples for this test happened almost simultaneously. Further, the load drop for the freeze-dried sample is not sudden and it drops rather smoothly. This is because the deformation within the freeze-dried samples is mainly fibre-pullout, as shown in Chapter 3. Consequently, the fibres are still physically in contact even after failure until they are pulled apart.

Figure 4.4 shows strain contours from the DVC analysis of the acquired sCT datasets for (a) the freeze-dried sample, and 100%NBSK samples refined at (b) 0,

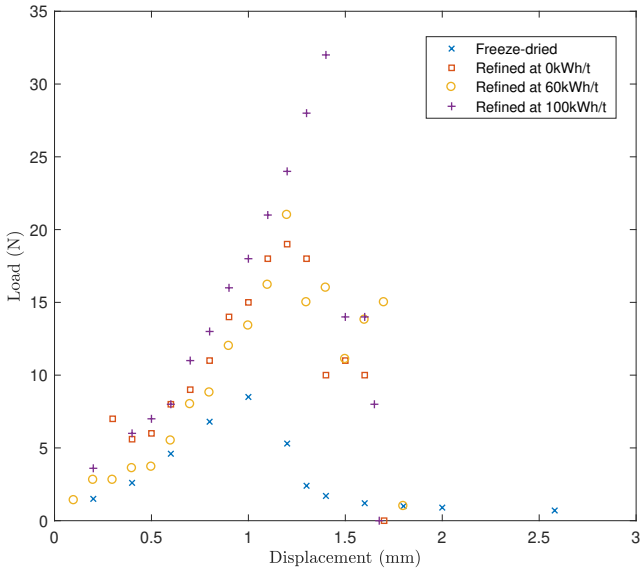

Figure 4.3: Peak loads of the freeze-dried, 100%NBSK refined at 0kWh/t, 100%NBSK refined at 60kWh/t, and 100%NBSK refined at 100kWh/t samples as a function of P2R tensile tester cross-head displacement

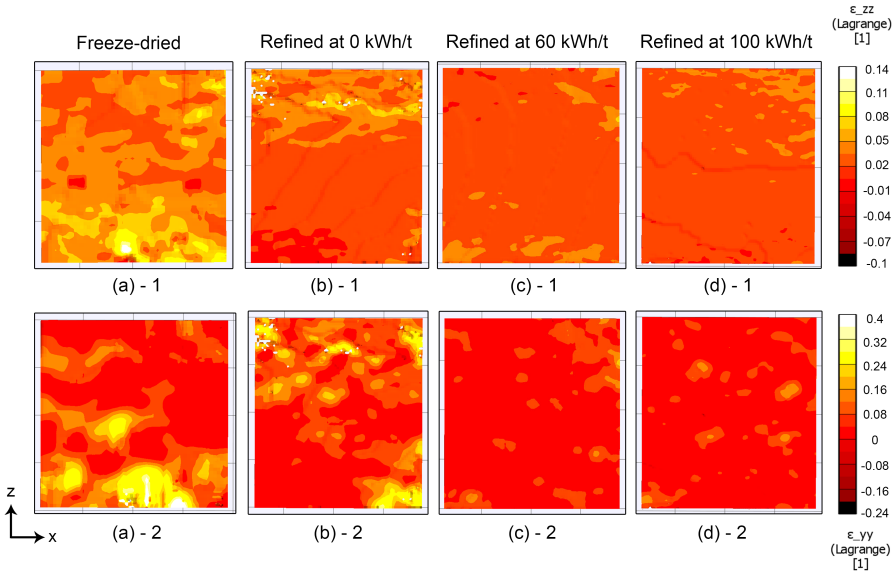

Figure 4.4: DVC calculated strain fields of the freeze-dried, 100%NBSK refined at 0kWh/t, 100%NBSK refined at 60kWh/t, and 100%NBSK refined at 100kWh/t samples as a function of P2R tensile tester cross-head displacement in "-1" in-plane (ε_{zz}), and "-2" out-of-plane (ε_{yy}) directions

(c) 60, and (d) 100kWh/t at the point just prior to failure. The top row of Figure 4.4, (a)-1 to (d)-1, shows the DVC calculated in-plane (ε_{zz}) strain fields, while the bottom row, Figure 4.4 (a)-2 to (d)-2, shows the corresponding out-of-plane (ε_{yy}) strain fields. To facilitate the comparison of the strain fields between the four samples, the values of in-plane and out-of-plane strain fields are capped at a maximum of 0.14 and 0.4, respectively, where the yellow and red regions identify areas with high and low in-plane deformation. As was observed in Section 3.1.2, there is a large region of high in-plane deformation at the bottom of the freeze-dried sample that is consistent with qualitative observations that showed the fibres were being pulled-out from the bottom of the sample. Further, a comparison between the in-plane and out-of-plane strain fields of this sample shows that large out-of-plane deformations seem to be concentrated in areas associated with high in-plane deformations. The same trend can also be observed for the softwood sample refined at 0kWh/t from Figure 4.4 (b). As can be seen from Figure 4.4 (b)-1, there is a narrow band of large in-plane deformation occurring near the top of the sample. In addition, as evident from Figure 4.4 (b)-2, for the most part, similar to the freeze-dried sample, the large out-of-plane deformations in this sample also occur in regions neighbouring the large in-plane deformations. In contrast, as evident from Figure 4.4 (c) and (d), the softwood samples refined at 60 and 100kWh/t contain very few regions that show large deformations, both in-plane and out-of-plane. This shows that for more efficient paper networks there is less accumulated damage before the failure leading to a more brittle like fracture for the softwood samples refined at 60 and 100kWh/t. This can be explained by the fact that more refined samples, due to the efficiency of their network, experience more uniform stress distribution during deformation. This is also clear from a comparison between the out-of-plane strain fields, Figure 4.4 (a)-2 to (d)-2, where the extent of yellow regions decreases from left to right as the network efficiency of the sample increases due to increasing refining energies (i.e. higher extents of inter-fibre bonding.) This is consistent with qualitative observations from Figure 4.2 in terms of thickness expansion in the freeze-dried, and softwood samples. The results shown in Figure 4.4 quantify the observations from Figure 4.2, that is, the freeze dried and the softwood sample refined at 0kWh/t show significant auxetic behaviour, while the softwood samples refined at 60 and 100kWh/t only show minimal auxetic behaviour.

The trends observed from the obtained strain fields confirms the findings of Borodulina et.al. [135], where they used particle-level simulation to model paper networks with varying levels of inter-fibre bonding and showed that the paper networks with lower levels of bonding show higher stress variations inside the network. They compared the in-plane strain fields obtained from the simulations with the patterns of bond failure inside the simulated networks and reported that the high strain regions in the network with lower levels of bonding matches the regions of bond failure, while for the network with high levels of bonding the areas of high in-plane strain does not match the regions associated with bond failures. This also agrees very well with the observed trends in the strain fields where large out-of-plane strain values, which is believed in here to be associated with the regions of inter-fibre bond failure, are concentrated mainly in and around the failure regions for the samples with lower levels of bonding (i.e. freeze-dried sample and softwood sample refined at 0kWh/t) and not much so for the rest of the samples. This further suggest that a comparison between in-plane and out-of-plane strain fields can be used as a criteria to evaluate inter-fibre bond breakage during deformation of paper samples. In other words, when regions of high out-of-plane strain concentration coincide with regions of high in-plane concentration it is an indication of inter-fibre bond failure. They also concluded that it is the high local in-plane strains due to network inefficiency that lead to inter-fibre bond failure, and not the other way around. However, the out-of-plane strain fields were not reported in their study. Regardless of the origin, this also confirms that strain localization can be used as a criteria for network efficiency.

Figure 4.5 plots the norm of the out-of-plane strain fields (N_{yy}) as a function of displacement for all the samples. The norms were calculated using the same way as explained in Section 3.1.3 and were measured until the last deformation configuration just before failure. Note that the results shown in Figure 4.5 correspond to samples of the multi-sample setup that failed just after the second load peak was reached, Figure 4.3. One should also note that the lines plotted between the measurement points do not imply a linear change between them, but instead were added to facilitate the comparison between the four samples. As can be seen, all three softwood samples show the same trend as the freeze-dried sample, an increase in N_{yy} occurs with an increase in displacement, which is consistent with the expected auxetic behaviour of

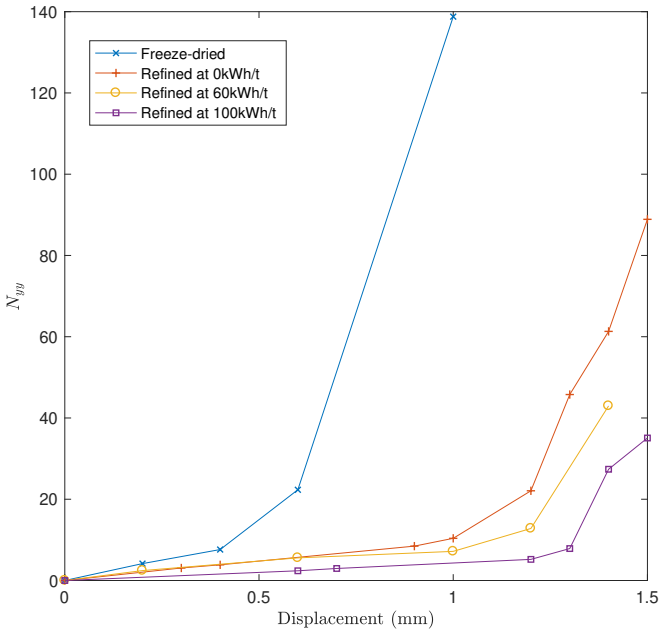

Figure 4.5: Out-of-plane strain norms of the freeze-dried sample, and the 100%NBSK sample refined at 0kWh/t, 60kWh/t, and 100kWh/t as a function of P2R tensile tester cross-head displacement

paper. Similar to the freeze-dried sample, while the increase in N_{yy} is small early-on, there is much larger increase in the later stages of deformation leading to the same shape of concave-up for all the plots. This trend, as mentioned in section 3.1.3, is consistent with observations for damage accumulation [36] and Poisson's ratios reported for some paper samples in the literature [42, 44, 47]. In general, the values for N_{yy} increase when the extent of inter-fibre bonding decreases (i.e. for less efficient paper networks). The changes in the values of N_{yy} between the samples that happen early-on during the deformation is believed to stem from the fact that more refined samples have a denser paper network that translates to lower values for free fibre length. This leads to lower values of thickness expansion due to fibre straightening during early stages of deformation. Interestingly, the difference amongst the values of N_{yy} for different samples increases drastically at the later stages of deformation where complete fibre detachments were observed. One should note that for the softwood fibres, refining up to 100kWh/t is expected to result in small amount of fibre shortening [141]. It is reported in [140] that for a 100% softwood samples a reduction of 3% in length weighted fibre length is observed after refining of 132kWh/t.

Therefor, possible fibre length reduction due to refining of the samples in this study is deemed negligible. This suggests that inter-fibre bond breakage is the main factor responsible for such large differences in the accumulated out-of-plane deformations of the samples with less efficient networks. In other words, for the less efficient paper networks the contribution of complete fibre detachment to N_{yy} becomes larger than the contribution of fibre straightening in later stages of deformation. This also agrees well with the findings of [135] where the reported percentage of fractured bonds as a function of in-plane strain for simulated paper networks with different levels of inter-fibre bonding show similar trends to that of the strain norms in this study. Therefore, it can be concluded that out-plane strain norms can be used as a criteria to compare the network efficiency of different paper samples (i.e. the extent of bond breakage.) Overall, considering that inter-fibre bond breakage is a precursor to fibre pull-out, it is proposed that the accumulated out-of-plane deformations can be used to quantify the accumulated damage and the contribution of fibre pull-out towards failure in paper handsheets.

4.2 Effect of Mixture

As explained in Section 1.1.2.2, the level of inter-fibre bonding is an important factor in prediction of the behaviour of the paper samples that are made from pulp blends of different fibres. Considering the findings of the previous sections that the out-of-plane strain norms compared with in-plane strain norms can be used as a measure to evaluate the levels of inter-fibre bonding in a paper handhseet, this section is intended to evaluate the viability of using such measurements to study the effect of pulp mixture on deformation of paper samples. To do so, the results of 4D imaging on 6 different samples with different levels of separately refined NBSK and Eucalyptus pulp are used. First, the image volumes are used for qualitative observations. Next, DVC analysis is used on the dataset to obtain quantitative insights on deformation of these samples.

4.2.1 Qualitative Observations

Figure 4.6 shows the front views of 3D visualizations of the image volumes obtained from 4D imaging of (a) 100% Eucalyptus, (b) 10% NBSK, (c) 80% NBSK, and (d) 100% NBSK samples after failure. Both NBSK and Eucalyptus fibres are separately refined at 60kWh/t. As can be seen, clear fracture zones are captured for all the samples. A comparison between Figures 4.6 (a) to (d) reveals that the number of unbroken fibres dangling inside the fracture zones increases with decreasing percentage of NBSK fibres. This shows that the addition of NBSK fibres results in less contribution of fibre pull-out to failure. This is due to the fact that longer NBSK fibres will result in more opportunities for inter-fibre bonding leading to more efficient paper networks.

Figure 4.7 shows the side views of the same samples as in Figure 4.6 at (left) the reference state and (right) after failure. Regions corresponding to the fracture zones are indicated by dashed-line rectangles. A comparison of thickness of the samples shows that while the 100% Eucalyptus sample, Figure 4.7 (a) left, has the lowest thickness, 100% NBSK sample, Figure 4.7 (d) left, has the highest thickness and the thickness of the samples, in general, increases with increasing percentage of NBSK fibres. This is due to the fact that Eucalyptus fibres have, generally, much lower diameters and lengths compared to the NBSK fibres, and addition of larger and longer fibres at the same levels of refining creates paper samples with higher caliper. A comparison of thickness of the samples between the reference state and after failure, left and right images of Figure 4.7 (a)-(d), shows that although some thickness reduction is observable inside the fractures zones, it is generally difficult to qualitatively evaluate any changes in the thickness that occur during deformation of the samples that have been subject to similar levels of refining. This necessitates a quantitative analysis of their image volumes.

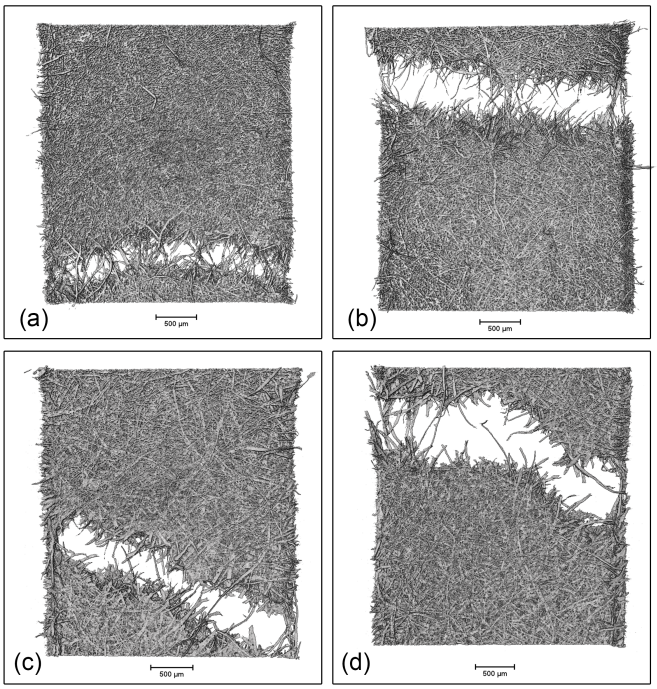

Figure 4.6: Front view of the (a) 100% Eucalyptus, (b) 10% NBSK, (c) 80% NBSK, and (d) 100% NBSK sample refined at 60kWh/t after failure

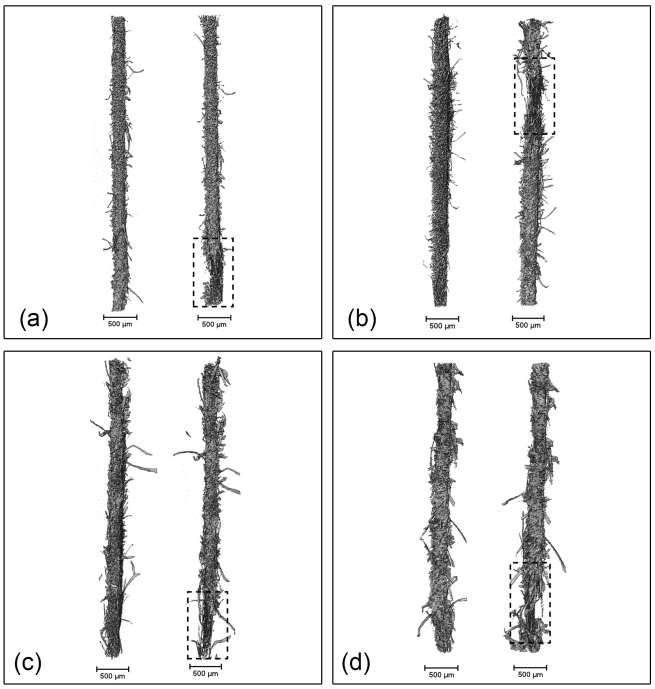

Figure 4.7: Side-views of the (a) 100% Euc., (b) 10% NBSK, (c) 80% NBSK, and (d) 100% NBSK samples refined at 60kWh/t at (left) reference state and (right) after failure with failed regions being indicated by dashed line rectangles

4.2.2 Quantitative Insights

Figure 4.8 shows the contour plots of the strain fields from the DVC analysis of the (a) 100% Euc., (b) 10% NBSK, (c) 40% NBSK, (d) 80% NBSK, and (e) 100% NBSK samples refined at 60kWh/t in '-1' in-plane direction (ϵ_{zz}), and '-2' out-of-plane direction (ϵ_{yy}). The strain values are capped at 0.14 and 0.4 for the in-plane and out-of-plane strain fields, respectively, to facilitate the comparison. The red regions show the areas of low strain, while the yellow regions show the areas of high strain values. A comparison of the in-plane strain fields, Figure 4.8 (a)-1 to (e)-1, shows that, except for the 40% NBSK sample that shows the largest extent of the orange regions, the extent of high strain regions increases slightly with increasing percentage of the NBSK fibres (i.e. from left to right). Furthermore, while the magnitude of the in-plane strain values are almost the same (i.e. all high strain regions are orange) for the first three samples from left, namely 100% Euc., 10% NBSK, and 40% NBSK samples, the existence of small yellow regions in Figure 4.8 (d)-1 and (e)-1 shows that there is an increase in the magnitude of the in-plane strain for the 80% NBSK, and 100% NBSK samples. The same trends can also be observed for the out-of-plane strain fields. As evident from out-of-plane strain fields of the 100% Euc. and 10% NBSK samples, Figure 4.8 (a)-2 and (b)-2, these samples show very little out-of-plane deformation before failure. In addition, a comparison of the out-of-plane strain fields for all the samples, Figure 4.8 (a)-2 to (e)-2, shows that both the extent and the magnitude of out-of-plane strain increase with increasing percentage of NBSK fibres in the pulp. In addition, as can be seen from Figure 4.8 (d)-2 and (e)-2, the areas associated with large out-of-plane strains (yellow regions) are again more or less concentrated around the areas of large in-plane strains that can be indicative of inter-fibre bond breakage.

Figure 4.9 shows the evolution of the out-of-plane strain norms (N_{yy}) with displacement. Strain norms are calculated using the same methods as explained in Section 3.1.3 until the last stage of deformation just before failure. It is worth noting that the lines connecting the data points are only to facilitate the comparison and does not imply a linear trend between each data point. Recall that the multi-sample setup had four samples for each test. In order to remain consistent, the values of N_{yy} are calculated using the strain fields from the samples in the same position within

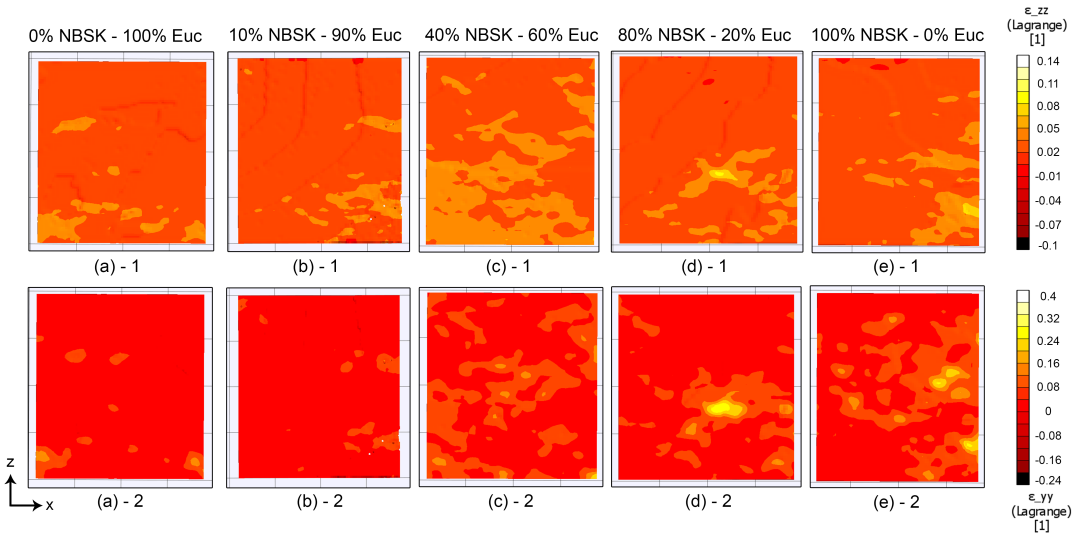

Figure 4.8: Strain fields obtained from DVC analysis of (a) 0%NBSK–100%Euc, (b) 10%NBSK–90%Euc, (c) 40%NBSK–60%Euc, (d) 80%NBSK–20%Euc, and (e) 100%NBSK–0%Euc samples refined at 60kWh/t in '-1' in-plane direction and '-2' out-of-plane directions

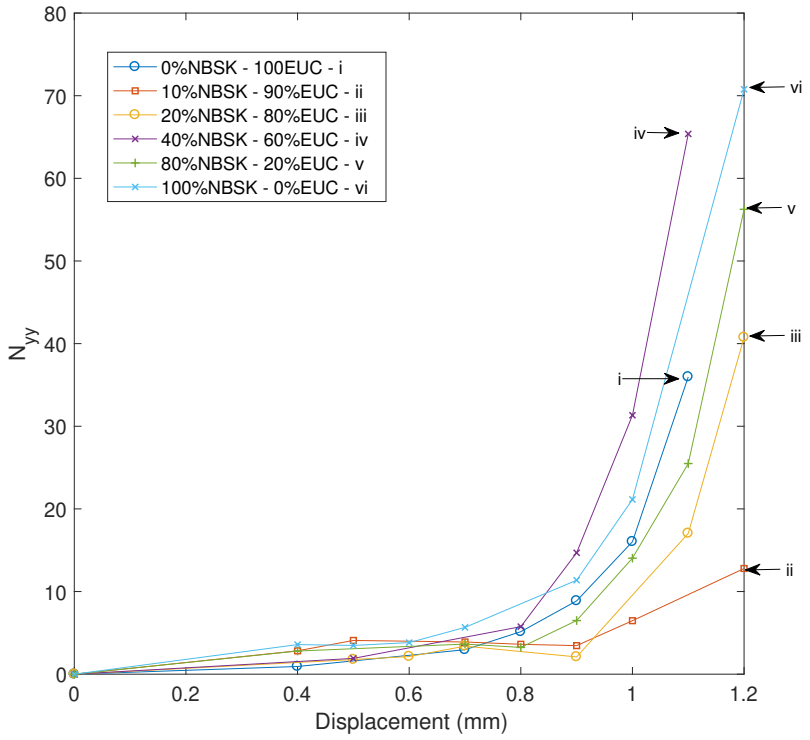

Figure 4.9: Out-of-plane strain norms (N_{yy}) of mixture samples as a function of tensile tester's cross-head displacement

the multi-sample setup. In this case, the first sample inside each multi-sample setup were used for all the tests with the exception of 100% Eucalyptus sample where the third sample was used. This choice was made based on the quality of the images that were obtained from the 4D imaging experiments, since DVC analysis on low quality data (i.e. blurry images) can result in erroneous strain values. In order to facilitate the comparison of the plotted values a roman numeral is assigned to each sample: (i)-100% Eucalyptus, (ii)-10% NBSK, (iii)-20% NBSK, (iv)-40% NBSK, (v)-80% NSBK, and (vi)-100% NBSK. In general, as can be seen, the N_{yy} increases with increasing displacements which is consistent with expected auxetic behaviour of paper samples. A comparison between the N_{yy} values of the 100% Euc, 10% NBSK, and 20% NBSK samples (i, ii , and iii) shows that with a slight increase in the percentage of the NBSK fibres in the pulp blend the values of out-of-plane norms decreases significantly. This is due to the fact that addition of the longer and more conformable NBSK fibres results in an increase in the extent of inter-fibre bonding leading to more efficient paper networks. Increasing the efficiency of paper networks, as concluded from the findings of the Sections 3.3 and 4.1, results in a decrease in the measured values of out-of-plane norms. A comparison of the N_{yy} values of the 40% NBSK, 80% NBSK, and 100% NBSK samples (iv,v,vi) shows that further increase of the percentage of NBSK fibres in the pulp blends results in an increase in the amount of the out-of-plane norms where N_{yy} values become almost equal or larger than that of the 100% Euc. sample. This trend is not consistent with the values reported by Verma [142] where the 100% hardwood samples when compared to 100% softwood samples show more rapidly increasing out-of-plane thickness as a function of axial strain. At first, it seems that since the out-of-plane norm values of these samples are equal or larger than the 100% Euc. sample, their network efficiency must be equal or less than this sample. However, this is not true since our qualitative observations showed less signs of fibre pull-out (i.e. unbroken fibres inside the fracture zone) for the 100% NBSK sample when compared to 100% Eucalyptus sample meaning that the former has higher network efficiency. The increase in the N_{yy} values for these samples is due to the fact that the addition of longer NBSK fibres results in longer free fibre lengths of the paper network that in return leads to larger out-of-plane thickness expansions when fibres are straightened during deformation. As evident from Figure

4.9, the 40% NBSK sample has the largest N_{yy} values for low amounts of displacement suggesting failure at lower cross-head displacement when compared to other samples. On the contrary, as evident from the extent of orange regions in Figure 4.8 (c)-1, this sample shows larger extents of in-plane deformation before failure when compared to other samples. This suggest a discrepancy in the readings for the displacement of this sample. Therefore, this sample is considered to be an anomaly in the observed trends. Overall, it seems that addition of small percentage of NBSK fibres to the Eucalyptus sample results in a large increase in the network efficiency (i.e. lower contribution of fibre pull-out to its failure) and as a result it shows less amount of out-of-plane deformation. However, a further increase in NBSK fibre content seems to increase the out-of-plane deformation which is explained by the increase in the free fibre length inside the paper networks and not the network efficiency. In other words, although the increase in the amount of NBSK fibres will result in more efficient paper networks leading to a decrease in out-of-plane norms, the increase in the free fibre length will counteract this reduction. This, in total, will lead to larger thickness expansions for the samples with higher levels of NBSK fibres.

In general, it seems that measurements of accumulated deformations alone cannot be used to evaluate the level of inter-fibre bonding in paper samples that are made from pulp blends with fibres of differing lengths. Therefore, the findings of this study regarding the mixture samples is inconclusive when it comes to evaluation of the levels of inter-fibre bonding, and therefore, it is not possible to conclude whether such samples should follow the linear mixture rule or not. This can be resolved by normalizing the measured out-of-plane strain values using the average or maximum thickness expansions achievable for each paper network to remove the possible extra contribution of longer free fibre lengths to thickness expansions of some samples. This can be done by utilizing geometrical or mathematical models such as the one suggested in [142]. This requires free fibre length measurements that can be obtained experimentally [143, 144], or by using mathematical models developed for random fibre networks [145, 146].

4.3 Summary

4D imaging experiments were used in this chapter to study the effect of refining and pulp mixture on deformation of paper samples. Image volumes obtained for three softwood samples that were refined at 0, 60, and 100kWh/t along with the freeze-dried sample were used to study the effect of refining. From qualitative observations of the captured fracture zones it was found that increasing refining energies lead to less contribution from fibre pull-out to failure consistent with the fact that more conformable fibres result in more efficient paper networks. Qualitative observations of the side views of the samples revealed thickness expansions in and around the failure regions that decreases with increasing refining energies. This was explained by the fact that higher refining energies result in more efficient paper networks with lower free fibre lengths leading to less contribution from inter-fibre bond breakage and fibre straightening to such thickness expansions. Strain fields obtained from DVC analyses were used to obtain quantitative insights about the effect of refining on deformation. In general, regions of high strain in both in-plane and out-of-plane strain fields increased in size and magnitude with decreasing extent of inter-fibre bonding (i.e. as the network of the sample became less efficient.) In addition, while in-plane strain fields of the softwood samples refined at 0kWh/t and the freeze-dried sample showed narrow bands of high strain concentration, the softwood samples refined at 60 and 100kWh/t showed little signs of accumulated damage before failure suggesting a more brittle fracture for these samples. This can be explained by more uniform stress distribution in the more efficient paper networks. Strain norms were also calculated from the obtained out-of-plane strain fields and were plotted against the cross-head displacement. In general, out-of-plane strain norms increased for all the samples with increasing displacements, which is consistent with the expected auxetic behaviour of paper material. While the difference between the out-of-plane strain norms of the samples were small early-on, it became more noticeable in later stages of deformation. It was concluded that the difference between the amount of inter-fibre bond breakage experienced by the lower efficient networks were the main contributing factor to such large differences observed at later stages of deformation.

To study the effect of mixture on deformation of paper, six samples made of

different levels of separately refined Eucalyptus and NBSK fibres were used. From qualitative observations of the captured fracture zones, it was clear that the number of dangling fibres inside the fracture zones decreased with increasing levels of NBSK fibres in the pulp blend. This is due to the fact that the longer NBSK fibres create more opportunity for inter-fibre bonding and lead to more efficient paper networks that exhibit less contribution from fibre pull-out to failure. A comparison of the side views of the samples showed that, in general, addition of longer and larger NBSK fibres to the pulp at the same level of refining results in paper samples that have higher caliper. In addition, a comparison between the side views at reference state and after failure revealed that the thickness expansions in and around the failure regions were difficult to notice qualitatively necessitating a quantitative approach. Strain fields of each sample in both in-plane and out-of-plane directions were obtained using DVC analyses of their image volumes. In general, the extent and magnitude of strain in both in-plane and out-of-plane directions increased with increasing content of NBSK fibres in the pulp blend. Plots of out-of-plane strain fields as a function of cross-head displacements showed that, in general, out-of-plane strain norms increased with increasing displacements for all the samples revealing auxetic behaviour as expected. A comparison between the plots showed that a small addition of 10 to 20 percent of NBSK fibres to the Eucalyptus sample leads to significant reduction in the calculated out-of-plane strain norms. This was rationalized by the increase in the network efficiency due to addition of longer NBSK fibres to the pulp blend. Further addition of NBSK fibres to the pulp blend resulted in an increase in the out-of-plane strain norms. This was explained by the increase of the free fibre length in the paper network due to addition of longer NBSK fibres and not the loss of network efficiency. These observations lead to the conclusion that out-of-plane strain norms are not a good criteria for evaluation of network efficiency of the mixture samples with fibres of differing lengths. This can be overcome by normalization of the obtained out-of-plane strain values based on the free fibre lengths measured experimentally or calculated theoretically.

Chapter 5

Mechanistic Insights

In the previous chapter it was shown that the qualitative and quantitative analysis of the image volumes acquired from 4D imaging experiments can be used to gain insights into the micro mechanisms that are active during tensile deformation of paper material. This chapter only focuses on measurement of Poisson's ratios of the samples using the obtained image volumes, and to complement the previous results, the effect of refining and mixture on these measurements are also considered.

5.1 Poissson's Ratios

As explained in Section 1.1.1.4, deformation of paper, similar to other materials, is a three-dimensional phenomenon where tensile deformations will also result in some lateral deformations. This effect is quantified by the ratio of lateral strain over axial strain, and is called Poisson's ratio. DVC has previously been used for measurements of Poisson's ratios of standard and auxetic foams [147], where two ways are suggested for such measurements. First, to create spatial maps for Poisson's ratios in each tomographic slice and then averaging over them. Second, to average axial and transverse strain values for each subset volume. This can also be done by simply averaging the strain values over the whole volume using the following equation:

$$\nu_{zy}^{average} = -\frac{\bar{\varepsilon}_{yy}}{\bar{\varepsilon}_{zz}} \tag{5.1}$$

where ν_{zy} is the out-of-plane Poisson's ratio and $\bar{\varepsilon}_{yy}$ and $\bar{\varepsilon}_{zz}$ are the average out-of-plane and in-plane strain values, respectively, that are calculated by averaging the

strain values obtained from the DVC analysis over the whole volume. In addition, to be consistent with the rest of this thesis and also to facilitate a comparison between the results of this chapter and the previous chapters, the ratio of strain norms are also used for measurements of out-of-plane Poisson's ratios as follows:

$$\nu_{zy}^{norm} = -\frac{N_{yy}}{N_{zz}} \tag{5.2}$$

where N_{yy} and N_{zz} are the out-of-plane and in-plane norms, respectively. The norms are calculated from Equation 3.1 using the corresponding in-plane and out-of-plane strain values obtained from the DVC analysis that are averaged over the thickness of the samples. Poisson's ratios of paper samples are reported in three ways [43, 47, 147]; First, by performing a linear fit, or second, a second order polynomial fit to the obtained instantaneous Poisson's ratios during the deformation. Third, only by considering the highest values that experimentally are measured during the deformation at the latest state before failure, which is the method used in this thesis to report the Poisson's ratios.

5.1.1 Effect of Refining

Figure 5.1 shows the plot of average out-of-plane strain values against the average in-plane strains of the softwood samples refined at 0, 60, and 100 kWh/t. As evident, an initial decrease in thickness is observed that later on during the deformation changes to rapid increase passing the initial thickness of the sample. The same trend has also been observed by Verma [47] for softwood samples with a grammage of 166 g/m^{-2}, and is believed to be due to fibre segment activation during early states of deformation. As evident, the sample with the lowest refining has the highest values of out-of-plane strain before failure. In contrast, the change in refining energies from 60 to 100kWh/t does not result in a significant change in the average out-of-plane strain values prior to failure. The lowest Poisson's ratios calculated using the average strain values for the samples refined at 0, 60, and 100kWh/t energies are $\nu_{zy}^{average} = -2.9, -1.62$, and -1.51, respectively, that are observed at the last stage of deformation just before failure. It is also evident that the strain to failure increases with increasing refining energy from 0 to 60kWh/t, while further increase of refining energy from 60 to 100kWh/t resulted in a decrease in the failure strain.

Figure 5.2 shows the out-of-plane strain norms, N_{yy}, plotted against in-plane strain norms, N_{zz}, of the softwood samples that were refined at 0, 60, and 100kWh/t. As can be seen, the lines for Poisson's ratios of $\nu_{zy}^{norm} = -0.5$ and $\nu_{zy}^{norm} = -1$ are also plotted. As evident, in contrast to the average strains, when strain norms are considered, all the samples have Poisson's ratios more negative than $\nu_{zy}^{norm} = -0.5$ at all stages of deformation. It is also evident that the absolute value of Poisson's ratio of the samples decreases with increasing amounts of refining which is consistent with the findings of Section 4.1, where samples with more refining was shown to have lesser values of out-of-plane strain norms. As can be seen, all the samples have Poisson's ratios of almost less negative than $\nu_{zy}^{norm} = -1$ in early stages of deformation, while they exhibit more negative values at later stages of deformation resulting in a concave-up shapes for all the samples.The lowest Poisson's ratios observed at the last stage of deformation just before failure of the samples refined at 0, 60, and 100kWh/t energies are $\nu_{zy}^{norm} = -2.9$, -1.77, and -1.56, respectively. These values seem to be very close to the values of Poisson's ratios that were obtained from average strains. This shows that the choice of average or norm does not change the calculated Poisson's ratios at the last stage of failure for refining samples, and only makes a difference for initial states of defamation. However, a comparison between Figures 5.1 and 5.2 makes it clear that this choice can effect the observed general trends. The obtained values for Poisson's ratios are within the range of the values that are reported in the literature [42, 44, 47]. For example, Poisson's ratios of as low as -4 are reported by Verma [142] for some softwood handsheets at initial deformation states. Post et. al. [44] also reported values of between -1.5 and -2.5 for out-of-plane Poisson's ratios of a range of Kraft pulp handsheets that were obtained using optical measurement methods at the last stage of deformation just prior to failure. In general, from the plot of out-of-plane strain norms, Figure 5.2, it is evident that the absolute values of Poisson's ratios decrease with increasing refining. In other words, softwood samples with lower refining have more negative Poisson's ratios. This agrees with the findings in [142] where increasing amounts of refining for softwood samples with a grammage of 60 g/m^{-2} resulted in less negative Poisson's ratios. This decrease in Poisson's ratio was reported to be so large that the handsheets were no longer auxetic which was rationalized with the fact that higher refining had caused some damage to the fibres.

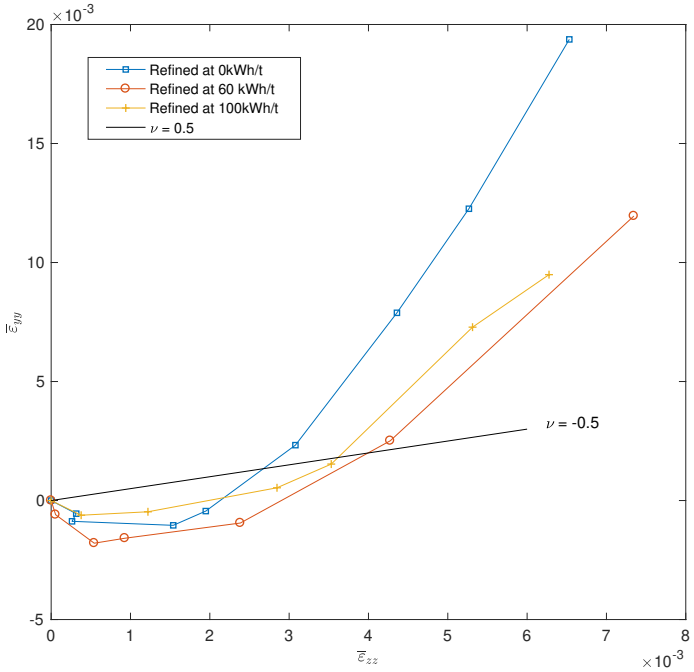

Figure 5.1: Average out-of-plane strain as a function of in-plane strain norms of the 100% NBSK samples refined at 0, 60, and 100kWh/t

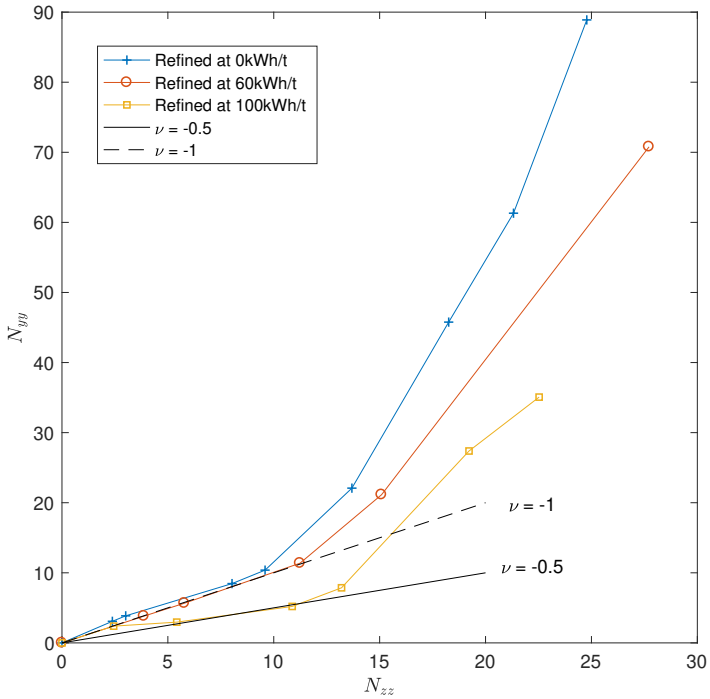

Figure 5.2: Out-of-plane strain norms as a function of in-plane strain norms of the 100% NBSK samples refined at 0, 60, and 100kWh/t

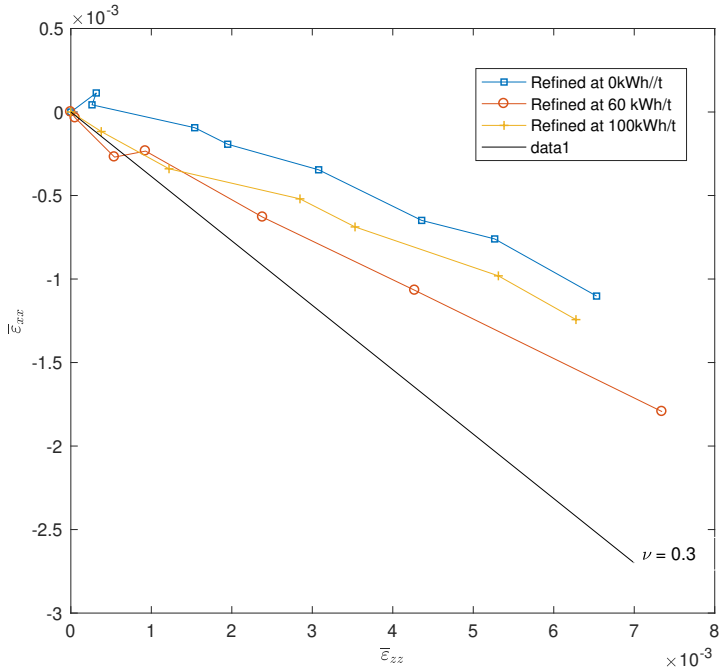

Figure 5.3: Average in-plane strain in transverse direction ($\bar{\varepsilon}_{xx}$) as a function of in-plane strain norms of the 100% NBSK samples refined at 0, 60, and 100kWh/t

Figure 5.3 shows average in-plane strain in transverse direction, $\bar{\varepsilon}_{xx}$, as a function of average axial in-plane strain, $\bar{\varepsilon}_{zz}$, of the softwood samples that were refined at 0, 60, and 100kWh/t. As can be seen, the line for Poisson's ratios of $\nu_{zx}^{average} = 0.3$ is also plotted. In contrast to the average out-of-plane strains where a transition from non-auxetic to auxetic behaviour can be observed, almost all the average in-plane strain values in the transverse direction of the refining samples have negative values resulting in positive Poisson's ratios for all the samples. This shows all the refining samples exhibit non-auxetic behaviour in the transverse in-plane direction. This can be explained by the absence of the layered structure in the transverse direction which exist in the thickness direction due to the way that fibres are laid upon each other during the paper making process. Furthermore, as can be seen, all the samples have Poisson's ratios less than $\nu_{zx}^{average} = 0.3$ for almost all the states of deformation. There is also no apparent correlation between the level of refining and the measured in-plane Poisson's ratios ($\nu_{zx}^{average}$).

5.1.2 Effect of Mixture

Figure 5.4 shows the average out-of-plane strain plotted against average in-plane strain obtained from the DVC analysis for samples with pulp blends of different levels of NBSK and Eucalyptus fibres. As can be seen, a similar trend to that of the refining samples is observable in that the samples' behaviour changes from non-auxetic at initial stages of deformation to auxetic at later stages of tensile deformation. This trend is more distinct for softwood samples than hardwood samples that is explained in [142] to be due to fibre segment activation during early stages of deformation as longer fibres in softwood samples are more likely to have non-activated segments. Figure 5.5 also shows the plot of out-of-plane strain norms versus the in-plane strain norms for the same samples. This transitional behaviour is not observable from the norm plots as the norms are obtained by sum of squares of strain values leading to exclusion of the sign of the values. It is evident from both plots that for the 100% softwood sample, out-of-plane strain values increase more rapidly with increasing in-plane strain when compared to 100% hardwood sample. Although, this does not agree with the findings reported in [142], where all the hardwood samples were reported to have more negative Poisson's ratios than softwood samples, it confirms the existence of strong correlation between paper materials' auxetic behaviour and their processing conditions and pulp mixture. A comparison between Figures 5.4 and 5.5 makes it clear that the use of strain norms or the average values does not change the observed trends. In general, it is evident from both plots that addition of 10 to 20% of NBSK fibres to Eucalyptus fibres results in less negative Poisson's ratio (i.e. less auxetic behaviour), while further increase of NBSK fibres leads to more negative Poisson's ratio when compared to the 100% Eucalyptus sample. Interestingly, a comparison between the Figures 5.5 and 4.9 shows that the 40% NBSK sample is no longer an anomaly in this trend when the out-of-plane norms are plotted against in-plane strain norms. A possible explanation is that by calculation of in-plane strain from DVC analysis possible inconsistencies that might have been introduced by the experimental setup for this sample are excluded. This leads to the conclusion that out-of-plane strain values as a function of in-plane strain values is a better measurement to be used as a criteria for evaluation of network efficiency for the paper samples. Table 5.1

Sample	Refining Energy (kWh/t)	Poisson's Ratio (Strain Norms)	Poisson's Ratio (Average Strain)
Freeze-dried	0	-2.84	-3
100% NBSK	0	-2.97	-2.9
100% NBSK	60	-1.77	-1.62
100% NBSK	100	-1.56	-1.51
100% NBSK-0% Euc.	60	-2.49	-2.35
80% NBSK-20% Euc.	60	-2.23	-2.02
40% NBSK-60% Euc.	60	-1.95	1.94
20% NBSK-80% Euc.	60	-1.33	-1.33
10% NBSK-90% Euc.	60	-1.01	-1.04
0% NBSK-100% Euc.	60	-1.40	-1.28

Table 5.1: Out-of-plane Poisson's ratios (ν_{zy}) of the samples using both strain norms and average strains

summarizes the measured Poisson's ratios for all the samples using both strain norms and average strain values obtained from the DVC analysis. As evident, the choice of strain norms and average values does not lead to a significant difference in the measured Poisson's ratios. This means that for most of the samples there is little to no contraction (i.e. negative deformation) in the thickness and axial directions.

Figure 5.6 shows the out-of-plane strain norms plotted against in-plane strain norms for the mixture samples using the strain fields obtained from the DVC analysis. The only difference between Figures 5.6 and 5.5 is that Figure 5.6 uses the values obtained from the fourth sample of the multi-sample setup except for the 100% Eucalyptus sample where the first sample is used, while Figure 5.5 shows the values obtained from the first sample of the multi-sample test setup except for the 20% and 40% NBSK samples where the same values as for the fourth samples are used due to the limitations in the quality of the obtained data. From a comparison between Figures 5.6 and 5.5, it is clear that while there might be slight changes in the final values of strain norms for different samples inside the multi-sample setup, the general trend does not change. This shows that while some samples inside the multi-sample setup failed at different displacements, the amount of deformation experienced by

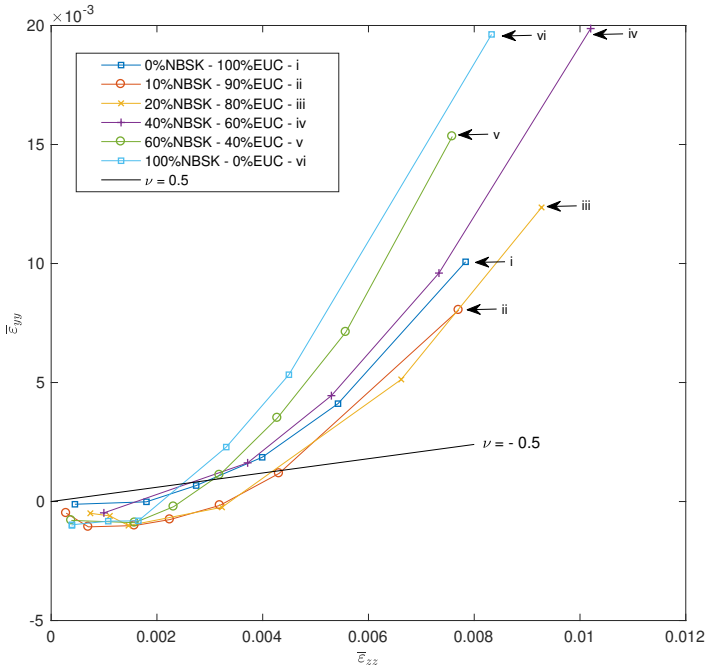

Figure 5.4: Average out-of-plane strain values as a function of average in-plane strain vales of the mixture samples for the first sample of the multi-sample setup

each sample before failure remains almost the same, or in other words, the difference is not significant enough to have an influence on the general trends.

Figure 5.7 shows average transverse in-plane strains, $\bar{\varepsilon}_{xx}$, for the mixture samples as a function of average axial in-plane strains, $\bar{\varepsilon}_{zz}$, along with the line for Poisson's ratios of $\nu_{zx}^{average} = 0.3$. As evident, all the samples exhibit contraction in the transverse in-plane direction, $\bar{\varepsilon}_{xx}$, showing non-auxetic behaviour resulting in positive Poisson's ratios. Furthermore, in contrast to the trends observed for the average out-of-plane strains of the same samples (Figure 5.4), there is no transition from non-auxetic to auxetic behaviour for the transverse in-plane strains. A comparison between the lines for the mixture samples and the line for Poisson's ratios of $\nu_{zx}^{average} = 0.3$, makes it clear that almost all the samples have Poisson's ratios of less than 0.3 except for initial stages of deformation for the 10%NBSK sample. In general, with the exception of 10%NBSK sample that has the largest Poisson's ratios, average in-plane Poisson's ratios seem to decrease with increasing contents of NBSk fibres. This is in contrast to the out-of-plane Poisson's ratios that increased with increasing percentage of NBSK content.

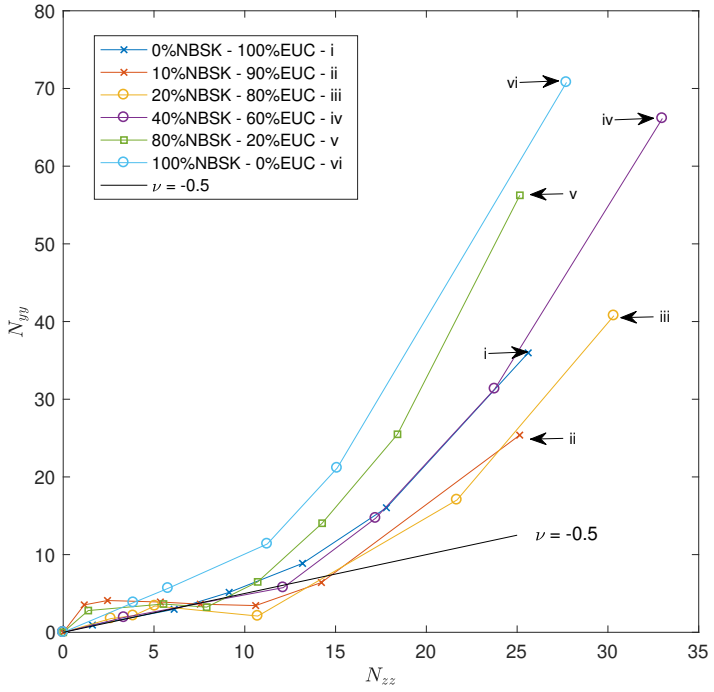

Figure 5.5: Out-of-plane strain norms as a function of in-plane strain norms of the mixture samples for the first sample of the multi-sample setup

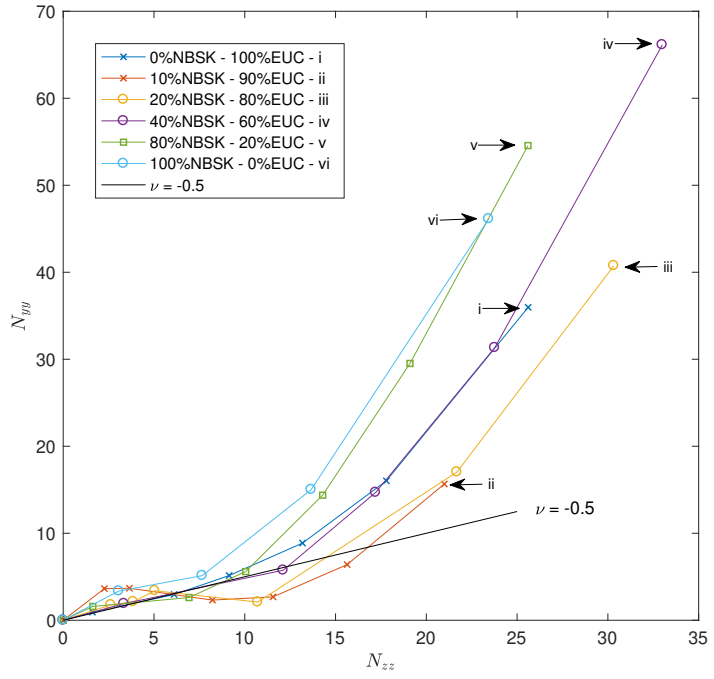

Figure 5.6: Out-of-plane strain norms as a function of in-plane strain norms of the mixture samples for the fourth sample of the multi-sample setup

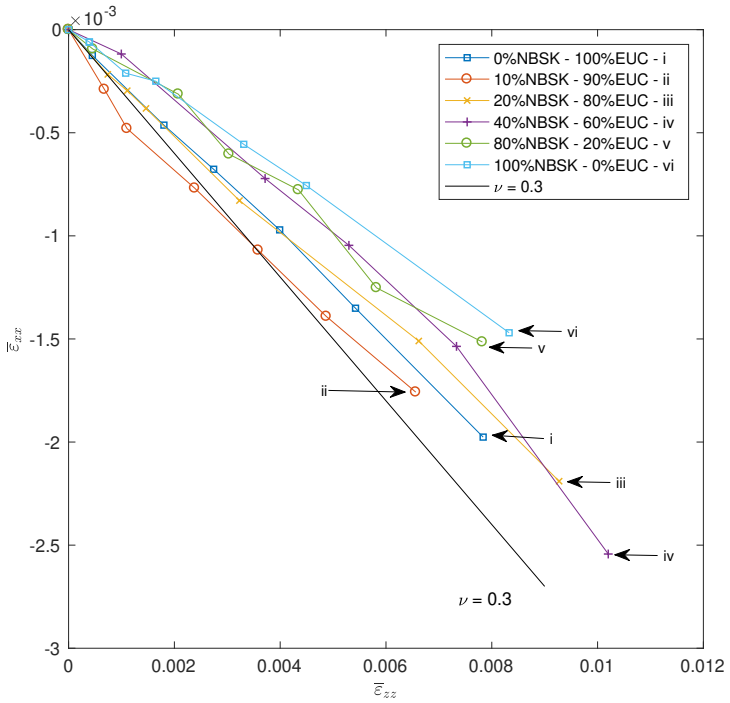

Figure 5.7: Average transverse in-plane strain as a function of average axial in-plane strain of the mixture samples

5.2 Summary

This chapter was intended to show that 4D imaging experiments can also be used for measurements of Poisson's ratios of paper samples. For this purpose the average and norm of the strain fields were used to obtain the plots of out-of-plane versus in-plane strain values. The largest values measured at the last stage of deformation just before failure was reported as the Poisson's ratio of each sample. The obtained values were within the range of the values reported in the literature [142, 44, 42]. It was shown that the choice of average and norm for the strain values result in almost the same Poisson's ratios for the samples. From the plot of strain norms for the refining samples it was found that all the samples initially experienced some thickness reduction that then transitioned to a thickness expansion as the tensile deformation continued leading to an auxetic behaviour for all the samples. This was explained by non-activated fibre segments that become activated during initial states of deformation. In general, it was found that the absolute values of Poisson's ratio decrease with increasing refining energies which is consistent with the findings in the literature [142]. The same trend

of initial thickness reduction followed by thickness expansion was also observed for the mixture samples. In general, the largest Poisson's ratio was measured to be for the 100% NBSK sample being even larger that the 100% Eucalyptus samples. This does not agree with the findings in [142] where the hardwood samples have the largest Poisson's ratios. However, the observed trends in the measured Poisson's ratios agree with the findings of Section 4.2, where small increase in the percentage of softwood samples results in significant reduction in the out-of-plane strain values leading to lower values for Poisson's ratio, and further increase leads to out-of-plane deformation strains larger than that of the 100% Eucalyptus sample. Interestingly, when the out-of-plane strain values are plotted against axial strain values, unlike the plot of strains versus displacements, the 40% NBSK sample is no longer the anomaly in the observed trends. In addition, out-of-plane strain norms obtained from two different samples of the multi-sample geometry were also plotted as a function of in-plane strain norms. These plots showed that while small changes in the norms can be observed for some of the samples, the choice of the sample does not change the general trend observed for the mixture samples.

Chapter 6

Conclusions

Paper despite being ubiquitous has a complex micro-structure that leads to many interesting properties. Although mechanical properties of paper materials have been studied before, the main focus of such studies have been on those that are related to printing. Recent trends in the market has lead the industry to explore new and innovative applications for paper pulp and materials. Therefore, in recent years the mechanical properties of paper have regained interest in the research community in an attempt to further understand the process-structure-property relation of paper materials. This trend has been fuelled by recent advancements in the imaging techniques including x-ray micro-tomography that has facilitated the direct characterization of paper structure. In particular, recent developments in fast synchrotron x-ray micro-tomography has made it possible to acquire 4D (3D+time) data of some physical phenomena in different materials including paper.

6.1 Summary of Findings

The main objective of this thesis has been to obtain 4D image volumes of different paper samples to study the effect of refining and pulp mixture on their deformation and failure. To do so, four different samples were used to study the effect of refining: a freeze-dried sample, and three softwood samples that were refined at 0, 60, 100kWh/t. To study the effect of mixture, six different samples with pulp blends of different levels of NBSK and Eucalyptus fibres were used that were separately refined at 60kWh/t. The samples were cut into a dog-bone shape to ensure that the fracture zones would be

captured inside the field-of-view of the synchrotron tomographic imaging equipment. Four samples from each material were tested concurrently to increase the load to an acceptable level that the tensile tester could capture noise free. For this purpose a multi-sample tensile test holder were designed and 3D printed. Details about the 4D imaging experiments and the samples are provided in Sections 2.1 and 2.2.

6.1.1 Characterization of Deformation Mechanisms

To study the obtained 4D image volumes of the samples two different approaches were taken: fibre-level and network-level analysis. To study the deformation of the samples at the network-level, DVC was applied to the obtained datasets using a commercial software called VicVolume®. Related details can be found in Section 2.4.1. For the fibre-level analysis an improved version of the lumen tracking algorithm were used. The improvements were achieved by adding extra dimensions to the tracking algorithm. Furthermore, two Matlab® functions were developed to calculate the curl index and relative contact areas (RCA) of the segmented fibres that were used to measure the evolution of these micro structural descriptors during deformation. Details of the improved segmentation algorithm and the developed post-processing functions are provided in Sections 2.3.4 and 2.3.5, respectively. Since fibre segmentation algorithm was based on tracking open lumens, only the freeze-dried sample was chosen for this analysis. At the network-level, qualitative observations revealed that the sample exhibits some thickness expansion with increasing deformation which was indicative of auxetic behaviour. This was in contrast to the assumptions made in [47] that the samples with weak hydrogen bonds will not exhibit significant auxetic response. Further, thickness expansions were larger at the bottom of the sample where failure was observed from 3D visualization of the sample confirming similar observations in the literature [44, 135]. In-plane and out-of-plane strain fields were obtained using the DVC analysis. From in-plane strain fields It was found that the strain becomes concentrated in a narrow band at some angle to the applied load at the bottom of the sample corresponding to the region of failure. This confirms the same observations reported in [134, 135, 136]. From the out-of-plane strain fields it was found that the strain becomes concentrated at the bottom of the sample in regions corresponding to in-plane strain concentration confirming qualitative observations. To quantify the

accumulated deformation inside the sample, strain norms were calculated using the obtained strain fields. The trend observed from the plot of out-of-plane strain norm as a function of cross-head displacement had a shape of concave-up that agrees with the expected auxetic behaviour reported in the literature [42, 44, 47]. Detail of the network-level analysis can be found in Section 3.1. At the fibre-level a set of 18 fibres were segmented from the image volumes. Qualitative observations of the segmented fibres revealed some movements for the fibres at the bottom of the sample were failure was qualitatively observed from 3D visualizations of the sample. A closer look at four segmented fibres inside the regions corresponding to large out-of-plane strains also confirmed that the fibres become straightened at earlier states of deformation and experience some inter-fibre bond breakage during later states. Curl index and RCA were also measured for the 18 fibres at two state of deformation using the developed Matlab® codes. From curl index measurements it was found that while most fibres experience straightening, two fibres also become more curly that can be due to fibre buckling under compression. Measurements of RCA also showed that while some fibres loose contact during deformation, some of them can experience an increase in the amount of contact area with other fibres that can be explained by their movements. In general, fibres that were located in the areas that correspond with identified failure regions showed larger values of straightening. In addition, fibres that experience bond breakage were also located inside or near the regions of failure. Details of the fibre-level analysis can be found in Section 3.2.

6.1.2 Industrial Applications

Similar network-level analysis was then used on the obtained image volumes to study the effect of refining on deformation of paper samples, details of which can be found in Section 4.1. Clear fracture zones were captured for the softwood samples refined at 0, 60, and 100kWh/t. From qualitative observations of the number of non-broken fibres dangling inside the fracture zones it was confirmed that the samples with higher refining energies had more efficient networks with less contribution from fibre pull-out to their failure. Furthermore, all the samples showed thickness expansion with increasing deformation that decreased with increasing refining energies. This was explained by the fact that more refined samples had more efficient networks with less free fibre

length, and therefore, less contribution from fibre-straightening and bond breakage to their thickness expansion. In-plane and out-of-plane strain fields were also obtained from the DVC analysis of the samples. In-plane strain fields of the samples refined at 0kWh/t, similar to the freeze-dried sample, showed regions of high strain concentration before failure. Such high strain concentrations were absent inside both the in-plane and out-of-plane strain fields of the samples refined at 60 and 100 kWh/t, which shows that these samples had more uniform stress distribution inside their networks and experienced little to no damage accumulation before failure suggesting more brittle fracture for these samples. This confirmed the findings of Borodulina et.al. [135] that used particle-level simulation to simulate papers with different levels of inter-fibre bonding and reported similar trends for the obtained strain fields. Furthermore, the regions of high out-of-plane strain concentration were concentrated in and around the regions of high in-plane strain for the samples with low network efficiency and not for the samples with high network efficiency. This further confirms the findings in [135] that the regions of high in-plane strain for the highly efficient paper network does not match the regions where inter-fibre bond breakage happens. In other words, the regions of high out-of-plane strains that match the regions corresponding to high in-plane strain are a strong indication of the areas associated with inter-fibre bond failure. Out-of-plane strain norms were also calculated for all the samples to quantify the accumulated deformation inside the samples and were plotted against the cross-head displacements. It was found that the values of out-of-plane strain norms increase with increasing deformation for all the samples which is consistent with the expected auxetic behaviour of paper samples. The values of out-of-plane strain norms were also larger for samples with lower levels of refining. While the difference between the out-of-plane strain norms of the samples were negligible early on during the deformation, it became more significant during later states where inter-fibre bond breakage were more prevalent inside the paper samples with less efficient fibre networks. This further confirmed that out-of-plane strain norms can be used as a criteria to compare the network efficiency (i.e. the extent of inter-fibre bonding) of different paper samples. Overall, it is safe to conclude that out-of-plane strain norms can be used as a criteria to evaluate network efficiency of softwood paper samples.

Considering that the level of inter-fibre bonding becomes an even more important

of a factor in determining the behaviour of paper samples when it comes to papers made from a mixture of two different fibres, the same methods of network analysis were also used on the image volumes obtained for the mixture samples. Qualitative observations of 3D visualizations of the captured fracture zones of the samples showed that the the number of non-broken fibres dangling inside the fracture zones decrease with increasing levels of NBSK fibres that was explained by the fact that the addition of larger fraction of longer NBSK fibres inside the paper network results in more opportunity for inter-fibre bonding and leads to more efficient paper network with less contribution of fibre pull-out to their failure. Strain fields were also obtained for all the mixture samples in both in-plane and out-of-plane directions. It was found that, in general, the magnitude and the extent of strain concentration increases with increasing levels of NBSK fibres. Out-of-plane strain norms were also calculated for all the samples and plotted as a function of cross-head displacement. All the samples showed an increase in the value of the out-of-plane strain norm with increasing deformation revealing auxetic behaviour for all the mixture samples. It was found that addition of 10 to 20 percent of NBSK fibres to Eucalyptus pulp can result in a significant reduction in the out-of-plane strain norms during deformation indicating a significant increase in the network efficiency. Further increase of the fraction of NBSK fibres in the pulp blend resulted in an increase in the measured values of out-of-plane strain norms for the samples which was in contrast to the qualitative observations that showed higher notwork efficiency for the sample with higher levels of NBSK fibres. This is due to the change in the free fibre length of the samples that have more levels of longer NBSK fibres resulting in higher values of thickness expansion as a result of fire straightening and not inter-fibre bond breakage. Therefore, free fibre length measurements need to be considered to remove the extra contribution that the networks with longer free fibre lengths have to their thickness expansion when comparing network efficiency of the mixture samples. Detail of the analysis can be found in Section 4.2. In conclusion, it is not possible to conclude about the network efficiency of the mixture samples of this study by only considering the out-of-plane deformation.

It is also worth noting that although the insights gained from the methods of this study are of possible value to the pulp and paper industry, the cost of 4D imaging

experiments including the equipment and computational costs might make such 4D imaging experiments prohibitive for many. However, recent improvements in lab-based x-ray equipment and related in-situ testing equipment indicate a near future where such 4D experiments will become more accessible.

6.1.3 Mechanistic Insights

In Chapter 5 the results of the 4D imaging experiments were used to find the Poisson's ratios of all the samples. To do so, both the average strain values and the strain norms were used and the largest ratios of out-of-plane versus in-plane strains at the latest state of deformation just before failure were reported as the Poisson's ratio for each sample. The obtained values for all the samples were within the range of values that have been reported for different paper samples in the literature [142, 44, 42]. From the average strain values some thickness reduction during early states of deformation were observable that were consistent with previous observations in the literature [142] where such thickness reductions were explained by activation of non-activated fibre segments that happens early on during deformation. In general, increasing levels of refining energies resulted in samples with less negative Poisson's ratios which is consistent with the findings in [142]. The same trend of initial decrease in sample thickness were also observed for mixture samples that were more significant for the samples with larger fractions of NBSK fibres. This was also observed by Verma [142] and explained by the fact that samples with longer fibres are more likely to have non-activated fibre segments. It was found that the 100% NBSK sample has the larger Poisson's ratio when compared to other samples. This does not agree with the reported values in [142] where 100% hardwood samples have been reported to have the highest Poisson's ratios when compared to 100% softwood samples. Furthermore, the strain values were calculated using two different samples from the multi-sample setup and it was shown that the choice of the sample does not change the general observable trend in the measured strain values of the mixture samples.

6.2 Main Conclusions

The main conclusions of different chapters of this study can be summarized as follows:

- *Characterization of Deformation Mechanisms:*
  - Despite previous reports in the literature, weakly bonded fibre networks (i.e. low efficient paper networks) can also exhibit significant auxetic behaviour.
  - For networks with low efficiency, regions of high in-plane strain concentration correspond to regions of high out-of-plane strain concentration.
  - Fibres inside a paper network become both straightened and buckled during deformation. However, inside and around the failure regions with high concentration of out-of-plane strain, fibre straightening is more prevalent compared to the rest of the network.
  - Inter-fibre bond breakage is also prevalent inside the regions of high out-of-plane strain inside paper networks with low efficiency that, in addition to fibre straightening, is responsible for auxetic behaviour of such papers.
- *Industrial Applications:*
  - There is a strong correlation between the level of refining and the auxetic response of paper networks in that networks with more refining (i.e. more efficient networks) exhibit less auxetic behaviour.
  - Regions of high out-of-plane strain does not correspond to regions of high in-plane strain for paper networks with high efficiency, which confirms the previous findings in the literature.
  - Out-of-plane strain norms can be used as a measure to evaluate network efficiency of paper samples made from the same pulp.
  - There is also a strong correlation between pulp mixture and auxetic response of paper samples in that samples made from pulps with higher levels of softwood fibres exhibit more significant auxetic behaviour.
  - Despite the existence of a strong correlation, out-of-plane strain norms alone cannot be used to evaluate the network efficiency of paper samples made from pulp mixtures containing fibres with different fibre lengths, and the proposed method requires a consideration of free fibre length of the network

- *Mechanistic Insights:*
  - 4D imaging experiments and DVC can be used to measure Poisson's ratios of different paper samples.
  - There is strong correlation between Poisson's ratios of paper samples and their network efficiency and pulp mixture.
  - More refined samples (i.e. more efficient networks) result in less negative Poisson's ratios, and therefore, Poisson's ratio of paper samples can also be used to evaluate their network efficiency .
  - Evaluation of network efficiency of mixture samples using Poisson's ratios also requires consideration of free fibre length of their network.

6.3 Future Work

Considering the shortcomings of the proposed methods to evaluate the level of inter-fibre bonding for mixture samples, it will be interesting to develop a geometrical or mathematical model to calculate the maximum contribution of fibre straightening to the out-of-plane strain values of such papers. In this way the contribution of fibre straightening can be excluded from calculations of the out-of-plane strain norms that will allow for comparison between network efficiency of a wide range of paper samples that are made from pulp mixtures that include fibres with different fibre lengths. This can be achieved by finding the maximum value for free fibre length of the samples which can be calculated by estimating the number of fibre-fibre contact for each fibre using mathematical models for random fibre networks [146]. Since, as explained in Section 1.1.2.2, the level of inter-fibre bonding is suggested to be the deciding factor to evaluate whether a mixture sample will follow the linear mixture rule or not, this can be used to predict the behaviour of different mixture samples. It will also be of interest to develop a network model similar to the one developed by Borodulina et. al. [135] using properties of NBSK and Eucalyptus fibres obtained from the 4D experiments, and compare the strain fields from such models with the strain fields obtained from the DVC analysis to further investigate the findings of this thesis. Finally, it will also be useful to see if there exist a correlation between the RBA values for each sample

and their measured strain norms or Poisson's ratios. This will result in a way to find RBA values from strain norms, or probably to modify the Page's equation to include the Poisson's ratios as a measure of network efficiency instead of RBA measurements.

References

[1] Daniel Tobjörk and Ronald Österbacka. "Paper Electronics". In: *Advanced Materials* 23.17 (May 2011), pp. 1935–1961. ISSN: 1521-4095. DOI: 10.1002/adma.201004692. URL: http:https://doi.org/10.1002/adma.201004692.

[2] Guangyuan Zheng et al. "Nanostructured paper for flexible energy and electronic devices". In: *MRS Bulletin* 38.4 (2013), pp. 320–325. ISSN: 08837694. DOI: 10.1557/mrs.2013.59.

[3] Zhi Li et al. "Melt-and-mold fabrication (MnM-Fab) of reconfigurable low-cost devices for use in resource-limited settings". In: *Talanta* 145.May (2015), pp. 20–28. ISSN: 00399140. DOI: 10.1016/j.talanta.2015.05.002.

[4] R.A. Stratton. "Characterization of Fiber-Fiber Strength from Paper Mechanicl Properties". In: *Proceedings, Tappi 1991 International Paper Physics Conference*. Kona, Hawaii: Tappi Press, 1991, pp. 561–577.

[5] Majid Targhagh. "Simulation of the Mechanical Behaviour of Low Density Paper and an Individual Inter-fibre Bond". Master's Thesis. The University of British Columbia, 2016.

[6] H L Cox. "The elasticity and strength of paper and other fibrous materials". In: *British Journal of Applied Physics* 3.3 (1951), pp. 72–79. DOI: 10.1088/0508-3443/3/3/302.

[7] DH Page. "A theory for tensile strength of paper". In: *Tappi* 52.4 (1969), p. 674.

[8] R S Seth, D H Page, and J Brander. "The Stress Strain Curve of Paper". In: *The Role of Fundamental Research in Paper Making*. Vol. 1. 1981, pp. 421–452.

[9] Elias Retulainen, K Niskanen, and N Nilsen. “Fibers and bonds”. In: *Paper physics* 16 (1998).

[10] Ulrich Hirn and Robert Schennach. “Comprehensive analysis of individual pulp fiber bonds quantifies the mechanisms of fiber bonding in paper”. In: *Scientific Reports* 5.April (2015), p. 10503. ISSN: 2045-2322. DOI: 10.1038/srep10503.

[11] “Bonding between cellulosic fibers in the absence and presence of dry strength agents - A review”. In: *BioResources* 1.2 (2007), pp. 281–318. ISSN: 1930-2126. DOI: 10.15376/biores.1.2.281-318.

[12] Tom Lindström, Lars Wågberg, and Tomas Larsson. “On the nature of joint strength in paper – a review of dry and wet strength resins used in paper manufacturing”. In: *13th Fundamental Research Symposium* 32.May 2005 (2005), pp. 457–562.

[13] William B Campbell. “The mechanism of bonding”. In: *Tappi* 42.12 (1959), pp. 999–1001.

[14] Anna K. Vainio and Hannu Paulapuro. “Interfiber bonding and fiber segment activation in paper”. In: *BioResources* 2.3 (2007), pp. 442–458.

[15] Ahmed Koubaa, Zoltan Koran, and S B T Scott. “Measure of the internal bond strength of paper and board”. In: *2008* 78.3 (20), pp. 103–111.

[16] Warren Batchelor and Jihong He. “A new method for determining the relative bonded area SCATTERING”. In: *TAPPI Journal* 4.6 (2005), pp. 23–28.

[17] WR Haselton. “Gas Adsorption by Wood, Pulp, and Paper. 1. The Low-Temperature Adsorption of Nitrogen, Butane, and Carbon Dioxide by Sprucewood and its Components”. In: *Tappi* 37.9 (1954), pp. 404–412.

[18] William R Haselton. “Gas adsorption by wood, pulp, and paper. II. The application of gas adsorption techniques to the study of the area and structure of pulps and the unbonded and bonded area of paper”. In: *Tappi* 38.12 (1955), pp. 716–723.

[19] Tetsu Uesaka et al. “Determination of fiber-fiber bond properties”. In: *Handbook of Physical and Mechanical Testing of Paper*. 2001.

[20] WL Ingmanson and EF Thode. “Factors contributing to the strength of a sheet of paper. II. Relative bonded area”. In: *Tappi* 42.1 (1959), pp. 83–93.

[21] Warren Batchelor and Jihong He. “A new method for determining the relative bonded area”. In: *TAPPI Journal* 4.6 (2005), pp. 23–28.

[22] F. Malmberg et al. “Measurement of fibrefibre contact in three-dimensional images of fibrous materials obtained from X-ray synchrotron microtomography”. In: *Nuclear Instruments and Methods in Physics Research, Section A: Accelerators, Spectrometers, Detectors and Associated Equipment* 637.1 (2011), pp. 143–148. DOI: 10.1016/j.nima.2011.01.080.

[23] Mattias Aronsson. *On 3D fibre measurements of digitized paper*. 2002. ISBN: 9157663386. URL: http://pub.epsilon.slu.se/273/.

[24] Yash Sharma. “Automated Fibre Segmentation in Micro CT Images of Paper”. Master’s Thesis. The University of British Columbia, 2014. URL: http://hdl.handle.net/2429/50044.

[25] Kari Ebeling. “Distribution of Energy Consumption during Straining of Paper”. PhD Thesis. Lawrence University, Appleton, Wisconsin, 1970, p. 680.

[26] Mikko Alava and Kaarlo Niskanen. “The physics of paper”. In: *Reports on Progress in Physics* 69.3 (2006), pp. 669–723. DOI: 10.1088/0034-4885/69/3/R03.

[27] H. F. Rance. “The formulation of methods and objectives appropriate to the rheological study of paper”. In: *Tappi Journal* 39.2 (1956), pp. 104–115.

[28] Lars Nordman, Pertti Aaltonen, and Tapio Makkonen. “Relationships between mechanical and optical properties of paper affected by web consolidation”. In: *Consolidation of the Paper Web-Transactions of the Symposium held at Cambridge, September 1965*. The British Paper and Board Makers’ Association (Inc.) 1966, pp. 909–927.

[29] DH Page, PA Tydeman, and M Hunt. “Behaviour of fibre-to-fibre bonds in sheets under dynamic conditions”. In: *The formation and structure of paper* 1 (1962), pp. 249–263.

[30] Jerome Phillip Brezinski. “A Study of the Viscoelastic Properties”. PhD Dissertation. Lawrence College, Appleton, Wisconsin, 1955.

[31] J; Kubát. “Rheology of Paper”. In: *Rheology, Volume 5*. Ed. by F. R.; Eirich. New York: Academic Press, 1969. Chap. 10, pp. 547–602.

[32] DH Page, PA Tydeman, and M Hunt. “The formation and structure of paper”. In: *Tech. Sect. Brit. Paper & Board Makers' Assoc., London* (1962), p. 397.

[33] H Kettunen and K Niskanen. “Microscopic damage in paper. Part I: Method of analysis”. In: *Journal of pulp and paper science* 26.1 (2000), pp. 35–40.

[34] GD Zhang et al. “Comparison of the effects of wet straining and refining on the fracture properties of paper”. In: *Nordic Pulp & Paper Research Journal* 17.1 (2002), pp. 45–49.

[35] PA Gradin et al. “Acoustic emission monitoring of light-weight coated paper”. In: *Journal of pulp and paper science* 23.3 (1997), J113–J118.

[36] P. Isaksson, P. A. Gradin, and A. Kulachenko. “The onset and progression of damage in isotropic paper sheets”. In: *International Journal of Solids and Structures* 43.3-4 (2006), pp. 713–726. DOI: 10.1016/j.ijsolstr.2005.04.035.

[37] P. A. Gradin et al. “The use of acoustic emission monitoring to rank paper materials with respect to their fracture toughnes”. In: *Experimental Mechanics* 48.1 (2008), pp. 133–137. DOI: 10.1007/s11340-007-9055-7.

[38] Douglas W Coffin. “A FRACTURE-BASED DESCRIPTION FOR THE DEVELOPMENT OF TENSILE AND TEAR STRENGTH IN PAPER”. In: *J-FOR-JOURNAL OF SCIENCE & TECHNOLOGY FOR FOREST PRODUCTS AND PROCESSES* 6.6 (2018), pp. 29–38.

[39] ANDERSSO. O and Olle Falk. “Spontaneous crack formation in paper”. In: *SVENSK PAPPERSTIDNING-NORDISK CELLULOSA* 69.4 (1966), p. 91.

[40] BC Donner. “An heuristic model of paper rupture”. In: *Proceedings of fundamentals of papermaking materials-11th fundamental research symposium*. 1997, pp. 1215–1247.

[41] Douglas W Coffin, Kun Li, and Ji Li. “Utilization of Modified Linear Elastic Fracture Mechanics to Characterize The Fracture Resistance of Paper”. In: *15th Fundamental Resaerch Symposium*. Cambridge, 2013.

[42] OE Öhrn. “Thickness variations of paper on stretching”. In: *Svensk Papperstidning* 68.5 (1965), pp. 141–149.

[43] Niclas Stenberg and Christer Fellers. “Out-of-plane Poisson’s ratios of paper and paperboard”. In: *Nordic pulp & paper research journal* 17.4 (2002), pp. 387–394.

[44] Paul-Philipp Post et al. “Optical measurement of deformation of paper under tensile load”. In: *Nordic Pulp and Paper Research Journal* 27.2 (2012), pp. 313–317.

[45] N Bekkedahl. “Volume dilatometry”. In: *Journal of research of the National Bureau of Standards* 43.2 (1949), pp. 145–156. ISSN: 0091-0635. DOI: 10.6028/jres.043.017.

[46] Alderson A Evans Kenneth E. “Auxetic Materials, Function Materials and Structure From Lateral Thinking”. In: *Advanced Materials* 12.9 (2000), pp. 617–628.

[47] Prateek Verma, Meisha L. Shofner, and Anselm C. Griffin. “Deconstructing the auxetic behavior of paper”. In: *Physica Status Solidi (B) Basic Research* 251.2 (2014), pp. 289–296. ISSN: 03701972. DOI: 10.1002/pssb.201384243.

[48] Herbert Holik, ed. *Handbook of Paper and Board*. John Wiley & Sons, 2006. ISBN: 9783527309979. DOI: 10.1002/3527608257.

[49] J Lumiainen. “Refining of Chemical Pulp”. In: *Papermaking Part 1: Stock Preparation and Wet End*. Helsinki, 2000, pp. 86–122. ISBN: 978-952-5216-25-7.

[50] Christopher J. Biermann. *Refining and pulp characterization*. 2nd. Academic Press, 1996.

[51] H. Meier. “Chemical and morphological aspects of the fine structure of wood”. In: *Pure and Applied Chemistry* 5.1-2 (1962), pp. 37–52. ISSN: 1365-3075. DOI: 10.1351/pac196205010037. URL: http://pac.iupac.org/publications/pac/5/1/0037/.

[52] J R Barnett and Victoria a Bonham. “Cellulose microfibril angle in the cell wall of wood fibres”. In: *Biological reviews of the Cambridge Philosophical Society* 79.2 (2004), pp. 461–472. DOI: Doi10.1017/S1464793103006377.

[53] B Butterfield. *Three-dimensional structure of wood: an ultrastructural approach*. Springer Science & Business Media, 2012.

[54] T C Maloney and H Paulapuro. “The formation of pores in the cell wall”. In: *Journal of Pulp and Paper Science* 25.12 (1999), pp. 430–436. URL: http://www.scopus.com/scopus/inward/record.url?eid=2-s2.0-0033356908{\&}partnerID=40{\&}rel=R7.0.0.

[55] JM Genco. “Fundamental processes in stock preparation and refining”. In: *Tappi Pulping Conference*. 1. 1999, pp. 57–96.

[56] M Rusu et al. “Relation Between Fibre Flexibility and Cross Sectional Properties”. In: *BioResources* 6.1 (2011), pp. 641–655.

[57] Forsstrom. “Influence of pore structure and water retaining ability of fibres on the strength of papers from unbleached kraft fibres”. In: *Nordic Pulp and Paper Research Journal* 20.02 (2005), pp. 176–185. DOI: 10.3183/NPPRJ-2005-20-02-p176-185.

[58] D. H.; Page. “The beating of chemical pulps–the action and the effects”. In: *Fundamental s of Papermaking 1*. 1989, pp. 1–38.

[59] JD Clark. “Fibrillation, Free Water, and Fiber Bonding”. In: *Tappi* 52.2 (1969), p. 335.

[60] Hong yan Mou et al. “Low consistency refining of eucalyptus pulp: Effects on surface chemistry and interaction with FWAs”. In: *BioResources* 8.4 (2013), pp. 5995–6013. ISSN: 19302126.

[61] T; Kang, H Paulapuro, and ; “Effect of External Fibrillation”. In: *Pulp and Paper Canada* 107 (2006), pp. 51–54.

[62] Paulo J. Ferreira, Sandra Matos, and Margarida M. Figueiredo. "Size characterization of fibres and fines in hardwood kraft pulps". In: *Particle and Particle Systems Characterization* 16.1 (1999), pp. 20–24. ISSN: 09340866. DOI: 10.1002/(SICI)1521-4117(199905)16:1<20::AID-PPSC20>3.0.CO;2-M.

[63] Richard R.; Hartman. "Mechanical Treatment of Pulp Fibers for Property Development". PhD Dissertation. Lawrence University, 1989, pp. 1–162.

[64] Richard J; Kerekes and James A. Olson. "Perspectives on fiber length reduction in refining". In: *Proceedings of 7th PIRA international refining conference & exhibition*. Stockholm, 2003.

[65] RJ Kerekes. "Characterization of pulp refiners by a C-factor". In: *Nordic Pulp and Paper Research Journal* (1990).

[66] R. S.; Seth and D. H.; Page. "Fiber Properties and Tearing Resistance". In: *Tappi Journal* 71.2 (1988), pp. 103–107.

[67] RJ Kerekes. "Rheology of fibre suspensions in papermaking: An overview of recent research". In: *Nordic Pulp and Paper Research Journal* 21.05 (2006), pp. 598–612. ISSN: 0283-2631. DOI: 10.3183/NPPRJ-2006-21-05-p598-612.

[68] WJ Batchelor, KA Kure, and D Ouellet. "Refining and the development of fibre properties". In: *Nordic pulp & paper research journal* 14.4 (1999), pp. 285–291.

[69] UB Mohlin and C Alfredsson. "Fibre deformation and its implications in pulp characterization". In: *Nordic Pulp and Paper Research Journal (Sweden)* (1990).

[70] D. H.; Page. "The beating of chemical pulps–the action and the effects". In: *Fundamental s of Papermaking 1*. 1989, pp. 1–38.

[71] D. H. Page et al. "Curl, crimps, kinks and microcompressions in pulp fibres: Their origin, measurement and significance". In: *Proceedings 8th Fundamental ...* (1985).

[72] R. S. Seth. "The importance of fibre straightness for pulp strength". In: *Pulp and Paper Canada* 107.1 (2006), pp. 34–42. ISSN: 03164004.

[73] Pin Wen Tsai. "Developing Mixture Rules for Non-conservative Properties for Pulp Suspension". Master's Thesis. The University of British Columbia, 2016.

[74] D Gates and Mark WESTCOTT. “Formulae for the relative bonded area of paper made from blended pulps”. In: (2002).

[75] U Britt Mohlin and K Wennberg. “Some aspects of the interaction between mechanical and chemical pulps”. In: *Tappi journal* 67.1 (1984), pp. 90–93.

[76] E Retulainen. “Strength properties of mechanical and chemical pulp blends”. In: *Paperi ja puu* 74.5 (1992), pp. 419–426.

[77] Gongde Zhang, Jaakko E Laine, and Hannu Paulapuro. “Characteristics of the strength properties of a mixture sheet under wet straining drying”. In: *Paperi ja Puu* 84.3 (2002), pp. 169–173.

[78] A Bovin and A; Teder. “Some aspects on additivity”. In: *EUCEPA International Symposium on Paper Pulp Characterization*. Ronneby, Sweden, 1971.

[79] J. A Clark. *Pulp Technology and Treatment for Paper*. 2nd. San Francisco: Miller Freeman Publications, 1985, p. 878. ISBN: 0879301643.

[80] J; Colley. “Properties of Blends of E. Tetrodonta and P. Radiate Pulps”. In: *Appita* 27.1 (1973), pp. 35–41.

[81] A; Vainio and H. Paulapuro. “INTERFIBER BONDING AND FIBER SEGMENT ACTIVATION IN PAPER”. In: *BioResources* 2.3 (2007), pp. 442–458.

[82] Carl A Jentzen. “The effect of stress applied during drying on some of the properties of individual pulp fibers”. PhD thesis. Georgia Institute of Technology, 1964.

[83] Elias Retulainen. *The role of fibre bonding in paper properties*. Helsinki University of Technology, Department of Forest Products Technology, Laboratory of Paper Technology, 1997.

[84] Robert H. ; Marchessault. “The effect of freeze-drying on the physical properties of cellulose fibres and papers”. PhD Thesis. McGill University, 1954.

[85] JA Van den Akker. “A Note on the Theory of Fiber-Fiber Bonding in Paper, The Influence on Paper Strength of Drying by Sublimation”. In: *Tappi* 35.1 (1952), pp. 12–15.

[86] G Chinga-Carrasco. "Exploring the multi-scale structure of printing paper–a review of modern technology." In: *Journal of microscopy* 234.3 (2009), pp. 211–242. DOI: 10.1111/j.1365-2818.2009.03164.x.

[87] S. Rolland du Roscoat et al. "Estimation of microstructural properties from synchrotron X-ray microtomography and determination of the REV in paper materials". In: *Acta Materialia* (2007). DOI: 10.1016/j.actamat.2006.11.050.

[88] Rodney A Brooks and Giovanni Di Chiro. "Theory of image reconstruction in computed tomography". In: *Radiology* 117.3 (1975), pp. 561–572.

[89] Eric N. Landis and Denis T. Keane. "X-ray microtomography". In: *Materials Characterization* 61.12 (2010), pp. 1305–1316. DOI: 10.1016/j.matchar.2010.09.012.

[90] J. Y. Buffiere et al. "In situ experiments with X ray tomography: An attractive tool for experimental mechanics". In: *Proceedings of the Society for Experimental Mechanics, Inc.* 67 (2010), pp. 289–305. ISSN: 10466789. DOI: 10.1007/s11340-010-9333-7.

[91] E. Maire and P. J. Withers. "Quantitative X-ray tomography". In: *International Materials Reviews* 59.1 (2014), pp. 1–43. ISSN: 0950-6608. DOI: 10.1179/1743280413Y.0000000023.

[92] S.R. Stock. "X-ray microtomography of materials". In: *International Materials Reviews* 44.4 (1999), pp. 141–164. DOI: 10.1179/095066099101528261.

[93] Jean Francis; Bloch and Sabine Rolland; Roscoat. "Three-Dimensional Structural Analysis". In: *14th Fundamental Research Symposium*. Oxford, 2009, pp. 599–644.

[94] S Rolland du Roscoat, J-F Bloch, and X Thibault. *Synchrotron radiation microtomography applied to investigation of paper*. 2005. DOI: 10.1088/0022-3727/38/10A/015.

[95] S. Rolland Du Roscoat, J. F. Bloch, and P. Caulet. "A method to quantify the 3D microstructure of fibrous materials containing mineral fillers using X-ray microtomography: Application to paper materials". In: *Journal of Materials Science* (2012). ISSN: 00222461. DOI: 10.1007/s10853-012-6575-z.

[96] Emil J Samuelsen et al. “Three-dimensional imaging of paper by use of synchrotron x-ray microtomography”. In: *Journal of Pulp and Paper Science* 27.March 2016 (2001), pp. 50–53.

[97] Christine Antoine et al. “3D images of paper obtained by phase-contrast X-ray microtomography: Image quality and binarisation”. In: *Nuclear Instruments and Methods in Physics Research, Section A: Accelerators, Spectrometers, Detectors and Associated Equipment* 490 (2002), pp. 392–402. DOI: 10.1016/S0168-9002(02)01003-3.

[98] C Marulier et al. “Towards 3D analysis of pulp fibre networks at the fibre and bond levels”. In: *Nordic Pulp and Paper Research Journal* 27.2 (2012), p. 245.

[99] E. L. G. Wernersson et al. “Characterisations of fibre networks in paper using micro computed tomography images”. In: *Nordic Pulp and Paper Research Journal* 29.03 (2014), pp. 468–475. ISSN: 0283-2631. DOI: 10.3183/NPPRJ-2014-29-03-p468-475. URL: http://www.npprj.se/html/xml/toc8952.html.

[100] Y. Sharma, Andre B. Phillion, and D. M. Martinez. “Automated segmentation of wood fibres in micro-CT images of paper”. In: *Journal of Microscopy* 260.3 (2015), pp. 400–410. ISSN: 13652818. DOI: 10.1111/jmi.12308.

[101] William K. Pratt. “Image Segmentation”. In: *Digital Image Processing*. John Wiley & Sons, Inc., 2002, pp. 551–587. ISBN: 9780471221326. DOI: 10.1002/0471221325.ch17. URL: http://dx.doi.org/10.1002/0471221325.ch17.

[102] P Perona and J Malik. “Scale-space and edge detection using anisotropic diffusion”. In: *IEEE Transactions on Pattern Analysis and Machine Intelligence* 12.7 (1990), pp. 629–639. DOI: 10.1109/34.56205. arXiv: 1102.0183. URL: http://ieeexplore.ieee.org/lpdocs/epic03/wrapper.htm?arnumber=56205.

[103] Joachim Weickert, Bart M. Ter Haar Romeny, and Max A. Viergever. “Efficient and reliable schemes for nonlinear diffusion filtering”. In: *IEEE Transactions on Image Processing* 7.3 (1998), pp. 398–410. DOI: 10.1109/83.661190.

[104] Rolf Adams and Leanne Bischof. “Seeded Region Growing”. In: *IEEE Transactions on Pattern Analysis and Machine Intelligence* 16.6 (1994), pp. 641–647. DOI: 10.1109/34.295913.

[105] C.R. Maurer and V. Raghavan. “A linear time algorithm for computing exact Euclidean distance transforms of binary images in arbitrary dimensions”. In: *IEEE Transactions on Pattern Analysis and Machine Intelligence* 25.2 (2003), pp. 265–270. DOI: 10.1109/TPAMI.2003.1177156. URL: http://ieeexplore.ieee.org/lpdocs/epic03/wrapper.htm?arnumber=1177156.

[106] Xavier Tizon and Örjan Smedby. “Segmentation with gray-scale connectedness can separate arteries and veins in MRA”. In: *Journal of Magnetic Resonance Imaging* 15.4 (2002), pp. 438–445. DOI: 10.1002/jmri.10047.

[107] Johanna Lundén. “Image Analysis Methods for Evaluation of Fibre Dimensions in Paper Cross-Sections”. Master’s Thesis. The Swedish Royal Institute of Technology, 2002.

[108] Rafael. C. González, Richard E Woods, and Stevenn L Eddins. *Digital Image Processing Using MATLAB*. Pearson, 2004.

[109] J Matas et al. “Robust Wide Baseline Stereo from Maximally Stable Extremal Regions”. In: *In British Machine Vision Conference*. 2002, pp. 384–393. ISBN: 1-901725-19-7. DOI: 10.5244/C.16.36.

[110] M Donoser M. Wiltsche and W Bauer. “Tracking of Fibers in 3D paper Structures Obtained by an Automated Microtomy Method”. In: *Proc. of Progress in Paper Physics Conf., Tappi Paper Physics Committee, 2006*. February 2014. 2006, pp. 3–6.

[111] Maria Axelsson. “3D tracking of cellulose fibres in volume images”. In: *Image Processing, 2007. ICIP 2007. IEEE International Conference on*. Vol. 4. IEEE. 2007, pp. IV–309.

[112] Peter Toft. “The Radon transform. Theory and implementation”. In: (1996).

[113] Peter Kontschieder et al. “Detecting paper fibre cross sections in microtomy images”. In: *Proceedings - International Conference on Pattern Recognition* August 2017 (2010), pp. 316–319. ISSN: 10514651. DOI: 10.1109/ICPR.2010.86.

[114] Jens Bache-wiig and Per Christian Henden. "Individual fiber segmentation of three-dimensional microtomograms of paper and fiber-reinforced composite materials". Master's Thesis. Institutt for datateknikk og informasjonsvitenskap, 2005.

[115] Felix Beckmann et al. "In-situ synchrotron X-ray microtomography studies of microstructure and damage evolution in engineering materials". In: *Advanced Engineering Materials* 9.11 (2007), pp. 939–950. ISSN: 14381656. DOI: 10.1002/adem.200700254.

[116] C. Puncreobutr et al. "Quantitative 3D characterization of solidification structure and defect evolution in Al alloys". In: *Jom* 64.1 (2012), pp. 89–95. ISSN: 10474838. DOI: 10.1007/s11837-011-0217-9.

[117] P Latil and C Geindreau. "Fast X-Ray Microtomography for the in Situ Analysis of the Compression of a Saturated Fibre Bundle". In: (2010).

[118] Jérémie Viguié et al. "Analysis of the hygroexpansion of a lignocellulosic fibrous material by digital correlation of images obtained by X-ray synchrotron microtomography: Application to a folding box board". In: *Journal of Materials Science* 46.14 (2011), pp. 4756–4769. ISSN: 00222461. DOI: 10.1007/s10853-011-5386-y.

[119] E. Bar-Kochba et al. "A Fast Iterative Digital Volume Correlation Algorithm for Large Deformations". In: *Experimental Mechanics* C (2014), pp. 261–274. ISSN: 00144851. DOI: 10.1007/s11340-014-9874-2.

[120] Bing Pan et al. "Two-dimensional digital image correlation for in-plane displacement and strain measurement: a review". In: *Measurement science and technology* 20.6 (2009), p. 062001.

[121] B K Bay. *Methods and applications of digital volume correlation*. 2008. DOI: 10.1243/03093247JSA436.

[122] F. Gillard et al. "The application of digital volume correlation (DVC) to study the microstructural behaviour of trabecular bone during compression". In: *Journal of the Mechanical Behavior of Biomedical Materials* (2014). ISSN: 17516161. DOI: 10.1016/j.jmbbm.2013.09.014.

[123] Mark Rivers. "Synchrotron 'pink beam' tomography for the study of dynamic processes". In: *SPIE Newsroom* (Aug. 2016), pp. 10–12. ISSN: 18182259. DOI: 10.1117/2.1201608.006674. URL: http://www.spie.org/x120329.xml.

[124] C Puncreobutr et al. "Quantitative 3D characterization of solidification structure and defect evolution in Al alloys". In: *Jom* 64.1 (2012), pp. 89–95.

[125] P. Thévenaz, D. Sage, and M. Unser. "Bi-Exponential Edge-Preserving Smoother". In: *IEEE Transactions on Image Processing* 21.9 (Sept. 2012), pp. 3924–3936.

[126] Johannes Schindelin et al. "Fiji: an open-source platform for biological-image analysis". In: *Nature methods* 9.7 (2012), pp. 676–682.

[127] S Nixon Von Mark and Alberto S Aguado. *Feature Extraction and Image Processing, pp, 164-168*. 2002.

[128] Robert M Haralock and Linda G Shapiro. *Computer and robot vision*. Addison-Wesley Longman Publishing Co., Inc., 1991.

[129] Aristidis Likas, Nikos Vlassis, and Jakob J Verbeek. "The global k-means clustering algorithm". In: *Pattern recognition* 36.2 (2003), pp. 451–461.

[130] B. K. Bay et al. "Digital volume correlation: Three-dimensional strain mapping using X-ray tomography". In: *Experimental Mechanics* 39.3 (1999), pp. 217–226. ISSN: 0014-4851. DOI: 10.1007/BF02323555.

[131] Bing Pan, Dafang Wu, and Zhaoyang Wang. "Internal displacement and strain measurement using digital volume correlation: a least-squares framework". In: *Measurement Science and Technology* 23.4 (2012), p. 045002. ISSN: 0957-0233. DOI: 10.1088/0957-0233/23/4/045002.

[132] Philip Schneider and David H Eberly. *Geometric tools for computer graphics*. Elsevier, 2002.

[133] M. G.D. Geers, R. De Borst, and W. A.M. Brekelmans. "Computing strain fields from discrete displacement fields in 2d-solids". In: *International Journal of Solids and Structures* 33.29 (1996), pp. 4293–4307. ISSN: 00207683. DOI: 10.1016/0020-7683(95)00240-5. URL: http://dx.doi.org/10.1016/0020-7683(95)00240-5.

[134] AE Ranger and LF Hopkins. “The Formation and Structure of Paper? ed. by Bolam, F”. In: *Tech. Sect. Brit. Paper and Board Makers' Assoc., London England* (1962), p. 277.

[135] Svetlana; Borodulina et al. “Stress-strain curve of paper revisited”. In: *Nordic Pulp and Paper Research Journal* 27.02 (2012), pp. 318–328. ISSN: 0283-2631. DOI: 10.3183/NPPRJ-2012-27-02-p318-328.

[136] M J Korteoja et al. “Local strain fields in paper”. In: *Tappi Journal* 79.4 (1996), pp. 217–223. ISSN: 07341415.

[137] Carl D; Meyer. *Matrix Analysis and Applied Linear Algebra*. 2nd ed. 2000, p. 281.

[138] Anton Hagman and Mikael Nygårds. “Investigation of sample-size effects on in-plane tensile testing of paperboard”. In: *Nordic Pulp and Paper Research Journal* 27.02 (2012), pp. 295–304. ISSN: 0283-2631. DOI: 10.3183/NPPRJ-2012-27-02-p295-304. URL: http://www.npprj.se/html/xml/toc8686.html.

[139] Stefan Andersson. “Low Consistency Refining of Mechanical Pulp ? Process Conditions and Energy Efficiency”. PhD thesis. Mid Sweden University, 2011, p. 53. ISBN: 9789186694609.

[140] D.D.P. Nugroho. “Low Consistency Refining of Mixtures of Softwood & Hardwood Bleached Kraft Pulp : Effects of Refining Power”. Master's Thesis. Asian Institute of Technologye, 2012.

[141] R. Paul Kibblewhite. “Effects of refined softwood/eucalypt pulp mixtures on paper Properties”. In: *Trans. 10th Fundamental Research Symposium* (1993), pp. 127–155.

[142] Prateek Verma. “Auxetic Behavior in Some Fiber Network Structures”. PhD Dissertation. Georgia Institute of Technology, 2015.

[143] Jihong He, Warren J Batchelor, and R.E. Johnston. “A microscopic study of fibre-fibre contacts in paper”. In: *Appita Journal* 57.4 (2004), pp. 292–298. ISSN: 10386807.

[144] DH Page, PA Tydeman, and M Hunt. “A study of fibre-to-fibre bonding by direct observation”. In: *The Formation and Structure of Paper?Trans. Oxford Symp.* Vol. 1. 1961, pp. 171–193.

[145] Steven Le Corre et al. “Rheology of highly concentrated planar fiber suspensions”. In: *Journal of Rheology* 49.5 (2005), pp. 1029–1058. ISSN: 0148-6055. DOI: 10.1122/1.1993594. URL: http://sor.scitation.org/doi/10.1122/1.1993594.

[146] W. J. Batchelor, J. He, and W. W. Sampson. “Inter-fibre contacts in random fibrous materials: Experimental verification of theoretical dependence on porosity and fibre width”. In: *Journal of Materials Science* 41.24 (2006), pp. 8377–8381. ISSN: 00222461. DOI: 10.1007/s10853-006-0889-7.

[147] F. Pierron et al. “Comparison of the mechanical behaviour of standard and auxetic foams by x-ray computed tomography and digital volume correlation”. In: *Strain* 49.6 (2013), pp. 467–482. ISSN: 00392103. DOI: 10.1111/str.12053.